学位論文

Spectroscopic Studies of Metal Oxides with Competing Electron-Electron and Electron-Lattice Interactions

電子間相互作用と電子格子相互作用の競合する
金属酸化物の分光学的研究

小林 研介

学位論文

Spectroscopic Studies of Metal Oxides with Competing Electron-Electron and Electron-Lattice Interactions

電子間相互作用と電子格子相互作用の競合する
金属酸化物の分光学的研究

小林研介

論文の内容の要旨

論文題目　Spectroscopic Studies of Metal Oxides with Competing Electron-Electron and Electron-Lattice Interactions

電子間相互作用と電子格子相互作用の
競合する金属酸化物の分光学的研究

氏名　　小林　研介

物質の多様性を生み出している二大要因として、電子間相互作用と電子格子相互作用が挙げられる。例えば、電子間相互作用は磁性を生み出す主要因であり、一方、電子格子相互作用は電荷密度波（CDW）やポーラロンの形成を引き起こす。この二つの相互作用は、理論的取扱いを容易にするためにも個別に取り扱われることが多いが、実際には多くの系で二つの相互作用は競合している。例えば古くから知られている magnetite における Verwey 転移や、近年非常に注目を集めている遷移金属酸化物における stripe order などの現象を理解するには、二つの相互作用を同時に扱う必要があると考えられている。このように両者の競合は、現代の固体物理の中でも未解決の点が多く、今後の研究が期待されている。その中でも、電子同士が電子格子相互作用による実効的な引力を通じて、お互いのクーロン反発力に打ち勝って対を作る、というスピン一重項電子対の形成は、二つの相互作用の競合が表れている典型的な現象であり、 spin-Peierls 転移、 bipolaron の形成、超伝導など、様々な興味深い現象を引き起こす原因となっている。したがって、この現象は、電子間相互作用と電子格子相互作用、そして両者の競合が物性に与える影響を理解するうえで、最適な研究対象である。我々は、NaV_2O_5、

Ti_4O_7、$Ba_{1-x}K_xBiO_3$ (BKBO) という 3 種類の金属酸化物に対して光電子分光法による研究を行った。この 3 種類は、それぞれスピン一重項電子対に関係のある特徴的な相転移を示すことで知られている。以下にそれぞれの物質系に対する研究結果の概要を紹介する。

NaV_2O_5 は、第二の無機 spin-Peierls 物質として、近年盛んに研究されている。最近では、この系は単純な spin-Peierls 物質ではなく、電荷整列を伴った一重項を形成することが分かってきたが、その特徴ある物性はなお多くの研究者の関心を集めている。結晶構造は、ピラミッド型の VO_5 が稜または角を共有した層状構造を形成した間隙に、Na イオンが挿入されたものであり、b-軸方向に一次元系を形成している。帯磁率は 34 K（「spin-Peierls」転移温度）で急激な減少を示し、スピン一重項電子対を形成する。それ以上の温度領域では、帯磁率はスピン $S = 1/2$ の一次元反強磁性 Heisenberg モデル（交換相互作用 $J \sim 560$ K）によく従っている。バンド計算によれば本系は金属であるが、局所的なクーロン力を取り入れると、絶縁体であることをうまく説明できる。したがって、この系は典型的な一次元 Mott-Hubbard 絶縁体あるいは一次元反強磁性体とみなすことが出来る。我々は、本系の一次元性に注目し、その一粒子励起スペクトルを角度分解光電子分光法を用いて 120 K ($\sim J/5$) と 300 K ($\sim J/2$) で調べた。ただし、サンプルは、低温での光電子分光測定を可能にするため、伝導度の良い $Na_{0.96}V_2O_5$ を用いた。この Na 欠損系の帯磁率は、転移点以上では無欠損のものと同様である。実験の結果、本系の電子状態が O $2p$ バンドも含めて極めて良い一次元性をもっていることがわかった。また、酸素のバンドが殆ど温度変化をしないのに対し、V $3d$ バンドの角度分解光電子スペクトルは、極めて顕著な温度変化を示すことが分かった。その温度変化の原因を調べるために、実験を、一次元 t-J モデルの有限温度での一粒子励起スペクトルの厳密対角化法による計算結果と比べたが、両者は非常に良い対応を示していることが分かった。すなわち、理論計算で得られる特徴的なスピノンとホロンと呼ばれる分散に対応した構造が実験でも見えており、本系において強相関一次元系に特有な性質である「スピン電荷分離」が起きていることを示唆している。また、実験のスペクトルに見られる有限温度効果についても、スペクトルの形状ばかりではなく、スペクトル強度自体がエネルギー運動量空間内で大きな移動を起こすという点でも、理論は実験をよく再現していることが分かった。以上の結果は、一次元 Mott-Hubbard 絶縁体におけるスピン電荷分離を初めて観測したということに加えて、スピノンバンドに存在する Fermi 面的なエネルギーの cutoff の存在によって、一粒子励起スペクトルに顕著な有限温度効果が起きるという理論的な予測を実験的に初めて検証したという点でも意義深いものである。

Ti_4O_7 は、Magnéli 相と呼ばれる一連の化合物群の一種であり、実空間でのスピン一重項電子対（bipolaron）状態が実現している系として注目を集めてきた。本物質は 154 K 以上では金属的な伝導を示すが、それ以下では bipolaron を作り、半導体的な伝導を示すようになる。この高温絶縁体相は bipolaron が動き回るいわば bipolaron liquid と呼べるような状態になっていると考えられている。さらに 140 K 以下の低温絶縁体相ではその電子対が整列を行う。これは bipolaron の結晶化に対応する秩序無秩序転移であり、magnetite Fe_3O_4 で見られるような Verwey 転移に対応する。我々はこの系について、転移温度付近で高分解能光電子分光測定を行い、3 種類の相それぞれに対して、特徴的な光電子スペクトルを得た。まず、高温金属相でのスペクトルは Fermi edge を持ち、確かに金属であることを示している。ただし、Fermi level 上での強度は小さく擬ギャップ的な振る舞いを見せており、スペクトル強度の多くはより高エネルギー側の incoherent 部分に移っている。また、低温絶縁体相では、電荷秩序形成に伴う明白なギャップが観測された。さらに、高温絶縁体相のスペクトルはちょうど Fermi level 上で強度が 0 になり、gapless になっていることが分かった。この相のスペクトルについて Fermi level 付近での形状を定量的に解析した結果、スペクトル強度は Fermi level から測ったエネルギーの二乗に非常によく比例していることが判明した。これは、高温絶縁体相が bipolaron liquid となっていることを考慮すると、Efros-Shklovskii が理論的に予言した乱れた系における「soft Coulomb gap」が見えている可能性を強く示唆するものである。さらに、Fe_3O_4 の金属相のスペクトルに対しても同様の解析を行い、そのスペクトルが温度に依存する有限の状態密度と soft Coulomb gap の重ね合わせで理解できることを見いだした。このことから、Ti_4O_7 と Fe_3O_4 とは Verwey 転移温度直上で、長距離クーロン力が支配的である一方で、電子格子相互作用とランダムな電荷分布の効果が競合していることが理解された。さらに、Verwey 転移温度よりもずっと高温側では均一な金属相へと移行するが、逆に転移温度より低温側では電荷秩序が形成されるという統一的な物理的描像を両者に対して得ることに成功した。

$Ba_{1-x}K_xBiO_3$ (BKBO) は、三次元 perovskite 構造を持つ。その母体物質 $BaBiO_3$ は、CDW 絶縁体であるが、Ba を K で置換していくことによってホールをドープしていくと、$x = x_c$ (~0.38) 付近で、転移温度約 30 K の超伝導体へと転移する。この転移温度は、非銅系の酸化物超伝導体としては非常に高い温度であり、その超伝導のメカニズムに関心が持たれてきた。我々は、BKBO の単結晶（$x = 0.0 - 0.6$、0.6 以上は固溶限界）を用いて、O $1s$ 吸収端での X 線吸収分光（XAS）及び X 線光電子分光（XPS）を行い、BKBO の電子状態を系統的に調べた。このような系統的な研究は本研究が初めてである。XAS の結果により、BKBO の非占有電子状態は、ホールドープ量 x に依存して系統的に変化することが分かった。また、吸収端近傍の構造について、$x = 0.30$ と 0.40 の間で顕著なスペクトル強度の増大が見られた。これは、$x = x_c$ における金属絶縁体転移に対応する。BKBO に対しては、$Ba_xPb_{1-x}BiO_3$（BPBO）が関連物質として知られているが、両者の XAS のデータを比較することによって、ドーピングに

よって引き起こされる電子構造の変化が定性的に異なっていることを明らかにした。一方、BKBOのXPSの結果からは、ホールドープに伴う化学ポテンシャルのシフトを求めることが出来た。得られたシフトの大きさはバンド計算においてrigid bandモデルを仮定した場合と比べて、半分程度の大きさである。Fermi流体論による解析によれば、この結果はBKBO内での準粒子間の相互作用が極めて弱い斥力かあるいは引力である可能性を意味している。また、この事実は、BKBOの金属側での超伝導や絶縁体側での電荷不均化・CDW相の存在との関連を示唆するものである。

以上の3種類の特徴的な金属酸化物の研究を通して共通に観察されたことは、温度あるいはホールドープ量の変化によって、光電子スペクトルの強度が広いエネルギー範囲にわたって顕著に移動することであった。また、その原因は3種類の物質によって異なる事も明らかになった。すなわち、NaV_2O_5では一次元系特有の強い電子間相互作用、BKBOにおいては構造相転移に伴って変化が表れることから電子格子相互作用が、それぞれ主な要因である。また、Ti_4O_7では、両者の競合によって、特異な電子状態の変化が生み出されていることが明らかになった。物性を支配している低エネルギー励起状態は本質的に多体効果であるため、その研究はまだ緒に就いたばかりであるが、本研究では典型的な3種類の物質について電子間相互作用と電子格子相互作用、および両者の競合がどのように物性に影響を与えているかを実験的に定量的に検証できた。

Spectroscopic Studies of Metal Oxides with Competing Electron-Electron and Electron-Lattice Interactions

Thesis

Kensuke KOBAYASHI

Department of Physics, University of Tokyo

1999

Contents

Chapter 1

Introduction

1.1 Electron-electron and Electron-lattice Interactions

Electron-electron and electron-lattice interactions are two main origins which lead to diverse physical properties of solids. In some cases, it may be enough to take only one of the two into account: Polaron, which greatly affects the thermal and electrical properties of ionic or covalent systems, is one of the most typical and important phenomena caused by the electron-lattice interaction. Electrical conductivity in simple metals is also explained by this interaction. On the other hand, many cases are also known where electron-electron interaction plays a dominant role rather than electron-lattice interaction as we learn in the standard theory of magnetism. Nevertheless, both interactions are actually competing in some cases, yielding complex physical properties of solids. In fact, the competition between the two is observed or is expected to be significant in such systems as those which show a spin-Peierls transition, a Verwey transition, and a charge ordering of stripe form.

Among them, the formation of non-magnetic singlet pairs of electrons is the most illustrative of the competition. When it is formed in the real space, the pair is called "bipolaron". Historically, the concept of bipolaron was firstly proposed by Anderson [1.1]. Let us briefly summarize his idea in order to clarify our standpoint. He started from a simple model expressed as

$$\mathcal{H} = -t\sum_{ij\sigma} c^{\dagger}_{i\sigma}c_{j\sigma} + U\sum_{i} n_{i\sigma}n_{i-\sigma} + \sum_{i}\left(\frac{1}{2}Cx_i^2 - gx_i(n_{i\sigma}+n_{i-\sigma})\right), \quad (1.1)$$

where $c_{i\sigma}$ is the annihilation operator of an electron with spin σ at site i, $n_{i\sigma} = c^{\dagger}_{i\sigma}c_{i\sigma}$, and x_i a lattice deformation. The parameters t, U, C and g are the transfer matrix element between sites, the on-site Coulomb repulsion, the elastic constant and the electron-phonon coupling constant, respectively. By eliminating x_i by minimizing the third term of Eq. (1.1), the following

effective Hamiltonian is obtained:

$$\mathcal{H}_{eff} = -t\sum_{ij\sigma} c^{\dagger}_{i\sigma}c_{j\sigma} + (U - S)\sum_{i} n_{i\sigma}n_{i-\sigma}. \qquad (1.2)$$

where $S = \frac{g^2}{C}$ is the lattice deformation energy, serving as a criterion of the strength of the electron-lattice interaction below. Anderson discussed that bipolarons are formed when $U < S$. Although it may be too simplified, this model gives the best example of the competition between the electron-electron and electron-lattice interactions. The spin-Peierls (SP) transition gives another example of the singlet pair while the SP state is insulating with the pairs ordered, being different from bipolarons.

In this thesis we have studied three different oxides namely, NaV_2O_5, Ti_4O_7, and $Ba_{1-x}K_xBiO_3$ (BKBO), where characteristic phase transitions are observed. While they are all related to a singlet-pair formation in common, the transitions are different in nature from compound to compound. We would like to briefly describe the physical properties of the three systems and the content and scope of our work below.

1.2 NaV_2O_5

NaV_2O_5, which has been known since 1970's [1.2], recently attracted considerable attention as Isobe and Ueda [1.3] pointed out in 1996 that this is the second example of inorganic spin-Peierls (SP) compounds discovered following $CuGeO_3$ [1.4], while organic SP materials have been known since 1975 [1.5]. An indication of the SP transition in NaV_2O_5 appears in the magnetic susceptibility $\chi(T)$ [1.3], which shows a broad maximum around ~ 300 K with a rapid decrease below $T_t = 34$ K, implying the formation of a non-magnetic spin-singlet pair due to the SP transition. Above T_t, $\chi(T)$ is well explained by that of a $S = 1/2$ one-dimensional (1D) antiferromagnetic (AF) Heisenberg chain. While it is doubtful nowadays whether NaV_2O_5 is a true SP compound or not [1.6, 7], its puzzling behavior provides an active field of research for both experimentalists and theorists where the patterns of charge order with the singlet state below T_t is supposed to be dominated mainly by U and S. Various charge ordering patterns are proposed based on Eq. (1.1) for the one-dimensional chain or ladder where $J \sim \frac{4t^2}{U}$ competes with S [1.8]. PES measurements were, however, experimentally difficult to perform in this temperature region as reported in Chapter 3.

In contrast, the behavior as a typical 1D-AF chain, which explains the physical properties of this compound well above T_t, is supposed to be determined mostly by U. It has significant importance to study to what extent U can explain this compound in this temperature range. In addition, how a 1D-AF chain behaves is the most basic but not trivial problem among various quantum-spin systems such as spin-ladder, Haldane, spin-Peierls and

frustrated Heisenberg systems. In Chapter 3, therefore, the study of the single-particle excitation and its finite-temperature effects in NaV_2O_5 has been performed from this view point. Quantitative discussion based on the result of the calculation of the 1D t-J model at finite temperatures will be presented.

1.3 Ti_4O_7

Ti_4O_7 has been known since 1950's as a member of Magnéli phases, which form a homologous series of triclinic compounds of the form T_nO_{2n-1} (T = Ti or V, $4 \leq n \leq 10$) [1.9]. While Magnéli-phase compounds undergo various phase transitions, Ti_4O_7 attracted particular attention in 1970's to early 1980's as a typical system where a singlet pair of two polarons, i. e. bipolaron, is formed in real space [1.10]. Indeed, Chakraverty explained that the intersite bipolaron is realized in this compound by introducing the intersite Coulomb interaction into Eq. (1.1). One of the principal motivations to study Ti_4O_7 at that time was to investigate whether a system composed of real-space singlet pairs shows superconductivity or not. Such a concept of "bipolaron superconductivity" proposed more than twenty years ago [1.11] has attracted many researchers up to now and its realization is still under controversy [1.12, 13]. Although no superconductivity has been observed in Ti_4O_7 and related compounds, two successive phase transitions observed in Ti_4O_7 are interesting themselves and need to be clarified: The one is a metal-to-semiconductor transition at 154 K and the other is a semiconductor-to-semiconductor transition at $\sim$ 140 K which can be viewed as a Verwey transition. The three phases separated by the two transitions have been interpreted as a polaron gas, a bipolaron liquid, and a bipolaron solid, implying competition between the electron-electron and electron-lattice interactions in Ti_4O_7.

Our motivation of Chapter 4 has been to study the electronic structure of Ti_4O_7 as a function of temperature in order to characterize the three phases where significant competition between U and S is expected. Among the three phases, the single-particle excitation in the bipolaron-liquid phase is of particular interest since dynamical disorder is inherent in this phase of Ti_4O_7, which is one of the few systems where the existence of dynamical disorder has been established. We have performed a quantitative comparison of the results of Ti_4O_7 with that of the Verwey compound Fe_3O_4.

1.4 $Ba_{1-x}K_xBiO_3$

BKBO is a remarkable compound in that the discovery of its superconductivity was motivated theoretically by band-structure calculation [1.14] in 1988

just after the discovery of high T_c cuprate superconductors. The parent compound $BaBiO_3$ is a charge-density-wave (CDW) insulator in contrast to the prediction of many band-structure calculations that it is a metal with the half-filled non-degenerate Bi 6*s*-O 2*p* antibonding band crossing the Fermi level. By increasing the K content x from 0 to $x > 0$, i. e., by hole doping into $BaBiO_3$, BKBO undergoes a semiconductor-to-superconductor transition at $x = x_c \sim 0.38$. The transition temperature becomes the highest (~ 30 K) at $x = x_c$ [1.15], which is the highest among the copper-free oxides. While many experimental studies have been performed so far on BKBO including transport, optical and tunneling experiments, the mechanism of its superconductivity has not yet been settled: Although the explanation using the conventional BCS theory has been made [1.16], the possibility of other exotic mechanisms such as bipolaron superconductivity has not been excluded [1.17]. Since $BaBiO_3$ shows a CDW order with the stable Bi^{3+} sites which are doubly occupied by 6*s* electrons, it may be possible to consider that singlet pairs of electrons are formed in real space induced by local CDW fluctuation and lead to the Bose-Einstein condensation of the singlet pairs as was treated using the negative-U Hubbard model [1.18, 19] similar to Eq. (1.2). Hence, investigation into the electronic structure of BKBO will serve the elucidation of the mechanism of its superconductivity.

From this viewpoint, x-ray absorption spectroscopy (XAS) and x-ray photoemission spectroscopy (XPS) studies have been performed on BKBO in a systematic way for the first time. XAS gives us information about the unoccupied electronic states and, therefore, is suitable for studying the effect of hole doping on the electronic structure of such a hole-doped system as BKBO. In addition, comparison with $BaPb_{1-x}Bi_xO_3$, a compound closely related to BKBO, has been performed. The core-level shifts of BKBO observed by XPS will be discussed in terms of the chemical potential shift due to the hole doping. By using the Fermi liquid theory, the strength of U will be discussed.

1.5 Scope of this Thesis

In this thesis, we will study the electronic structure of the three kinds of metal oxides, namely, NaV_2O_5, Ti_4O_7, and BKBO where electron-electron and electron-lattice interactions are thought to play a significant and sometimes competing role. These compounds seem to have their own U and S, possibly characterizing there physical properties. Our scope is to understand the electronic structure underlying the compounds through photoemission spectroscopy (PES) measurements. There are almost no experimental methods to investigate the electron-electron and electron-lattice interactions at the same time. Actually, PES probes photoelectrons from the compounds under study and, therefore, is one of the most powerful methods to investigate the

electronic structure and electron correlation in solids. While the information on the other, that is, the electron-lattice interaction, is obtained indirectly, our interest is to study how the effect of the electron-lattice interaction as well as the electron correlation appears in the electronic structure obtained by PES. We believe that such an approach is necessary to fully understand the physical properties of these characteristic systems.

The present thesis is organized as follows. The principle of PES is described in Chapter 2. We also describe the details of experimental setup with several apparatuses newly designed for the present work. The PES studies of NaV_2O_5, Ti_4O_7, and BKBO are presented in Chapters 3, 4, and 5, respectively. Chapter 6 is devoted to conclusion.

References

[1.1] P. W. Anderson, Phys. Rev. Lett. **34,** 953 (1975).

[1.2] A. Carpy and J. Galy, Acta Cryst. B **31,** 1481 (1975).

[1.3] M. Isobe and Y. Ueda, J. Phys. Soc. Jpn. **65,** 1178 (1996).

[1.4] M. Hase, I. Terasaki and K. Uchinokura, Phys. Rev. Lett. **70,** 3651 (1993).

[1.5] J. J. W. Bray, H. R. Hart Jr., L. V. Interrante, I. S. Jacobs, J. S. Kasper, G. D. Watkins, S. H. Wee, and J. C. Bonner, Phys. Rev. Lett. **35,** 744 (1975).

[1.6] H. Smolinski, C. Gros, W. Weber, U. Peuchert, G. Roth, M. Weiden, and C. Geibel, Phys. Rev. Lett. **80**, 5164 (1998).

[1.7] T. Ohama, H. Yasuoka, M. Isobe, and Y. Ueda, Phys. Rev. B **59**, 3299 (1999)

[1.8] J. Riera and D. Poilblanc, Phys. Rev. B **59**, 2667 (1999).

[1.9] S. Andersson, B. Collen, U. Kuylenstierna, and A. Magnéli, Acta Chem. Scand. **11,** 1641 (1957).

[1.10] C. Schlenker, *Physics of Disordered Materials*, eds. by D. Alder, H. Fritzsche, and S. Ovshinsky (Plenum, New York, 1985) p. 369 and references therein.

[1.11] B. K. Chakraverty, J. Phys. (Paris), Lett. **40,** L-99 (1979).

[1.12] A. S. Alexandrov, V. V. Kabanov, and N. F. Mott, Phys. Rev. Lett. **77,** 4796 (1996).

[1.13] B. K. Chakraverty, J. Ranninger, and D. Feinberg, Phys. Rev. Lett. **81,** 433 (1998).

[1.14] L. F. Mattheiss, E. M. Gyorgy, and D. W. Johnson, Jr., Phys. Rev. B **37,** 3745 (1988).

[1.15] R. J. Cava, B. Batlogg, J. J. Krajewski, R. Farrow, L. W. Rupp, Jr., A. E. White, K. Short, W. F. Peck, and T. Kometani, Nature (London) **332**, 814 (1988).

[1.16] A. I. Liechtenstein, I. I. Mazin, C. O. Rodriguez, O. Jepsen, O. K. Andersen, and M. Methfessel, Phys. Rev. B **44**, 5388 (1991).

[1.17] A. V. Puchkov, T. Timusk, M. A. Karlow, S. L. Cooper, P. D. Han, and D. A. Payne, Phys. Rev. B **52**, 9855 (1995).

[1.18] T. M. Rice and L. Sneddon, Phys. Rev. Lett. **47**, 689 (1981).

[1.19] D. Yoshioka and H. Fukuyama, J. Phys. Soc. Jpn. **54**, 2996 (1985).

Chapter 2

Photoemission Experiment

In this Chapter, we will describe the principle of photoemission spectrosropy and the experimental setup which was used for the present thesis.

2.1 Principles of Photoemission Spectroscopy

The technique of photoemission spectroscopy (PES) has been widely used as one of the most suitable methods to study the electronic structure of solids. In this section, we will summarize the principles of this method [2.1]. Details of the actual experimental setup are reported in the following sections.

An electron which absorbs a photon of energy $h\nu$ can be emitted from the solid as a photoelectron. In this process, the energy conservation rule holds:

$$E_{kin}^{v} = h\nu - \Phi - E_B, \tag{2.1}$$

where E_{kin}^{v} stands for the kinetic energy of the emitted electron measured from the vacuum level (E_{vac}), Φ for the work function of the solid under study, and E_B for the binding energy. A schematic diagram of the photoemission process is shown in Fig. 2.1. In real experiments the kinetic energy (E_{kin}) measured from the Fermi level (E_F) is directly observed rather than E_{kin}^{v}. Then,

$$E_{kin} = h\nu - E_B. \tag{2.2}$$

In the one-electron approximation, Koopmans' theorem [2.2] is assumed to hold in the photoemission process, namely,

$$E_B = -\epsilon_k, \tag{2.3}$$

where ϵ_k is the Hartree-Fock orbital energy of a Bloch electron with momentum k in the initial state measured from the chemical potential (μ). This assumption is valid when the wavefunctions of both the initial and final states

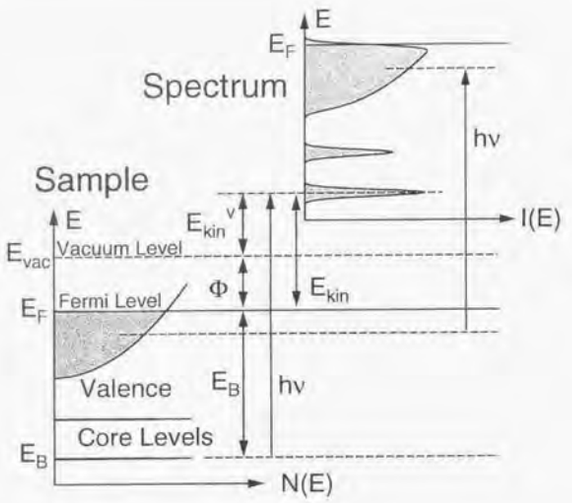

Figure 2.1: Schematic diagram of PES. The density of states $N(E)$ (left panel) can be obtained by measuring the PES spectrum $I(E)$ (right panel). $I(E)$ is broadened due to the instrumental resolution and the photohole lifetime effect.

of the system in the photoemission process are expressed by single Slater determinants of the N- and $(N-1)$-electron systems, respectively. It is also assumed that the removal of an electron from the system does not influence the wavefunctions of the remaining electrons. Furthermore, if the transition matrix element between a Bloch electron in the initial state and a photoelectron in the final state is constant, the photoemission spectrum $I(E_B)$ as a function of E_B can be expressed as:

$$I(E_B) \propto \sum_k \delta(E_B + \epsilon_k) \propto N(-E_B), \tag{2.4}$$

which gives the density of states (N) of Bloch electrons in the solid under study. Since the momentum parallel to the surface of a single crystal sample is conserved through the photoemission process, by measuring emission angles of photoelectrons as well as E_{kin}, the momentum-resolved photoemission spectrum $I(k, E_B)$ can be obtained. This gives the principle of angle-resolved photoemission spectroscopy (ARPES).

Thus, the electronic structure of the occupied states such as the core levels and the valence band can be obtained by measuring the energy spectrum of photoelectron as shown in Fig. 2.1. In the same way, the inverse-photoemission spectroscopy reveals the electronic structure of unoccupied states by injecting electrons of varying energies onto the sample and detecting photons emitted from it.

Next, let us take many-electron effects into account beyond the one-electron approximation. In this more generalized description, photoemission process is regarded as the removal of an electron from the ground state $|\Psi_0^N\rangle$ of the N-electron system with energy E_0^N, leaving the system in an excited state $|\Psi_n^{N-1}\rangle$ of the $(N-1)$-electron system with energy E_n^{N-1}. Then, E_B gives the difference between E_0^N and E_n^{N-1}, namely,

$$E_B = E_n^{N-1} - E_0^N + \mu. \tag{2.5}$$

Using Fermi's golden rule, the photoemission spectrum, which now corresponds to the single-particle excitation spectrum of the system, is expressed as

$$I(\omega) \propto \sum_n |\langle \Psi_n^{N-1} | a_k | \Psi_0^N \rangle|^2 \delta(\omega - (E_0^N - E_n^{N-1} + \mu)), \tag{2.6}$$

where a_k is the annihilation operator of the electron occupying the orbital k. In terms of the Green function formalism, Eq. (2.6) can be rewritten in another expression [2.3]. Let the Green function $G(k,t)$ defined as:

$$G(k,t) \equiv -i\langle \Psi_0^N | T[a_k(t) a_k^\dagger(0)] | \Psi_0^N \rangle, \tag{2.7}$$

where $a_k^\dagger$ is the creation operator of an electron with momentum k and T is Wick's time-ordering operator. By Fourier-transforming Eq. (2.7), the well-known formula called Lehmann representation is derived:

$$G(k,\omega) = \int_\mu^\infty dz \frac{A^e(k,z)}{\omega - z + i\eta} + \int_{-\infty}^\mu dz \frac{A^h(k,z)}{\omega - z - i\eta}, \tag{2.8}$$

where

$$A^e(k,\omega) = \sum_n |\langle \Psi_n^{N+1} | a_k^\dagger | \Psi_0^N \rangle|^2 \delta(\omega - (E_n^{N+1} - E_0^N + \mu)),$$

and

$$A^h(k,\omega) = \sum_n |\langle \Psi_n^{N-1} | a_k | \Psi_0^N \rangle|^2 \delta(\omega - (E_0^N - E_n^{N-1} + \mu)).$$

$A^e(k,\omega)$ and $A^h(k,\omega)$ are called electron and hole spectral functions, respectively. Using the identity

$$\frac{1}{x \pm i\eta} = \mathrm{P}\frac{1}{x} \mp i\pi\delta(x), \tag{2.9}$$

one obtains

$$A^h(k,\omega) = \frac{1}{\pi}\mathrm{Im}\,G(k,\omega) \quad \text{for } \omega \leq \mu \tag{2.10}$$

and

$$A^e(k,\omega) = \frac{1}{\pi}\mathrm{Im}\,G(k,\omega) \quad \text{for } \omega \geq \mu. \tag{2.11}$$

The formula often used in photoemission spectroscopy is finally obtained:

$$I(\omega) \propto \frac{1}{\pi}\sum_k \mathrm{Im}\,G(k,\omega). \tag{2.12}$$

Now it becomes clear that the imaginary part of the Green function can be measured by photoemission spectroscopy. Similarly, the electron spectral function $A_k^e(k,\omega)$ is measured by inverse-photoemission spectroscopy.

Here, let us see some examples of the spectral lineshape based on the above formalism. Using the Dyson equation [2.3],

$$G(k,\omega) = G_0(k,\omega) + \Sigma(k,\omega)G(k,\omega), \tag{2.13}$$

where $G_0(k,\omega)$ and $\Sigma(k,\omega)$ represent the Green function of a non-interacting electron or hole and the self-energy, respectively. Applying $G_0(k,\omega) = (\omega - \epsilon_k)^{-1}$ [2.3],

$$G(k,\omega) = \frac{1}{\omega - \epsilon_k - \Sigma(k,\omega)}. \tag{2.14}$$

First, in the simplest case where the one-electron picture is exactly applicable with $\Sigma(k,\omega) \equiv 0$,

$$I(\omega) \propto \sum_k \delta(\omega - \epsilon_k) \tag{2.15}$$

holds, which is Koopmans' theorem itself. See Fig. 2.2 (a).

As a second example, if $\Sigma(k,\omega)$ is not zero,

$$A^h(k,\omega) = \frac{1}{\pi}\mathrm{Im}\,G(k,\omega) \tag{2.16}$$

$$= \frac{\mathrm{Im}\Sigma(k,\omega)}{\pi\left[(\omega - \epsilon_k - \mathrm{Re}\Sigma(k,\omega))^2 + (\mathrm{Im}\Sigma(k,\omega))^2\right]} \tag{2.17}$$

For simplicity, let us think the Fermi liquid with a local self-energy, where $\Sigma(k,\omega) \equiv \Sigma(\omega)$ holds, which is supposed to be a good approximation when the interaction is of short-range [2.4]. Then,

$$\Sigma(\omega) \simeq -a\omega - ib\omega^2 \quad (a, b > 0) \tag{2.18}$$

holds near the Fermi level ($\omega = 0$), yielding

$$A^h(k,\omega) \propto \frac{b\omega^2}{\pi\left[(\omega - \epsilon_k + a\omega)^2 + b^2\omega^4\right]} \tag{2.19}$$

$$= \frac{z^2 b\omega^2}{\pi\left[(\omega - z\epsilon_k)^2 + z^2 b^2\omega^4\right]}. \tag{2.20}$$

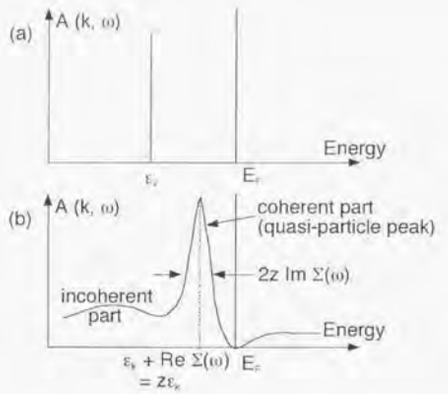

Figure 2.2: Spectral function (a) when the one-electron approximation is exactly applicable and (b) when the electron correlation is considered.

Here, $z \equiv (1+a)^{-1} < 1$. As shown in Fig. 2.2 (b), the peak position of the quasi-particle which is called "coherent part" is located at $\omega = z\epsilon_k$ with the spectral weight z. The remaining spectral weight is transferred to the "incoherent part" away from the Fermi level. These phenomena are due to electron correlation which also affects other physical properties as observed in the enhancement of the coefficient of the electronic specific heat with the factor of $z^{-1} > 1$. Thus, the ratio of the spectral weight between the coherent and incoherent parts reflect the strength of electron correlation as observed in the Ti and V oxides [2.5]. In Chapter 4, we will see that the PES spectra of Ti_4O_7 in the metallic phase has a small coherent part with a large incoherent part, implying the significance of electron correlation in this system.

As may be already clear from the above example, it must be emphasized that the information on the final states which is obtained in the PES measurements does not necessarily reflect the properties of the ground state for strongly correlated systems. Among one of the most extreme examples far from trivial is the one-dimensional correlated system whose excitation spectra are continuum with the characteristic dispersions called "spinon" and "holon". These features can never be obtained in the one-electron approximation. This subject will be discussed in more detail in Chapter 3.

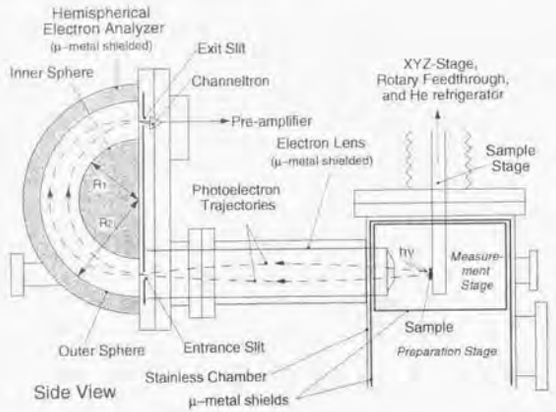

Figure 2.3: Sketch of the VSW system with the VSW hemispherical electron analyzer. The principle of the hemispherical electron analyzer is also shown. Note that actual trajectories of photoelectrons are more complicated due to the electron lens composed of several parts with various parameters. R_1 and R_2 are the radii of the inner and outer hemispheres, respectively.

2.2 Experimental Setup

In this section, we will describe two major photoemission systems which are used for the present thesis. One is an ARPES system which was implemented in the system (the VSW system), which was built seven years ago. Most of the data of NaV_2O_5 presented in Chapter 3 were obtained using this instrument. The other was an ultraviolet photoemission spectroscopy (UPS) system which was newly built mainly by the author with the help of some coworkers for the purpose of obtaining spectra of higher quality. All the spectra of Ti_4O_7 reported in Chapter 4 were obtained on this newly-built UPS spectrometer (the OMICRON system).

2.2.1 ARPES System

The VSW system had a VSW hemispherical electron analyzer installed in the μ-metal-shielded stainless chamber. Figure 2.3 shows the sketch of the system. The specifications of this system are tabulated in Table 2.1 at the end of this section. The light source was a VG discharge lamp. A sample is mounted on a sample stage made of copper which can be cooled by an IWATANI closed-cycle He-refrigerator down to $\sim$ 20 K. The energies of photoelectrons emitted from the sample surface are analyzed by the VSW

hemispherical electron analyzer, whose principle is as follows: The emitted photoelectrons first enter the electron lens, where they are focused by means of electrostatic fields. Then, they go into the analyzer where only photoelectrons with a given energy (pass energy E_P) can pass through the electrostatic field created between the outer and inner spheres. Finally, the number of photoelectrons which reach the channeltron is counted. The resolution of an ideal hemispherical electron analyzer ΔE is expressed in a simplified equation as

$$\Delta E = E_P(\frac{w}{2R_0} + \frac{\alpha^2}{4}), \tag{2.21}$$

where w, R_0, and α are the slit size, the mean radius of the hemispheres, and the acceptance angle at the entrance slit. $R_0 = (R_1 + R_2)/2$, where R_1 and R_2 are the radii of the inner and outer hemispheres. Using the parameter $R_0 = 150$ mm and $\alpha/2 = 4°$ of the VSW analyzer, $\Delta E = 5$ meV is obtained for $E_P = 1$ eV and $w = 1$ mm. Although α is dependent on the retarding voltage ($= E_P - E_{kin} + \phi_A$, where ϕ_A is the workfunction of the analyzer), this value falls in the same order as the actual resolution $\sim$ 18 meV measured at the Fermi edge of gold at 20 K. The deviation between the ideal and actual instrumental resolutions may be due to several reasons: the incomplete focusing of photoelectrons due to inhomogeneity of the electrostatic fields in the spectrometer, the fluctuations of the power supplies and the ground level, residual magnetic field in the spectrometer, external noises, and so on.

The VSW electron analyzer had an acceptance angle of $\pm 4°$ which was too large for the purpose of ARPES measurements. Hence, we had to narrow down the acceptance angle. As shown in Fig. 2.4, this was realized by installing a slit with an aperture at the entrance of the electron lens of the analyzer. The diameter of the aperture was set 2.0 mm, which geometrically yielded the acceptance angle of $\pm 1.0°$. By using a rotary feedthrough, this aperture slit can be both installed and removed quickly from the outside of the spectrometer without breaking the vacuum.

Prior to the measurements of NaV_2O_5, we had tested ARPES measurements on cleaved surfaces of highly orientated pyrolytic graphite (HOPG). ARPES spectra measured using $h\nu = 21.2$ eV at various take-off angles θ's, which are defined as in Fig. 2.4, are shown in Fig. 2.5 (a). After having converted θ's to the momenta in the crystal, the experimental band structure plot was obtained as shown in the density plot of Fig. 2.5 (b)[1]. While HOPG is a good layered compound, it has rotational disorder of in layers, forming a "mosaic" crystal. As a result, it was impossible to distinguish between the Γ-K and Γ-M in the Brillouin zone. Except for this, the obtained result is consistent with the previous reports of ARPES study on single-crystal graphite [2.6–8]. It is instructive to compare the experiment with the result of the band-structure calculation [2.9] shown in Fig. 2.6. Our result agrees

[1] This kind of analysis will be described in detail in Chapter 3.

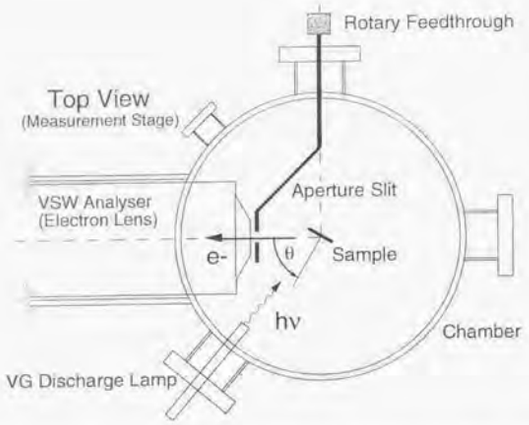

Figure 2.4: AREPS system with an aperture of a diameter of 2.0 mm, which was set at the entrance of the electron lens of the hemispherical electron analyzer. This figure corresponds to the top view of the measurement stage shown in Fig. 2.3. The aperture slit was mounted on the rotary feedthrough which enabled us to install and remove the aperture slit without breaking the vacuum. The definition of the take-off angle θ is also given.

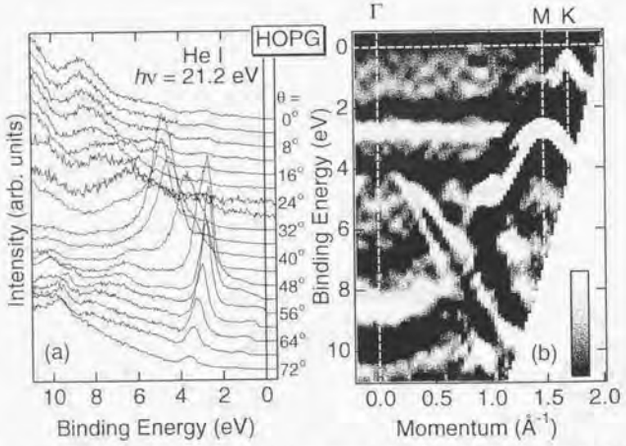

Figure 2.5: (a) ARPES spectra of HOPG measured at various take-off angles θ. (b) The density plot of the second derivative of the spectra.

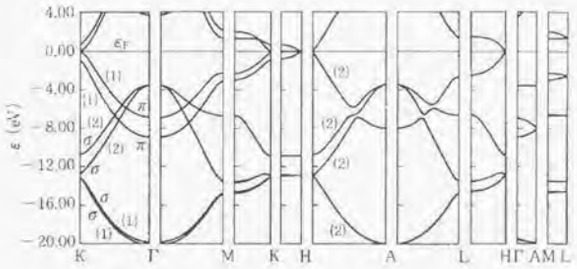

Figure 2.6: Calculated energy band structure of graphite [2.9].

with their result, for example, in that the graphite crosses the Fermi level at the K point. The broad non-dispersive band at $E_B \sim 3$ eV is attributed to a surface state [2.7].

We evaluated the effect of the aperture as follows. In Fig. 2.7 (a), the spectra of HOPG measured with the aperture slit and without it are shown by solid and dashed curves, respectively. The former spectra apparently have sharper peaks than the latter. Especially, in the spectra at $\theta = 37°$, 39°, and 41° taken with the aperture slit, two dispersing features around $E_B \sim 3$–4 eV are observed, which can be hardly seen in the spectra without the aperture slit. By further analyzing these results as shown in Fig. 2.7 (b) and considering that the acceptance angle without the aperture slit is $\pm 4°$, it was plausible that the aperture slit with a diameter of 2.0 mm surely gives the acceptance angle of about $\pm 1°$ as geometrically expected.

Actually, we took Laue photos of samples to fix the crystal orientations before ARPES measurements. We recorded the orientation of the crystal on the sample holder, since the Laue photos were taken outside the spectrometer. A sample holder for recording the Laue results was newly designed for this purpose. After having prepared the ARPES setup as described above, the ARPES measurements of NaV_2O_5 were performed with sufficient reliability and reproducibility.

2.2.2 OMICRON UPS System

The VSW system was built seven years ago, which was a state-of-the-art analyzer at that time with the energy resolution of ≤ 20 meV. However, since the techniques of PES measurements have made a remarkable progress in these few years, energy resolution ≤ 5 meV was achieved nowadays. Hence, a new UPS system was planned three years ago, which aimed at the following points.

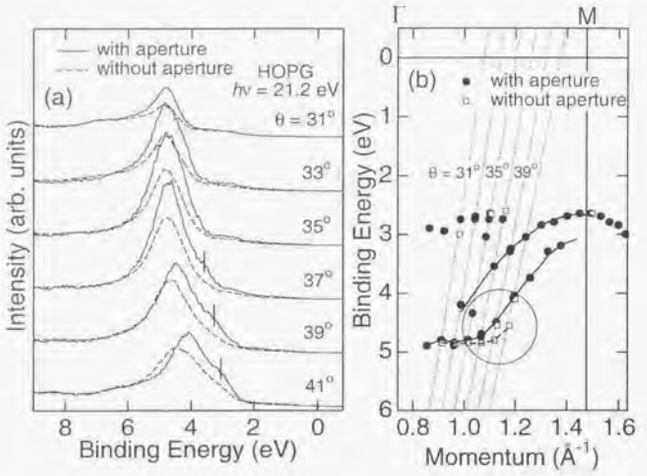

Figure 2.7: (a) Spectra of HOPG measured with the aperture slit and without it are shown by solid and dashed lines, respectively. The features in the spectra with the aperture slit, which are indicated by vertical bars, are hardly observed in the spectra without it. (b) Band dispersions obtained from the spectra with the aperture slit and without it. The result without the aperture slit failed to distinguish the band which disperses rapidly especially for the region indicated by a circle.

- It achieves the energy resolution better than 10 meV.
- In order to shield the terrestrial magnetic field, the vacuum chamber is composed of μ-metal. At the same time, the base pressure in the spectrometer is expected to be improved, because the surface area can be reduced due to disuse of μ-metal shields inside the spectrometer.
- It has enough room to install a LEED system. A LEED system with Auger spectroscopy will be useful in preparing samples *in situ*.
- It has a lower operating pressure when using the He discharge lamp, which is possible by pumping the main chamber with a turbo molecular pump (TMP) and with an ion pump (IP) at the same time.
- It cools samples down to 7 K using a new closed-cycle He refrigerator.

Figure 2.8 shows a sketch of the main part of the OMICRON system. The specifications of the OMICRON system compared with the VSW system are tabulated in Table 2.1. While it has a slightly smaller radius

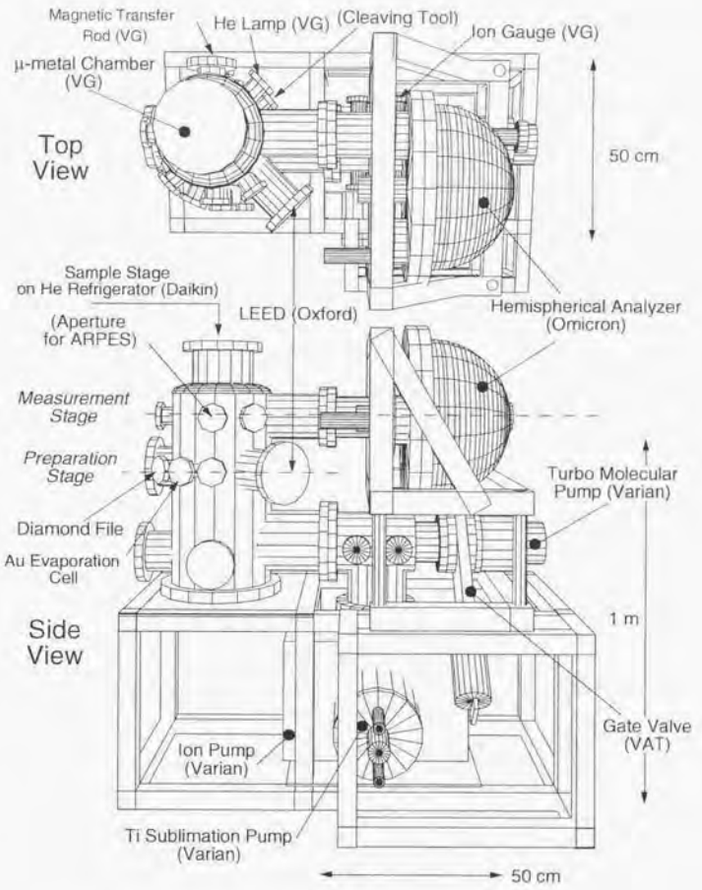

Figure 2.8: Sketch of the main part of the OMICRON UPS system.

	OMICRON System	VSW system
Chamber	μ-metal chamber	stainless chamber with μ-metal shields
Electron Analyzer	OMICRON (EA-125 HR)	VSW (Class-150)
Energy Resolution (at Fermi edge)	14 meV	18 meV
Line Width of Xe $5p_{3/2}$ (gas phase)	7 meV	—
Channeltron Type	Five Channeltrons	Single
Mean Radius (R_0)	125 mm	150 mm
Pass Energy (E_p)	≥ 0.5 eV	≥ 1 eV
Acceptance Angle (α)	$\pm 1°$, $\pm 4°$, and $\pm 8°$	$\pm 4°$ (fixed)
He Discharge Lamp	VG	VG
IP	Varian VacIonPlus300	ULVAC UTM-150
TP	Varian V250	—
Base Pressure	$< 1 \times 10^{-11}$ Torr	5×10^{-11} Torr
Operating Pressure	1×10^{-9} Torr	1×10^{-8} Torr
He Refrigerator	DAIKIN (V204 SCL)	IWATANI (D310)
Lowest Temperature Reached at Sample	7 K	20 K
Temperature Controller	Scientific Instruments (Model 9650)	(homemade system)*
Thermometer	silicon diode	thermocouple
Other Apparatus	Sample Transfer* Oxford LEED ANELVA Ion Gun Annealing Stage*	Sample Transfer* Aperture Slit* Sample Cleaver*

Table 2.1: Comparison between the OMICRON and VSW systems. The asterisks indicate a homemade apparatus.

$R_0 = 125$ mm than the VSW analyzer ($R_0 = 150$ mm), the OMICRON analyzer has a more optimized electron lens system and a multi-channeltron detector, which promise higher energy resolution and more efficient collection of photoelectrons, respectively. The system was almost completed in the spring of 1998, while there were left some more devices such as a cleaving tool and an aperture slit to be installed. The energy resolution estimated from the Fermi edge of gold has not yet reached the expected value < 10 meV, while the line width of Xe $5p_{3/2}$ in the gas phase is 7 meV. The reason for these deviations is now under investigation. The cooling and temperature control system work as we expected, which is significantly important in that, for example, much more compounds are superconducting at 7 K than at 20 K. The base and operating pressures are greatly improved compared to those in the VSW system, enabling us to continue measurements for a much longer time. The measurement of Ti_4O_7 was successfully done in the OMICRON UPS system thanks to the efficient photoelectron acquisition of the OMICRON analyzer and the stable temperature control system.

References

[2.1] S. Hüfner, *Photoelectron Spectroscopy* (Springer-Verlag, Berlin, 1994); G. K. Wertheim and P. H. Citrin, in *Photoemission in Solids*, edited by M. Cardona and L. Ley (Springer-Verlag, Berlin, 1978), Vol. I.

[2.2] P. Fulde, *Electron Correlations in Molecules and Solids* (Springer-Verlag, Berlin, 1991).

[2.3] *e.g.* A. L. Fetter and J. D. Walecka, *Quantum Theory of Many Particle Physics* (McGraw-Hill, New York, 1971).

[2.4] N. Tsuda, K. Nasu, A. Fujimori, and K. Siratori, *Electronic Conduction in Oxides* (Shokabo, Tokyo, 1993).

[2.5] A. Fujimori, I. Hase, H. Namatame, Y. Fujishima, Y. Tokura H. Eisaki, S. Uchida K. Takegahara, and F. M. F. de Groot, Phys. Rev. Lett. **69,** 1796 (1992).

[2.6] A. R. Law, J. J. Barry, and H. P. Hughes, Phys. Rev. B **28,** 5332 (1983).

[2.7] D. Marchand, C. Frétigny, M. Laugës, F. Batallan, Ch. Simon, I. Rosenman, and R. Pinchaux, Phys. Rev. B **30,** 4788 (1984).

[2.8] T. Takahashi, H. Tokailin, and T. Sagawa, Solid State Commun. **52,** 765 (1984).

[2.9] J.-C. Charlier, X. Gonze, and J.-P. Michenaud, Phys. Rev. B **43,** 4579 (1991).

Chapter 3

One-Dimensional Mott-Hubbard Insulator NaV_2O_5

We have made an angle-resolved photoemission (ARPES) study of NaV_2O_5, which undergoes a spin-Peierls-like transition at $T = 34$ K, and analyzed the results in terms of a one-dimensional (1D) Mott-Hubbard (MH) insulator or a 1D antiferromagnetic chain with nearest-neighbor exchange interaction $J \sim 560$ K. The ARPES spectra of the O $2p$ band as well as the V $3d$ band are found to be highly anisotropic, reflecting the one-dimensionality of the electronic structure of NaV_2O_5. The spectra of the V $3d$ band, which corresponds to the lower Hubbard band, are very sensitive to changes in the measurement temperature of the order $\sim J$. We have compared the experimental results with the one-particle spectral function of the one-dimensional t-J model at finite temperatures calculated by exact diagonalization. Good overall agreement is obtained between experiment and theory, which indicates the existence of holon and spinon excitations in this system, reflecting the spin-charge separation due to the reduced dimensionality. Although they are more drastic than the theoretical prediction, the experimental finite temperature effects have been partly explained according to the scenario of spin-charge separation, which may be expressed as the Fermi surface effect of the spinon band.

The content of this chapter was reported in: K. Kobayashi, T. Mizokawa, A. Fujimori, M. Isobe, and Y. Ueda: Single-Particle Excitations in One-Dimensional Mott-Hubbard Insulator NaV_2O_5, Phys. Rev. Lett. **80**, 3121 (1998); K. Kobayashi, T. Mizokawa, A. Fujimori, M. Isobe, and Y. Ueda: Angle Resolved Photoemission Study of the Spin-Peierls System α'-NaV_2O_5, J. Electron Spectrosc. Relat. Phenom., **92**, 87 (1998); K. Kobayashi, T. Mizokawa, A. Fujimori, M. Isobe, Y. Ueda, T. Tohyama, and S. Maekawa: Finite Temperature Effects in One-dimensional Mott-Hubbard Insulator: Angle-Resolved Photoemission Study of $Na_{0.95}V_2O_5$, Phys. Rev. Lett. **82**, 803 (1999).

3.1 Introduction

α'-NaV_2O_5 has attracted considerable attention as the second example of inorganic spin-Peierls (SP) compounds [3.1] discovered following $CuGeO_3$ [3.2]. While NaV_2O_5 [1] itself was known more than twenty years ago [3.3], an indication of the SP transition was recently pointed out by Isobe and Ueda [3.1] through the temperature (T) dependence of magnetic susceptibility $\chi(T)$. As shown in Fig. 3.1, the behavior of $\chi(T)$ is peculiar in that it has a broad maximum around $\sim$ 300 K with a rapid decrease below $T = T_t = 34$ K, implying the formation of a non-magnetic spin-singlet pair due to the SP transition. Above $T = T_t$, as shown by a solid line in Fig. 3.1, $\chi(T)$ is well fitted to the characteristic curve for the $S = 1/2$ one-dimensional (1D) antiferromagnetic (AF) Heisenberg chain (so-called Bonner-Fischer curve [3.4]) with nearest-neighbor exchange interaction $J \sim 560$ K. Until now, many experiments [3.5] have established that the transition at $T = T_t$ is accompanied by the formation of spin-singlet pairs and a lattice distortion, both of which are necessary conditions for the SP transition.

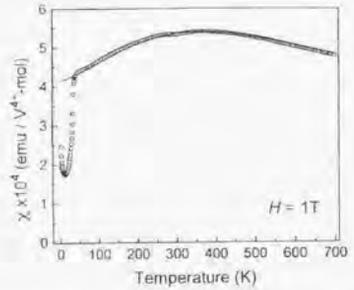

Figure 3.1: Magnetic susceptibility of NaV_2O_5 measured in a field of 1T over a wide temperature range. The solid line represents a fit to the Bonner-Fisher curve with $J \sim 560$ K [3.1]. A rapid decrease below $T = 34$ K implies the formation of a non-magnetic spin-singlet due to the SP transition.

NaV_2O_5 of an orthorhombic structure consists of layers (ab-planes) of VO_5 square pyramids isolated by inter-layer Na ions. The VO_5 pyramids running along the b-axis are sharing corners along the chain direction. Crystalographically, however, it is controversial whether the V atoms in the VO_5 pyramids are mixed-valent ($V^{4+} : V^{5+} = 1 : 1$) [3.3] or uniform-valent ($V^{4.5+}$) [3.6], as shown in Figs. 3.2 and 3.3, respectively. The former crystal has the non-centrosymmetric space group C_{2v}^7-$P2_1mn$ while the latter has the centrosymmetric space group D_{2h}^{13}-$Pmmn$. Nowadays the latter model has become more convincing due to recent reports on the several x-ray diffraction experiments for NaV_2O_5 [3.7, 8]. The lattice constants are reported to be $a = 11.316$ Å, $b = 3.611$ Å, and $c = 4.797$ Å [3.6]. In the mixed-valent model, which had been widely believed since the first report by Carpy and Galy [3.3], this compound can be regarded as a half-filled chain. Figure 3.4 (a) schematically represents a chain of $S = 1/2$ spins localized on the V^{4+} ions running along the b-axis in parallel with an empty chain consisting of V^{5+} ions. In this picture, reflecting the fact that the VO_5 pyramids share corners, this system is expected to behave as an ideal 1D AF system or, in other word, a 1D half-filled MH system with the nearest-neighbor exchange interaction of J. This explains the behavior of $\chi(T)$ at $T \gg T_t$ and, at the same time, the transition is also understood within this scheme, being much simpler than $CuGeO_3$ [3.9]. In the uniform-valent case, whose possibility was suggested by the crystal structure study [3.6] and the NMR study [3.10], NaV_2O_5 is viewed as a quarter-filled ladder system. From this viewpoint, the transition at $T = T_t$ may well be explained as a transition into a specific kind of charge-ordered phase from the uniform phase rather than as a simple SP transition [3.11–14].

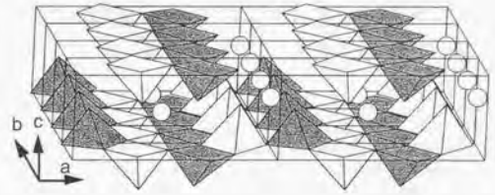

Figure 3.2: Crystal structure of α'-NaV_2O_5 in the mixed-valent model [3.3]. The $V^{4+}O_5$ and $V^{5+}O_5$ pyramids running along the b-axis are shown by white and dark-shaded square pyramids, respectively. The row of the $V^{4+}O_5$ pyramids forms a chain. Open circles indicate interlayer Na^+ ions.

The energy bands of NaV_2O_5 based on the uniform-valent case were obtained within density functional theory using the local-density approximation (LDA) [3.6]. The calculated energy dispersions and the density of states of the V $3d$ bands are shown in Fig. 3.5. According to the tight-binding analysis of this result, the bands of d_{xy} character labelled as a form a pair of bonding and anti-bonding bands of the ladder[2]. While the result of the calculations predicts this compound to be metallic, reflecting that each V ion has 0.5 $3d$ electron, the inclusion of electron correlation effects within the

[1] $Na_xV_2O_5$ composes a series of vanadium bronzes with five phases as a function of x such as α'-$Na_xV_2O_5$ ($0.70 \leq x \leq 1$), β-$Na_xV_2O_5$ ($0.22 \leq x \leq 0.40$) and so on [3.1].

[2] Since there are two weakly-coupled ladders in a unit cell, the number of the bands denoted by a is not two but four, which is not intrinsic here.

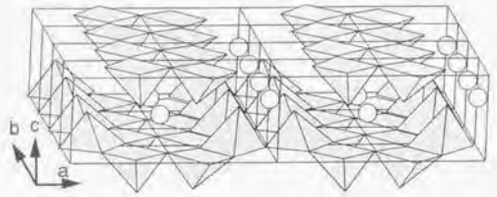

Figure 3.3: Crystal structure of α'-NaV_2O_5 in the uniform-valent model [3.6]. The $V^{4.5+}O_5$ pyramids running along the b-axis are shown by the gray-shaded square pyramids. The pair of two chains forms a ladder. Open circles indicate interlayer Na ions.

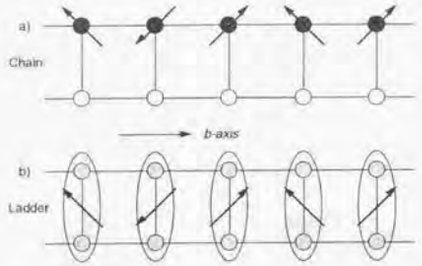

Figure 3.4: Ladder structure in the vanadium planes of NaV_2O_5. Only vanadium atoms are shown with each line corresponding to a V-O-V bond. (a) The mixed-valent case (see Fig. 3.2). Open and black circles represent V^{5+} and V^{4+} ions, respectively. (b) The uniform-valent case (see Fig. 3.3). The ovals represent the V-O-V molecular orbitals in the rung. Gray circles represent $V^{4.5+}$ ions.

V $3d$ bands would lead to the experimentally observed insulating behavior. Consequently, the bonding band can be thought to be half-filled, forming a 1D AF Heisenberg system with the spin 1/2 per rung as schematically shown in Fig. 3.4 (b), which explains the behavior of $\chi(T)$ well above T_t. In this sense, NaV_2O_5 is mapped onto a half-filled MH insulator [3.6]. Such a treatment starting from the V-O-V molecular orbitals has also been made in Ref. [3.11].

The difference between these two models is significant around or below T_t in terms of the charge ordering pattern. What kind of pattern is realized at low temperature is an unsettled problem being under intensive study [3.12-15]. Indeed, the possibility is not limited to the two types shown in Fig. 3.4. On the other hand, there is general agreement that NaV_2O_5 behaves as an ideal 1D AF Heisenberg chain well above T_t, which is supported both experimentally and theoretically as stated above.

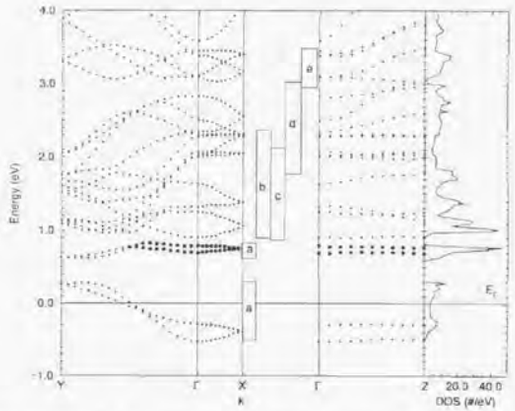

Figure 3.5: V $3d$ band dispersions and density of states of NaV_2O_5 [3.6]. a–e denote the d_{xy}, d_{yz}, d_{zx}, $d_{x^2-y^2}$, and $d_{3z^2-r^2}$ orbitals, respectively. Note that this result without electron correlation predicts metallic behavior for NaV_2O_5.

Now, it is of great interest how the excitation spectra of a 1D AF Heisenberg chain behaves, because the most basic but far from trivial is the excitation spectra of the 1D AF chain among various quantum-spin systems such as spin-ladder, Haldane, spin-Peierls and frustrated Heisenberg systems. Theoretical work on its excitation spectra based on the Hubbard model or t-J model has shown signs of spin-charge separation: as a result of one-dimensionality, the degrees of freedom of an electron are decoupled into spin-like and charge-like elementary excitations called "spinon" and "holon", respectively [3.16, 17]. The discovery of the high-T_C cuprates has invoked renewed interest in this phenomenon because of possible relationship between the spin-charge separation and the mechanism of high-T_C superconductivity [3.18].

Angle-resolved photoemission spectroscopy (ARPES) is a powerful technique in that the observed momentum-resolved spectra can be directly compared with theoretical single-particle excitation spectra. Kim *et al.* [3.19] performed a pioneering ARPES study on the 1D charge-transfer (CT) insulator $SrCuO_2$ and found that the spectra agree well with the theoretical one-particle spectra of the 1D t-J model with realistic parameters, identifying such spinon and holon excitations, as will be described in detail below. Since the t-J model is an effective low-energy Hamiltonian of the more realistic but complicated p-d model for the Cu-O chain, it is natural to ask whether simpler MH systems [3.20] can be described by the Hubbard model.

In this section, we have briefly described the physical properties of NaV_2O_5 and discussed its behaviors as a 1D MH system. Our scope in this chapter is to present the ARPES results on NaV_2O_5 including finite-temperature effects and to investigate how the characteristic features of a 1D MH system appears in this compound. After having described experimental details in Sec. 3.2, we present experimental results of x-ray photoemission spectroscopy (XPS) and ARPES studies of $Na_xV_2O_5$ ($x = 0.96$ and 1) in Sec. 3.3. In Sec. 3.4, theoretical calculations on the excitation spectra using the 1D t-J model at finite temperatures are shown. Finally, we make a quantitative comparison between theory and experiment in Sec. 3.5.

3.2 Experiment

Single-crystal stoichiometric NaV_2O_5 samples and Na-deficient $Na_xV_2O_5$ ($x = 0.96$) samples were provided by Prof. Y. Ueda and Dr. M. Isobe of ISSP, University of Tokyo. The Na-deficient $Na_{0.96}V_2O_5$ has almost the same magnetic properties as NaV_2O_5 except that the phase transition is suppressed [3.21]. Nearly the same magnetic behavior above T_t of the two compositions is reasonable because the 4 % Na deficiency would have negligible effect on the spin correlation because of the short correlation length (ξ_{AF}) above $T \sim T_t$ [3.22]. Though remaining an insulator, $Na_{0.96}V_2O_5$ is more conductive than NaV_2O_5 due to the doped holes as shown Fig. 3.6, which favored our experiments as described below. Theoretically, a correlated 1D MH system is insulating only when it is half-filled [3.16] and, therefore, the insulating behavior of the "hole-doped" $Na_{0.96}V_2O_5$ is self-trapping presumably caused by the potential disorder due to the Na vacancies or the electron-lattice coupling.

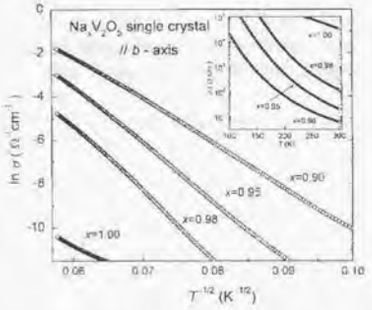

Figure 3.6: Logarithm of the electrical conductivity plotted against $T^{-1/2}$ of $Na_xV_2O_5$. The inset shows the resistivity [3.21].

Single crystals of NaV_2O_5 were prepared by the self-flux method. After having prepared powder samples of $Na_{0.96}V_2O_5$ by the solid-state reaction of mixtures with appropriate molar ratios of $NaVO_3$, V_2O_3 and V_2O_5 [3.1], single crystals of $Na_{0.96}V_2O_5$ were obtained by heating a small crystal of stoichiometric NaV_2O_5 embedded in a large quantity of the powder sample of $Na_{0.96}V_2O_5$ in an evacuated silica tube at 650°C for a week [3.23]. Typical size was $\sim 1 \times 0.5 \times 3$ mm^3.

The XPS measurements were performed for stoichiometric NaV_2O_5 using the Mg Kα line (photon energy $h\nu = 1253.6$ eV) and a PHI double-pass cylindrical-mirror analyzer with the energy resolution of ~ 1 eV. Samples were scraped *in situ* with a diamond file. The base pressure in the XPS spectrometer was $\sim 6 \times 10^{-10}$ Torr. The measurements were performed at room temperature in order to avoid charging effect. Calibration and estimation of the instrumental resolution were done using gold evaporated on the sample surface defining Au $4f_{7/2} = 84.0$ eV. The total resolution was ~ 1 eV, including both the light source and the instrumental resolution.

We took Laue photographs of all the samples to fix the crystal orientations before ARPES measurements. The single crystals could be cleaved parallel to the ab plane to give mirror-like surfaces. For the surfaces cleaved *in situ*, we detected the laser reflection from the sample surface to calibrate angles normal to the surface. ARPES measurements using the He I and He II resonance lines ($h\nu = 21.2$ and 40.8 eV, respectively) emitted from a Vacuum Generator discharge lamp were made using a VSW hemi-spherical analyzer. The angular and energy resolution of our operation were $\pm 1°$ and $\sim 80 - 100$ meV, respectively. We also did angle-integrated photoemission spectroscopy (AIPES) measurements for the samples scraped *in situ* with a diamond file. The scraped surfaces are supposed to reflect no crystal symmetry, giving us information about the momentum-integrated density of states (DOS). Calibration was done using the position of the Fermi edge of gold evaporated on the sample surfaces. Measurements for NaV_2O_5 were done only at room temperature (300 K), below which severe charging effect prohibited us from doing measurements. As mentioned above, non-stoichiometric $Na_{0.96}V_2O_5$ is more conductive than NaV_2O_5, which made it possible for the measurement temperature to range from $T = 120$ K ($\sim 0.21J \gg T_t$) to room temperature 300 K ($\sim 0.54J$). Temperature was controlled within the accuracy of ± 0.5 K. We checked that measurements were possible until down to 80 K. The measurements were performed for several times for different sample surfaces to confirm the reproducibility of the results. Furthermore, for $Na_{0.96}V_2O_5$, we carefully cycled the temperatures of cleavage and measurements in order to exclude any extrinsic effects such as surface degradation and contamination, which may build up with time after cleaving. To avoid any charging effects, the intensity of light from the discharge lamp was set as weak as possible. The base pressure of the analyzer chamber was below 1×10^{-10} Torr.

3.3 Results

3.3.1 Core-Level Spectra

In the top panel of Fig. 3.7 is shown the XPS spectrum of the V $2p_{1/2,\,3/2}$ and O 1*s* core levels for NaV_2O_5. The nearly symmetric shape of the O 1*s* core-level peak indicates high quality of the sample. For comparison, the spectra of the core levels of V_2O_5 and β-$Na_{0.33}V_2O_5$ (samples supplied by Profs. M. Onoda and H. Nagasawa) are also plotted in the bottom panel of Fig. 3.7. They have been shifted so as to match their O 1*s* core-level positions to that of NaV_2O_5. V_2O_5 has no 3*d* electron while β-$Na_{0.33}V_2O_5$, a member of the vanadium bronzes, has nominally $3d^{0.17}$ electron if Na is fully ionized. In Fig. 3.7, the V $2p_{3/2}$ core-level position of V_2O_5 is marked by "A". While peak A also exists in common in the spectra of NaV_2O_5 and β-$Na_{0.33}V_2O_5$, the latter compounds have another feature labelled as "B" in the figure. Feature B is found to be only a weak shoulder in β-$Na_{0.33}V_2O_5$ but is as strong as A in NaV_2O_5. On the assumption that the ratio of the intensity between A and B is proportional to the nominal ratio between V^{5+} and V^{4+}, we could decompose the V 2*p* spectra into structures A and B as shown in Fig. 3.8, where the lineshape is convoluted with a Gaussian and a Lorentzian function which represent the instrumental resolution and the core-hole lifetime broadening, respectively. The fact that NaV_2O_5 and

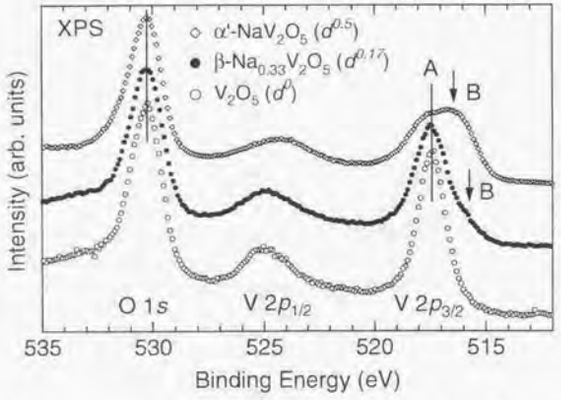

Figure 3.7: XPS spectra of the V 2*p* and O 1*s* core levels for α'-NaV_2O_5, β-$Na_{0.33}V_2O_5$, and V_2O_5. The peak labelled by A is commonly observed in all the spectra. The two arrows indicate the extra feature B of α'-NaV_2O_5 and β-$Na_{0.33}V_2O_5$ which is not observed in V_2O_5.

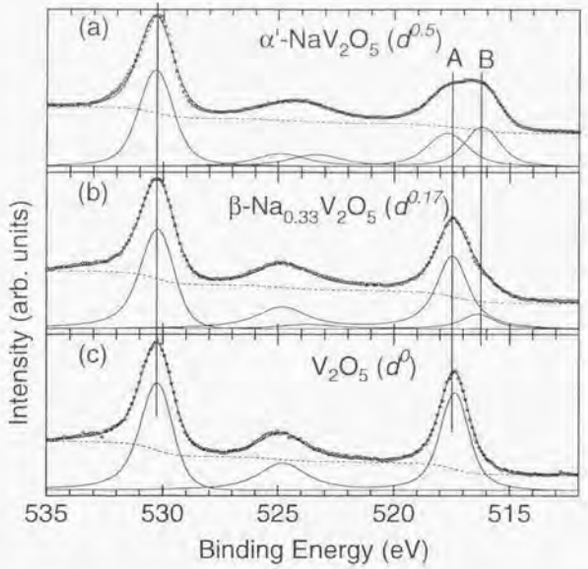

Figure 3.8: XPS spectra of the V 2*p* and O 1*s* core levels for (a) α'-NaV_2O_5, (b) β-$Na_{0.33}V_2O_5$, and (c) V_2O_5 with the results of decomposition into structures A and B. The fitted curve and decomposed curves corresponding to A and B origin are shown by lines. Dashed line shows the integral background.

β-$Na_{0.33}V_2O_5$ have component B at almost the same position supports the appropriateness of the decomposition. Hence, A and B are attributed to signals from V^{5+} and V^{4+}, respectively. This result is consistent with the x-ray absorption spectroscopy (XAS) measurement at the V *K*-edge (5.465 keV for vanadium metal) [3.15], which is a bulk-sensitive probe. The consistency between both, therefore, indicates that the mixed valence observed in the XPS spectra is not due to the surface effect.

It must be noted here that the above observations do not necessarily mean that the V atoms are *statically* in the mixed valent state. On the contrary, as shown in Fig. 3.9, according to the NMR measurement for ^{51}V [3.10], only a single V site is observed above $T = T_t$ while two V sites clearly appear below the transition temperature against the mixed-valent model above $T = T_t$. This is explained as due to the different time scales of the different measurements: NMR is a slow probe of order $\sim 10^6$–10^7 Hz, while measurements using x-rays are much faster probes of order $\sim 10^{16}$ Hz and detect V^{5+} and

V^{4+} separately. Our observation, therefore, does not contradict with both of the possible crystal structures introduced in Sec. 3.1. In the uniform-valent case, where the V-O-V rung forms a molecular orbital, NMR detects a single V site within the time scale of NMR while measurements using x-rays detect more than one V site due to their fast time scale, if the time scale of the electron transfer between the V atoms falls between $\sim 10^6$ and 10^{16} Hz.

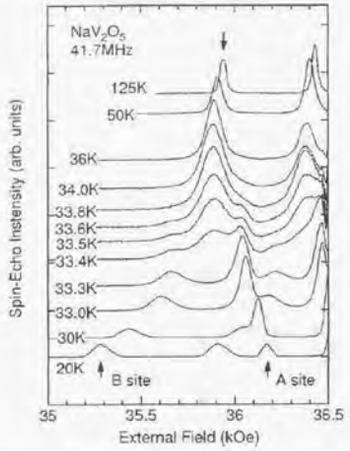

Figure 3.9: Temperature dependence of the NMR spectrum around T_i of a single crystal NaV_2O_5 [3.10]. Only signals from single V sites are observed above $T = T_i$ while the signals clearly split into two as indicated by "A" and "B" below the transition temperature.

3.3.2 Electronic Structure in the Entire Valence-Band Region

Figure 3.10 shows the AIPES spectra of NaV_2O_5 measured using He I ($h\nu = 21.2$ eV) and He II ($h\nu = 40.8$ eV) at 300 K. The background due to secondary electrons has been subtracted for the He I spectrum. The prominent features at $E_B = 3$–8 eV are the O $2p$ band while the weaker structures between 0 and 3 eV are the V $3d$ band. There are three distinct structures in the O $2p$ band at $E_B \sim 4$, ~ 6, and ~ 7 eV as indicated by the vertical bars in the figure. The difference in the intensity ratios of the structures for the different photon energies reflects the strength of hybridization between the O $2p$ and V $3d$ orbitals. Since the photoionization cross-section per V $3d$ electron relative to O $2p$ electron is estimated to be ~ 0.7 at $h\nu = 21.2$ eV and ~ 1.2 at $h\nu = 40.8$ eV [3.24], the structure around $E_B \sim 4$ eV,

which becomes weaker in comparison with the other two structures in going from $h\nu = 21.2$ to 40.8 eV, is thought of O $2p$ non-bonding character. The structures around $E_B = 5$–8 eV are of O $2p$-V $3d$ bonding character.

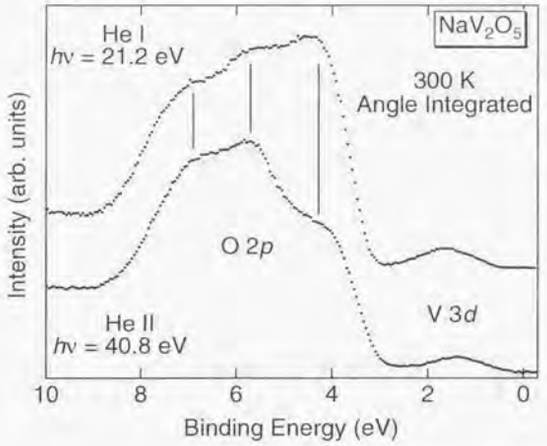

Figure 3.10: AIPES spectra of NaV_2O_5 measured using He I ($h\nu = 21.2$ eV) and He II ($h\nu = 40.8$ eV) at 300 K.

Figure 3.11 shows the geometry of the ARPES measurements and the definition of the take-off angles θ and ϕ of photoelectrons[3]. By scanning the momentum in the Brillouin zone (BZ) varying θ or ϕ, we obtained ARPES spectra along the $k \perp b$ and $k \parallel b$ cuts as indicated in Fig. 3.12. Hereafter, k_a and k_b are the momenta (Å^{-1}) along the a- and b- axes in units of the inverse of the corresponding lattice constant, respectively. ϕ and θ are related to the momenta k_a and k_b by

$$k_a = \frac{1}{\hbar}\sqrt{2m_e(-E_B + h\nu - W)}\sin\phi\cos\theta \tag{3.1}$$

and

$$k_b = \frac{1}{\hbar}\sqrt{2m_e(-E_B + h\nu - W)}\sin\theta, \tag{3.2}$$

where m_e is the electron mass and W the work function.

Figure 3.13 shows ARPES spectra in the entire valence-band region. The

[3]One of the angles (θ or ϕ) was controlled within the accuracy of $\pm 0.5°$ while the other was estimated from the reflection spot of the laser within the accuracy of $\pm 3°$, because only single axis can be controlled in our experimental setup.

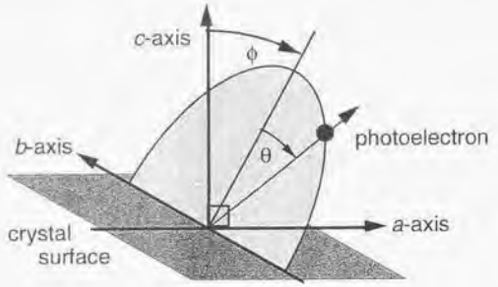

Figure 3.11: Definition of the take-off angles ϕ and θ of photoelectrons in the ARPES measurements.

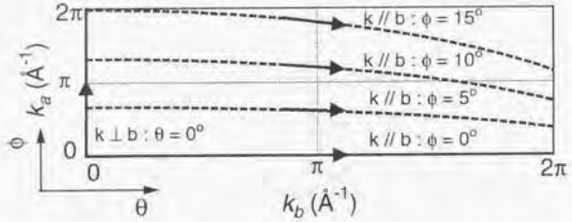

Figure 3.12: Various cuts in the BZ. By changing θ or ϕ, we can scan the momentum in the BZ as indicated by arrows.

upper panel shows the spectra with momentum parallel to the b-axis ($k \parallel b$), and the bottom panel those with momentum parallel to the a-axis ($k \perp b$). The spectra have been normalized to the area of the O $2p$ band between $E_B = 3$ and 8 eV. The $k \parallel b$ spectra in the upper panel of Fig. 3.13 clearly show dispersive O $2p$ features as marked by the dashed curves as a guide to the eye. Around the Γ point (take-off angle $\theta = \phi = 0°$) the spectra have three distinct peaks, consistent with the AIPES spectra. In contrast with this observation, the $k \perp b$ spectra in the bottom panel are nearly independent of angle. A slight modulation of the positions of spectral features does not reflect the BZ symmetry along the a-axis, indicating that this is due to a gradual variation of the photoemission matrix elements with the take-off angle. The clear contrast between the upper and bottom panels of Fig. 3.13 supports the view that NaV_2O_5 has a highly anisotropic electronic structure with sizable dispersions only along the b-axis. This strong anisotropy is

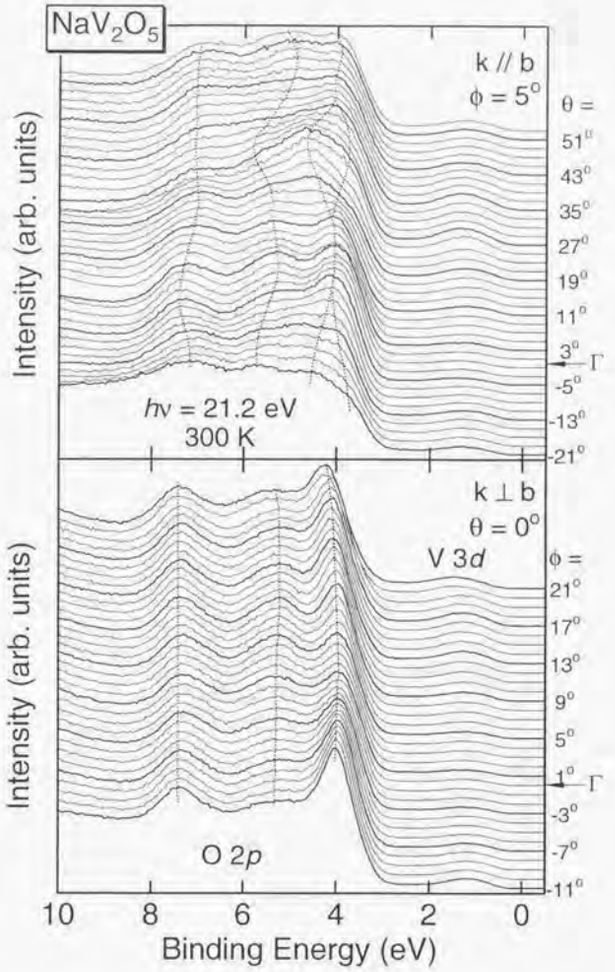

Figure 3.13: ARPES spectra of NaV_2O_5 for various take-off angles θ and ϕ. Upper panel: $k \parallel b$-axis. Lower panel: $k \perp b$-axis. The dashed lines are determined by the second derivative of the spectra, emphasizing the dispersing features of the O $2p$ bands.

not obvious from the crystal structure alone, however, because it has a two-dimensional V-O network in the ab-plane [see Figs. 3.2 and 3.3]. Presumably, the dispersions of the O $2p$ bands are predominantly caused by hybridization with the V $3d$ states, which are arranged in the one-dimensional way.

Next, we compare these results with those of $Na_{0.96}V_2O_5$. In Fig. 3.14, ARPES spectra of $Na_{0.96}V_2O_5$ in the entire valence band measured at 120 K and 300 K region are shown by the solid and dashed curves, respectively. By comparing between the $k \parallel b$ spectra (the upper panel of Fig. 3.14) and the $k \perp b$ spectra (the bottom panel of Fig. 3.14), the O $2p$ band structure was again found to be very anisotropic: the $k \parallel b$ spectra show rich dispersive features while those with momentum of $k \perp b$ have no dispersions, supporting the one-dimensionality of $Na_{0.96}V_2O_5$. The dispersive features of the O $2p$ band well agree with those of stoichiometric NaV_2O_5 described above, indicating that the small amount of Na deficiency has no appreciable influence on the O $2p$ band structure of $Na_{0.96}V_2O_5$. Furthermore, the O $2p$ spectra have no obvious temperature-dependent changes, except that the spectra at 300 K are somewhat broader than those at 120 K due to thermal broadening. This insensitivity to the temperature of the O $2p$ band makes a clear contrast to the remarkable changes of the V $3d$ band described below.

Using Eqs. (3.1) and (3.2), we have obtained the experimental band structure at 120 K for the O $2p$ band along the $k \parallel b$-axis and the $k \perp b$-axis as shown in Figs. 3.15 (a) and (b), respectively. The band structures are indicated by the open circles whose positions and sizes are determined by the negative peak positions and their strengths of the second derivatives of the original spectra, respectively. The intensity plots derived from the second derivatives of the original spectra are also shown in gray scale in Figs. 3.15 (a) and (b), where white part indicates the position of the bands. Solid curves show the dispersing features of the O $2p$ band thus obtained. While the band structure derived from the spectra of 300 K is somewhat broader than that at 120 K due to thermal broadening, both are consistent with each other. Around the Γ point the electronic structure along the $k \parallel b$-axis consists of three distinct bands centered at $E_B \simeq 3.7$, ~ 5.4 and ~ 7.0 eV. The band originated around $E_B \simeq 3.7$ eV at the Γ point disperses toward $k = \pi$ with splitting. The other parts starting from $E_B \simeq 5.4$ eV and ~ 7.0 eV at the Γ point also disperse toward $k = \pi$ point. In contrast, the $k \perp b$ spectra in Fig. 3.15 (b) are almost independent of momentum k_z. This supports the view that $Na_{0.96}V_2O_5$ still has a highly anisotropic electronic structure with sizable dispersions only along the b-axis in spite of the Na deficiency[4].

[4]While some results of the band-structure calculations for NaV_2O_5 were recently reported [3.25, 26], no calculations are available for the dispersion of O $2p$ band of this system.

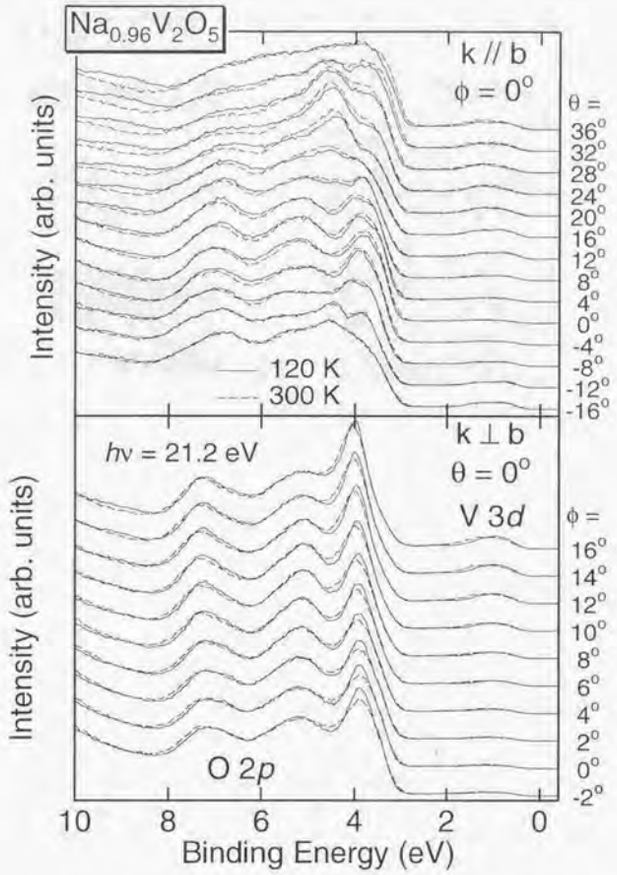

Figure 3.14: ARPES spectra of $Na_{0.96}V_2O_5$ for various take-off angles θ and ϕ. Upper panel: $k \parallel b$-axis. Lower panel: $k \perp b$-axis. Small structures appearing around $E_B = 9$ eV in the $k \parallel b$ spectra at 120 K are probably due to some physisorption on the cooled sample surface, which was not found to influence the intrinsic band dispersions.

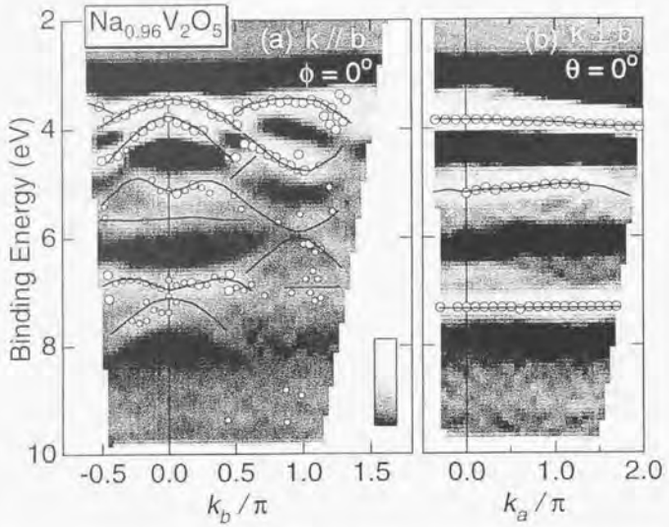

Figure 3.15: O $2p$ band structure of $Na_{0.96}V_2O_5$ along (a) the $k \parallel b$-axis and (b) the $k \perp b$-axis at 120 K. Open circles are the peak positions determined by the second derivative of the spectra, whose sizes are dependent on the intensities of the peaks. The background is not subtracted from the original spectra, which does not significantly influence the obtained band structure. We also superimposed the grey-scale plot of the second derivative of the spectra. Solid curves indicate the dispersing features of the O $2p$ band.

3.3.3 Electronic Structure in the V $3d$-Band Region

We first discuss the symmetry of the occupied V $3d$ orbital. Looking at both the $k \parallel b$ and $k \perp b$ spectra in Figs. 3.13 and 3.14, we notice that the intensity of the peak of V $3d$ character takes a minimum around the normal emission ($\theta = \phi = 0°$). To be more quantitative, the θ dependence $I(\mathrm{V}3d)/I(\mathrm{O}2p)$, where $I(\mathrm{V}3d)$ and $I(\mathrm{O}2p)$ are the area of the spectra around the V $3d$ band and the O $2p$ band, respectively, is plotted in Fig. 3.16[5]. The θ dependence of $I(\mathrm{V}3d)/I(\mathrm{O}2p)$ is shown for two kinds of BZ scan of $|\phi| < 5°$ and $|\phi| > 10°$ as plotted by closed and open circles, respectively. In the former case, the relative intensity at $\theta \sim 0°$ is as weak as almost half of the latter. This observation can be explained by the facts that the occupied V $3d$ orbital has approximately xy symmetry lying in the ab-plane [3.6, 27] and

[5]We do not discuss the effect of the photoelectron diffraction in this figure. The plot is meaningful only at $|\theta| < 10°$.

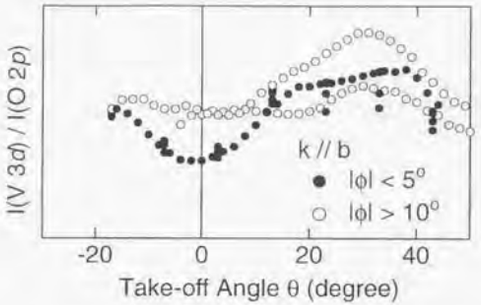

Figure 3.16: θ dependences of $I(\mathrm{V}3d)/I(\mathrm{O}2p)$ for two kinds of BZ scan of $|\phi| < 5°$ and $|\phi| > 10°$ are plotted by closed and open circles, respectively.

therefore that normal emission from this orbital is forbidden due to selection rules [3.28]. The full explanation is as follows: The photoemission intensity I is proportional to $|\langle f|p|i\rangle|^2$, where $|i\rangle$, $|f\rangle$, and p are the initial state, the final state, and the momentum in the dipole operator. Now, we focus on the the photoelectron emission from the V $3d$ orbital in the direction normal to the ab plane. In the one-electron description, $|i\rangle \propto |3d\rangle|\Psi_0^{N-1}\rangle$ and $|f\rangle \propto |e^{ikz}\rangle|\Psi_n^{N-1}\rangle$ hold [3.28] (also see Sec. 2.1) where $|e^{ikz}\rangle$ represents the wavefunction of the photoelectron emitted normal to the ab plane. By noticing the so-called m-selection rule of Wigner-Eckart's theorem [3.29], the matrix element $\langle e^{ikz}|p|3d\rangle$ is zero when $|3d\rangle \propto xy$, while it is not zero when $|3d\rangle \propto yz$ or zx.

It is noted that the origin of the weak but finite intensity for the normal emission, which shows no temperature dependence as we shall see below, may be explained by the tilting of the VO_5 pyramids from the ab plane [3.3] or by the background due to scattered electrons as observed in cuprates [3.19].

Figures 3.17 (a) and (b) show the result for the $k \parallel b$ cut with $\phi = 15°$ measured at 120 K and 300 K, respectively. By scanning such a cut, we could avoid the Γ point where the matrix-element effects prohibit emission from d_{xy}. The four spectra plotted with thicker curves in each panel indicate the spectra taken at $k_b \simeq 0$, $\pi/2$, π, and $3\pi/2$. The V $3d$ band located between $E_B = 0$ and 2.5 eV is broad and shows no spectral weight at the Fermi level (E_F), reflecting its insulating behavior. The broad peak centered at $E_B \sim 1$ eV, which has also been observed in other vanadium oxides such as insulating $LaVO_3$ [3.30], metallic $SrVO_3$ and $CaVO_3$ [3.22, 23], would be attributed to the lower Hubbard band or its remnant feature, which is separated from the upper Hubbard band by the Coulomb repulsion energy U.

The obtained 120 K spectra show rich dispersing features. In going from

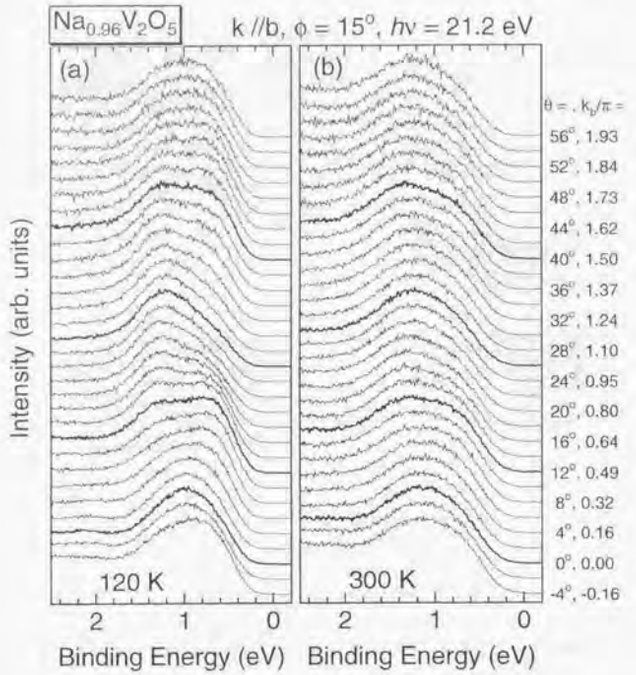

Figure 3.17: Spectra for a $k \parallel b$ cut measured at (a) 120 K and (b) 300 K. The four spectra plotted with thicker curves in each figure indicate the spectra at $k_b \simeq 0$, $\pi/2$, π, and $3\pi/2$.

$k_b = 0$ to $\pi/2$, a single peak centered at $E_B = 0.9$ eV is split into two features: the splitting becomes largest at $k_b = \pi/2$ with two features located at $E_B \sim 0.7$ and ~ 1.4 eV. The 0.7 eV peak then decreases in intensity in going from $k_b = \pi/2$ to π and only a single broad peak is left at $E_B \sim 1.1$ eV at the BZ boundary $k_b \sim \pi$. The k_b-dependence of the spectra between $k_b = 0$ and 2π is almost symmetric with respect to $k_b = \pi$, which excludes significant changes in the photoemission matrix elements between the first and second BZ's. By contrast, the 300 K spectra show less pronounced features than the 120 K spectra.

Figure 3.18 (a) shows a quantitative comparison between the 120 K spectra and the 300 K spectra of $Na_{0.96}V_2O_5$ obtained along $k \parallel b$. In Figs. 3.18 (b), (c), and (d), we present intensity plots derived from the 120 K spectra,

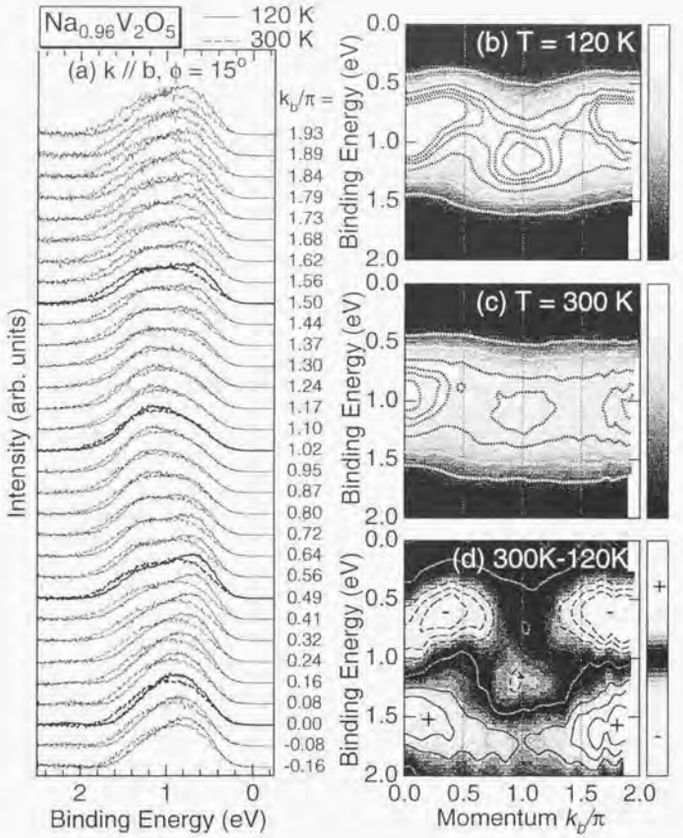

Figure 3.18: (a) Temperature dependence of the $k \parallel b$ spectra measured at 120 K and 300 K are shown by solid and dashed curves. They have been normalized to the area between $E_B = 0.0$ eV and 2.5 eV after having subtracted the integral background. The four spectra plotted with thicker curves in each figure indicate the spectra at $k_b \simeq 0$, $\pi/2$, π, and $3\pi/2$. (b) Intensity plot at 120 K. (c) Intensity plot at 300 K. (d) Intensity plot of the 300 K-120 K difference spectra.

the 300 K spectra, and the difference spectra between the 300 K and 120 K spectra, which will be referred to as the "300 K-120 K" spectra. In Fig. 3.18 (a), all the spectra have been normalized to the area of the lower Hubbard band of V $3d$ origin between $E_B = 0.0$ eV and 2.5 eV after having subtracted the integral background. In going from $T = 120$ K to 300 K, the spectra at $k_b = 0$ and π become a broader peak with a longer tail towards high binding energies. As for the spectra at $k_b \sim \pi/2$, the peak located at $E_B \sim 0.7$ eV becomes weaker and that at ~ 1.4 eV stronger in going from 120 K to 300 K. These observations are more clearly recognized in the intensity plots shown in Figs. 3.18 (b) and (c). The intensity plot of the 300 K-120 K difference spectra in Fig. 3.18 (d) clearly shows that spectral-weight transfer of order ~ 1 eV is caused by finite-temperature effects and that this phenomena occurs depending not only on the energy E_B but also on the momentum k_b. It must be emphasized here that the intensity plots shown in Figs. 3.18 (b), (c), and (d) clearly reflect the symmetry of BZ of this system, supporting that our observations are intrinsic. As shown in Fig. 3.19, we also performed ARPES measurements at 200 K and confirmed that the changes are gradual as a function of temperature in going from 120 K to 300 K being consistent with Fig. 3.18 (d).

These characteristic finite-temperature effects of the $k \parallel b$ spectra between 120 K and 300 K become more vivid through comparison with the result of the $k \perp b$ spectra. The $k \perp b$ cut in Fig. 3.20 (a) shows a clear temperature dependence and a weak angle dependence except for around the Γ point ($\theta = \phi = 0°$). In addition, the absolute intensity at the Γ point was found to be reduced to half of those at $\phi > 10°$ as shown Fig. 3.16. Considering the xy symmetry of the occupied V $3d$ orbital and the selection rules as mentioned above, we conclude that the obtained temperature dependence results from intrinsic finite-temperature effects of the V $3d_{xy}$ band and that the momentum dependence along the $k \perp b$ direction is due to the matrix element effects of the d_{xy} orbital. The intensity plots in Figs. 3.20 (b) and (c) support that there is only a slight k_a-dependence in the $k \perp b$ spectra except for around the Γ point, which makes clear contrast to those shown in Figs. 3.18 (b) and (c). The intensity plot of the 300 K-120 K difference spectra along the $k \perp b$ cut is also shown in Fig. 3.20 (d).

In addition to the discussion on the finite-temperature effects observed in $Na_{0.96}V_2O_5$, it is meaningful to compare the result of NaV_2O_5 with that of $Na_{0.96}V_2O_5$ taken at 300 K, whose intensity plots are shown in Fig. 3.21 (a) and (b), respectively. Although the spectra of the more insulating NaV_2O_5 are distorted toward higher E_B due to weak charging effect even at 300 K, the modulating feature observed in $Na_{0.96}V_2O_5$ is also seen in NaV_2O_5. Details of the results of NaV_2O_5 are described in Appendix A.

By noting that the finite-temperature effects strongly depend on the momentum ($k \equiv k_b$), they are clearly not due to simple thermal broadening or

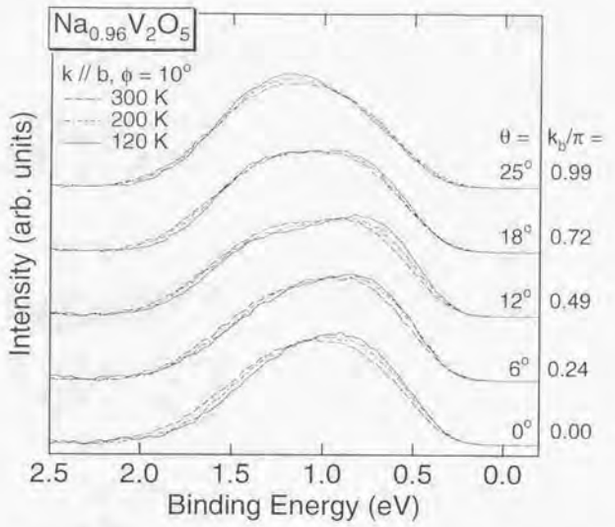

Figure 3.19: Temperature dependence of the $k \parallel b$ spectra at specific momenta $k_b \simeq 0$, $\pi/4$, $\pi/2$, $3\pi/4$, and π measured at 300 K, 200 K, and 120 K. The temperature-dependant changes are found to be gradual.

charging effects. The following two points are remarked:

1. In the temperature range studied here, there is no phase transition that may give rise to such a dramatic change.
2. The energy scale of the spectral change is not of order $kT \sim 0.03$ eV but of order ~ 1 eV. These phenomena are obviously beyond the conventional band picture and would reflect strong correlation effects.

As discussed in Sec. 3.1, this compound can be viewed as a 1D AF system at $T \gg T_1$ and, therefore, the experimental results could be interpreted as a manifestation of the nature of such a correlated system. In the rest of this chapter, we will interpret the spectra from this view point.

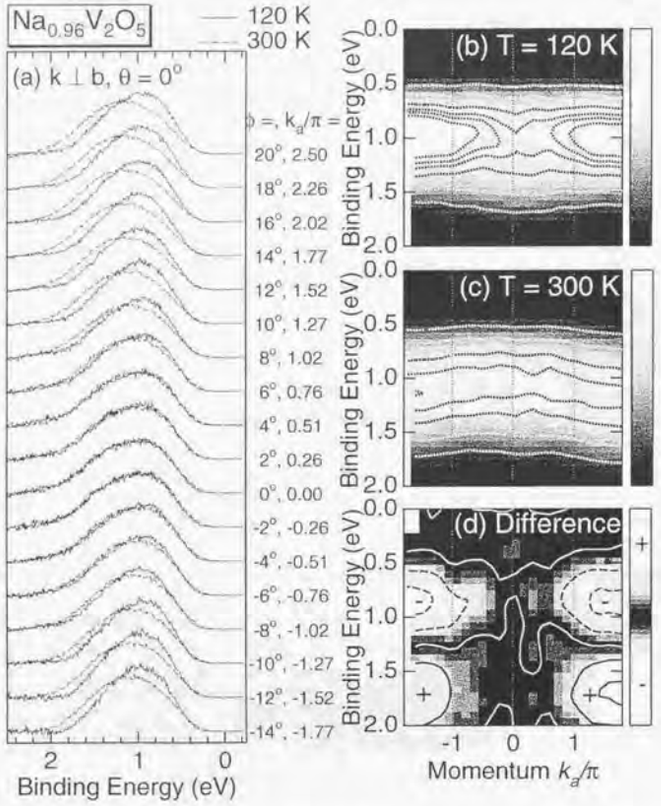

Figure 3.20: (a) Temperature dependence of the $k \perp b$ spectra. They have been normalized to the area between E_B = 0.0 eV and 2.5 eV after having subtracted the integral background. (b) Intensity plot at 120 K. (c) Intensity plot at 300 K. (d) Intensity plot of the 300 K-120 K difference spectra. Note that the spectra at $|\phi| > 10°$ are consistent with the $k \parallel b$ spectra at $\theta \sim 0°$.

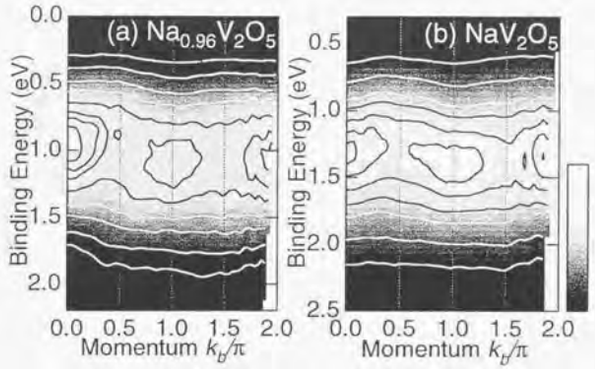

Figure 3.21: Comparison between the spectra of (a) $Na_{0.96}V_2O_5$ and (b) NaV_2O_5, both of which were measured at 300 K.

3.4 t-J Model Calculations of the Excitation Spectra of 1D AF Chain

Since Lieb and Wu [3.16] found that the degrees of freedom of an electron in 1D correlated systems are decoupled into collective spin and charge elementary excitations called spinon and holon, respectively, many theoretical studies on the excitation spectra have been performed based on the Hubbard model or t-J model. Parameters appearing in those models are the transfer integral t (> 0) between nearest neighbors, the on-site Coulomb energy U and the exchange coupling constant J ($\sim 4t^2/U$ for $U/t \gg 1$). The models are given by,

$$\mathcal{H}_{tJ} = -t \sum_{i\sigma} (\tilde{c}^{\dagger}_{i\sigma} \tilde{c}_{i+1\sigma} + H.c.) + J \sum_{i} S_i \cdot S_{i+1} \tag{3.3}$$

for the 1D t-J model and

$$\mathcal{H}_{Hubbard} = -t \sum_{i\sigma} (c^{\dagger}_{i\sigma} c_{i+1\sigma} + H.c.) + U \sum_{i} n_{i\sigma} n_{i-\sigma} \tag{3.4}$$

for the 1D Hubbard model, where $c_{i\sigma}$ is the annihilation operator of an electron with spin σ at site i, $\tilde{c}_{i\sigma} = c_{i\sigma}(1 - n_{i-\sigma})$, $n_{i\sigma} = c^{\dagger}_{i\sigma} c_{i\sigma}$, and S_i is the spin operator of an electron localized at site i. Sorella and Parola analytically obtained the single-particle excitation spectra in case of the $U \to \infty$ ($J \to 0$) 1D Hubbard model [3.17], starting from the so-called Ogata-Shiba wave function [3.33], which embodies the spin-charge separation. Their result is

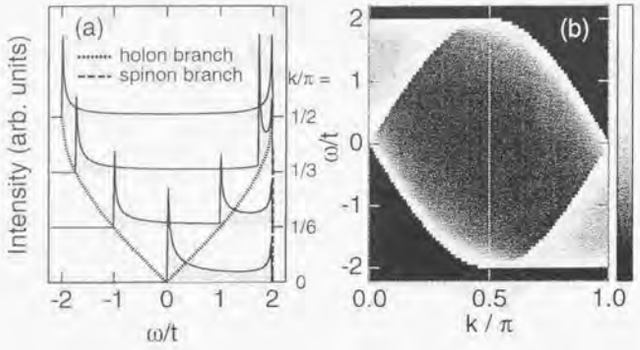

Figure 3.22: (a) Single-particle excitation spectra of the $U \to \infty$ ($J \to 0$) 1D Hubbard model at various k points. The dotted and dashed lines indicate the holon and spinon branches, respectively [3.17]. (b) The intensity plot of the same excitation spectra. Here, $E_0 = 0$.

shown in Fig. 3.22. Dotted and dashed lines indicate the holon and spinon branches, respectively. The holon dispersion has two branch cuts at

$$\omega(k) = E_0 \pm 2t \sin k \quad \text{for } 0 \le k \le \pi, \tag{3.5}$$

between which there exist continuum excitations. The spinon branch is located at

$$\omega(k) = \begin{cases} E_0 + 2t, & \text{for } 0 \le k < \pi/2 \\ E_0 - 2t, & \text{for } \pi/2 < k \le \pi \end{cases} \tag{3.6}$$

and has no dispersion for $J \to 0$. As will be discussed below in detail for finite U or J, by applying the exact diagonalization method, it has been found that the single-particle spectral function has spinon and holon branches whose energy scale is given by J and t, respectively [3.34–37].

Experimentally, an ARPES study has been reported for a 1D charge-transfer type insulator $SrCuO_2$ by Kim *et al* [3.19]. Parameters which characterize its electronic structure are $J \sim 0.2$ eV and $t = 0.60$ eV. The result is shown in Fig. 3.23. The left panel shows spectra between $k = 0$ and $\pi/2$, and the right panel shows spectra between $k = \pi/2$ and π. Here, k is momentum along the 1D axis of $SrCuO_2$. The main feature with a maximum at $k = \pi/2$ has a symmetrical dispersion toward $k = 0$ and $k = \pi$ with the width of ~ 1 eV. The dispersion is, however, asymmetric with respect to $k = \pi/2$: The spectra in the left panel show a broad feature centered around 0.5 eV, while the spectra in the right panel show no such features. Kim *et al.* assigned the main feature to the holon band and the broad feature to the spinon band.

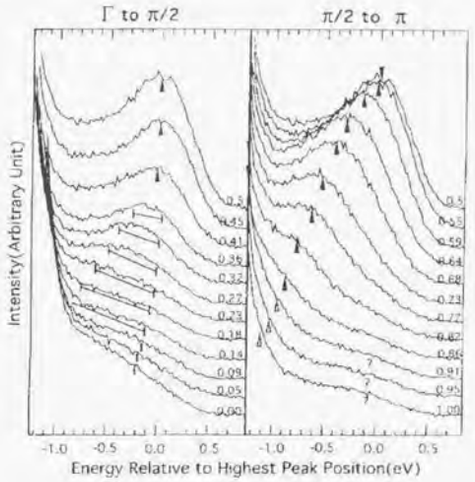

Figure 3.23: ARPES spectra from $SrCuO_2$. The left panel has spectra from k positions between Γ and $\pi/2$ and the right panel from $\pi/2$ to π. Different marks are guides to the eye. The solid triangles are used for the peaks which are certain and the question marks when there is some ambiguity. The spectra in the left panel show a broad feature which implies that there may exist multiple features. The line segments indicate the upper and lower bounds for the dispersive features [3.19].

This agrees well with calculations on the 1D t-J model at $T = 0$ with t and J appropriate to this compound, exhibiting such spinon and holon excitations. The theoretical calculations correspond to the results at $T = 0$ shown in Fig. 3.24.

Unlike $SrCuO_2$ with large $J \sim 2000$ K, finite-temperature effects can be more significant in the NaV_2O_5 system because the changes in the measurement temperature can become of order $J \sim 560$ K, which is the parameter characterizing excitations on the low energy scale. The 1D t-J model has been adopted to calculate the one-particle spectral function $A(k,\omega)$ at finite temperatures by the exact diagonalization method [3.38]. As the behavior of $\chi(T)$ well above T_t indicates, the t-J model is valid as one of the simplest models to describe this system in the temperature region considered. It may be applicable not only to the half-filled chain case [3.1, 3], but also to the quarter-filled ladder case where each d electron is localized in a rung consisting of two V atoms [3.6, 10]. In the ladder case, only the half-filled bonding band is taken into account because no electrons are in the antibond-

ing band [3.6]. The quarter-filled ladder can be mapped on to the half-filled chain if one considers only the half-filled bonding band and by an appropriate modification of the parameters t and J [3.6, 11]. In addition, the t-J model has the advantage over the more realistic Hubbard model in that the former can treat larger clusters, which is crucial for the discussion of finite temperature effects. The spectral function $A(k,\omega)$ is given by

$$A(k,\omega) = \frac{1}{Z}\sum_{f,\sigma} e^{-\beta E_i^N} |\langle f, N-1|c_{k\sigma}|i,N\rangle|^2 \times \delta(\omega - E_i^N + E_f^{N-1}), \quad (3.7)$$

where $Z = \sum_i e^{-\beta E_i^N}$ is the partition function. Figure 3.24 shows the results for a half-filled 14-site t-J cluster with $J/t = 1/3$ at $T = 0$, $J/4$, and $J/2$ calculated by Profs. T. Tohyama and S. Maekawa of IMR, Tohoku University.

Here, we would like to add some technical comments on the calculations. In the one-dimensional t-J model, a 14-site cluster is large enough for studying the spinon and holon structures in $A(k,\omega)$ at zero temperature. At finite temperatures, however, the energy-level spacing between the ground state and low-energy excited states should be checked carefully due to the small size of the cluster. Because the energy separation between the ground and first excited states is roughly $J/4$, we can say that reliable results are obtained in the region $T \geq J/4$. The two temperatures $T = J/4$ and $J/2$, where the comparison between experiment and theory will be made, fall within this region. Additionally, Na vacancies in $Na_{0.96}V_2O_5$ are more sparsely distributed than the cluster size used for the exact diagonalization calculation, which justifies our quantitative comparison hereafter.

At $T = 0$, the spectral function $A(k,\omega)$ can be intuitively interpreted as a convolution of spinon and holon spectral functions, as is schematically drawn in Fig. 3.25 [3.19]. When one electron is removed from the 1D AF chain through the photoemission process, one photohole left behind is split into two objects and propagates along the chain. One is the charge defect called holon with the hopping energy t and the other is the spin kink called spinon with the exchange energy J. Hence, both of them have their own energies and momenta under the constraints:

$$k = k_h - k_s, \quad (3.8)$$

where k, k_s, and k_h are the momenta of the photohole, spinon, and holon, respectively, and

$$E = E_h - E_s, \quad (3.9)$$

where E, E_s, E_h are the energies of the photohole, spinon, and holon, respectively. This argument is based on the fact that the spin part of the t-J Hamiltonian can be transformed into an interacting spinless fermion system through the Jordan-Wigner transformation. In this scenario, a holon can be

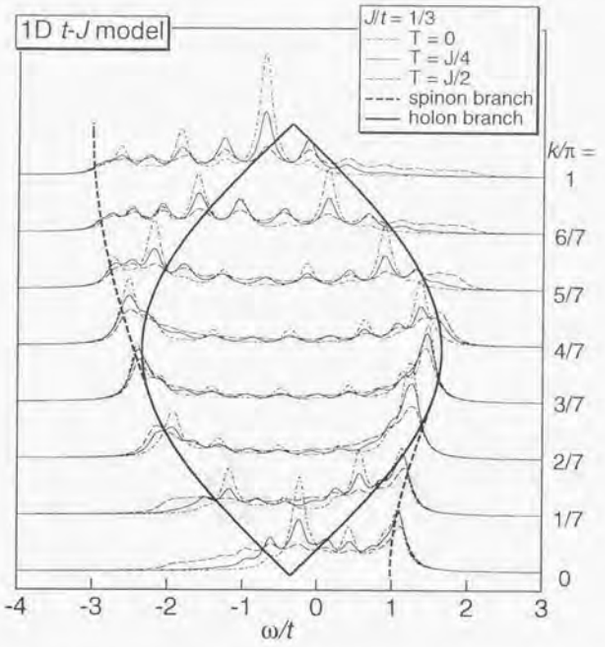

Figure 3.24: Spectral function of the half-filled 14-site t-J model with $J/t = 1/3$ at various temperatures calculated by Profs. T. Tohyama and S. Maekawa. The thick solid and dashed curves indicate the singularities of the spinon and holon branches, respectively.

viewed as a spinless fermion occupying an empty band of the width of $4t$, while a spinon corresponds to a hole in the half-filled band with the width πJ whose Fermi momentum[6] is located at $k_s = \pi/2$ and $3\pi/2$ as shown in Fig. 3.26 (a) and (b) [3.19]. Thus, the spectral function is obtained through a convolution of spinon and holon excitations under the constraint of Eqs. (3.8) and (3.9) as shown in Fig. 3.26 (c). The lineshape of the spinon branch is determined by the band edge singularity of the holon band at $k_h = 0$, π

[6]The term "Fermi momentum" and "Fermi surface" which will be used below might not be appropriate in the strict sense, because the distribution function of spinons is not of a Fermi-Dirac function. In fact, its temperature dependence is theoretically unclear at this moment. Nevertheless, there is an energy cut-off at $k_s = \pi/2$ and $3\pi/2$, which could be compared to a Fermi surface, and the Fermi surface will be blurred over the energy scale $\sim kT$ at finite temperatures [3.19, 40].

and 2π, whereas that of the holon branch is determined by the Fermi edge singularity of the spinon band at $k_s = \pi/2$ and $3\pi/2$ [3.17, 39].

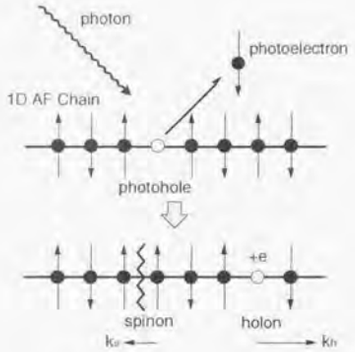

Figure 3.25: Schematic diagram of the photoemission process in a 1D AF chain. The degrees of freedom of the created photohole are split into a spinon and a holon with different velocities [3.19]. In the case where NaV_2O_5 is treated as a quarter-filled ladder system, the sites shown by circles correspond to the V-O-V molecular orbitals in the rung as shown in Fig. 3.4.

At finite temperatures, the existence of the Fermi surface of spinon excitations makes significant influence on the excitation spectra [3.40]. In fact, the singularity of the holon branch due to the existence of the spinon Fermi surface is easily smeared out over the entire energy range of $4t$ ($\gg T \sim J$) at finite temperatures of order J [3.40]. As shown in Fig. 3.26 (d), the spectral weight of the spinon branch labelled as α (β) is transferred from $0 < k < \pi/2$ ($\pi/2 < k < \pi$) to $\pi/2 < k < \pi$ ($0 < k < \pi/2$). At the same time, the intensity of the holon branch decreases. The lost spectral weight is transferred from the spinon branch to a wide energy region, making the spectral features less pronounced and more symmetric with respect to $k = \pi/2$.

3.5 Discussion

Now we make a comparison between the experimental and theoretical spectra. Figure 3.27 (a) shows experimental spectra for selected momentum values. Figures 3.27 (b) and (c) show the intensity plot in the E-k plane on the grey scale. Correspondingly, we show in Figs. 3.27 (d)–(f) the theoretical spectra at $T = J/4 \sim 150$ K (solid lines) and $T = J/2 \sim 300$ K (dashed lines) after Gaussian broadening with the width $2.5t$ and their intensity plots. Here, we have assumed that $t = 3J = 0.15$ eV, which is plausible because

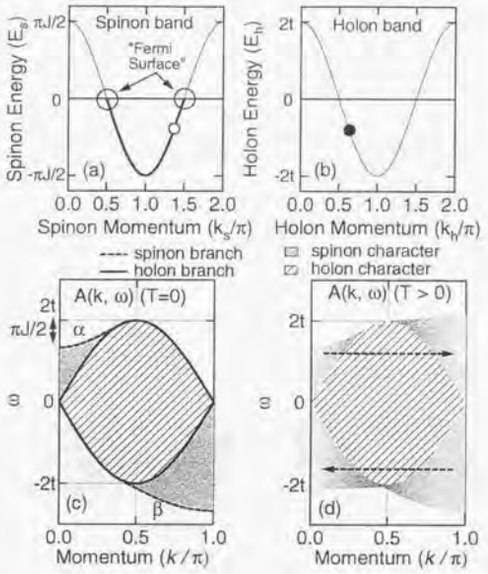

Figure 3.26: (a) Open circle denotes a spinon as a hole in the half-filled spinon band. (b) Closed circle is a holon as a spin-less fermion in the empty holon band. (c) Spectral function obtained through a convolution of the spinon band and the holon band [3.19]. (d) At $T > 0$, the intensities at the holon and spinon branches decrease and the lost spectral weight is transferred to the directions indicated by arrows.

$J = 4t^2/U \sim 0.05$ eV [3.1] and $U = 2$–4 eV in typical vanadium oxides [3.23, 41]. Comparing (a)–(c) and (d)–(f), overall agreement between experiment and theory is satisfactory. In the low temperature region ($T = 120$ K or $J/4$), the observed shift of the peak position between $k_h = 0.0$ and 0.95π may be attributed to the existence of the spinon branch, resulting in the asymmetry of the spectra with respect to $k = \pi/2$. Besides, between $k_h = 0.32\pi$ and 0.72π, there are two dispersing features, which may be assigned to the two holon branches as predicted in the theoretical spectra. These findings are also substantiated in the comparison between (b) and (e). Unlike the 1D cuprates, where the intense O $2p$ structure obscures the higher binding energy part of the holon and spinon branches [3.19], the whole structure of theoretical $A(k,\omega)$ can be compared with the experimental results of the present compound.

In the high temperature region ($T = 300$ K or $J/2$), both the experimen-

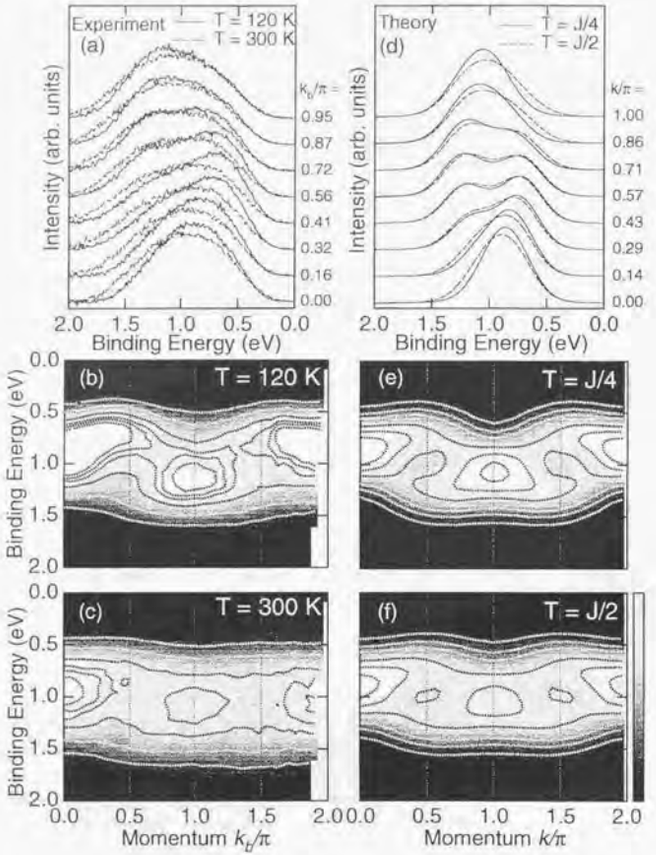

Figure 3.27: Comparison between the experimental and theoretical spectra. Panel (a) shows the ARPES spectra of $Na_{0.96}V_2O_5$ with the intensity plots in panels (b) and (c). Panels (d), (e) and (f) show the theoretical counterparts calculated for the half-filled 14-site t-J model. Here $J = 0.05$ eV.

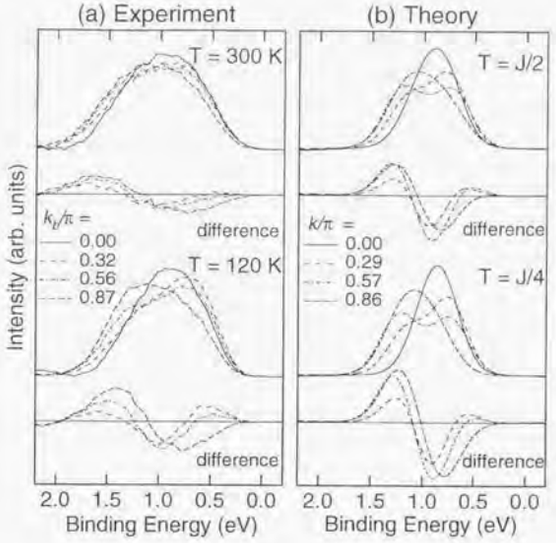

Figure 3.28: Spectra are plotted for $k = k_b \sim 0$, $2\pi/7$, $4\pi/7$, and $6\pi/7$. (a) Experiment. (b) Theory. The difference spectra from the $k = k_b = 0$ spectrum are also shown, emphasizing the dispersing part from the original spectra.

tal and theoretical results become broader and more symmetric with respect to $k = \pi/2$. The tendency of the experimental spectral weight redistribution due to finite temperature is grossly reproduced by the theory as seen in the intensity plots in Fig. 3.27. Around $k \sim 0$, agreement is excellent. In order to focus on the spectral weight transfer caused by the finite-temperature effects, the experimental and theoretical spectra are plotted one over another for $k = k_b \sim 0$, $2\pi/7$, $4\pi/7$, and $6\pi/7$ in Figs. 3.28 (a) and (b), respectively. The difference spectra from the $k = k_b = 0$ spectrum are also shown. The difference spectra thus obtained, which extract the dispersing feature from the original spectra in the E-k space, resemble between theory and experiment. To this extent, the experimental finite temperature effects may be attributed to the existence of the spinon Fermi surface, which theoretically causes the dramatic spectral redistribution over the entire E-k space with changing temperature.

To be more precise, however, there exist some discrepancies between theory and experiment. When the temperature is increased from 120 K to

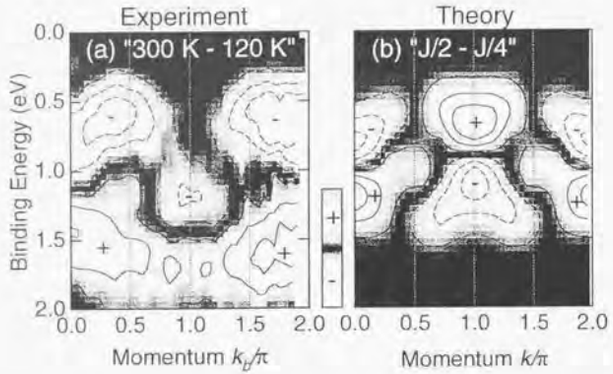

Figure 3.29: (a) Experimental intensity plot of the 300K-120K difference spectra. (b) Theoretical intensity plot of the "$J/2$-$J/4$" difference spectra. "+" and "-" indicate the sign of the difference.

300 K, the spectra change more dramatically than the theoretical prediction, as seen in the comparison between Figs. 3.28 (a) and (b) at 300 K. In Figs. 3.29 (a) and (b), the experimental and theoretical intensity plots of the difference between the high and low temperatures are shown. We notice that the finite-temperature effects influence the distribution of the spectral weight more widely in the E-k space than the calculations predict. Furthermore, while the temperature dependence is rather well simulated by theory at $k_b \sim 0$-0.32π, at $k_b \sim 0.5\pi$ the feature around $E_B = 0.7$ eV in experiment loses much of its spectral weight in going from 120 K to 300 K, in disagreement with theory. In addition, around $k_b \sim \pi$ in going from 120 K to 300 K, the experimental spectra lose spectral weight at $E_B < 0.8$ eV and a longer tail develops on the high binding energy side unlike the theoretical spectra. At low temperatures, where the decay of a photohole is probably dominated by purely electronic mechanisms while other decay channels may become available at higher temperatures. As a candidate, we may consider electron-phonon interaction and possible charge disorder [3.42], which may become important at higher temperatures. The difference between the t-J model and the Hubbard model as well as the degeneracy of the V $3d$ orbitals might be another origin for the discrepancy.

Another kind of discrepancy also exists between theory and experiment: The experimental spectra have much larger width than the theoretical spectra at both 120 k and 300 K, although the theoretical spectra have been already broadened by the Gaussian with the width $2.5t \sim 0.38$ eV. Since this

Gaussian broadening seems sufficient to phenomenologically take account of the instrumental energy and momentum resolutions and the lifetime of photoholes, the discrepancy still remaining in the spectral width should be attributed to the other causes. The possible origins which may broaden the experimental spectra are the effect of defects and the surface state. Defects, which inevitably exist on the cleaved surface, break the crystal symmetry locally, presumably resulting in the broadening of the ARPES spectra. The effects of surface states were recently discussed for other vanadium oxides $La_{1-x}Ca_xVO_3$ by Maiti *et al.* [3.43], who claimed that the broad structure around $E_B \sim 1$ eV in the ultraviolet photoemission spectra of such compounds have significant contribution from the surface state. Their observation may give a clue to the origin of the broadened structure of NaV_2O_5.

3.6 Conclusion

We have made an ARPES study of the 1D MH-type (or 1D AF) insulator NaV_2O_5 and $Na_{0.96}V_2O_5$. First, the ARPES spectra reveal that the gross electronic structure of the valence band is highly anisotropic. Second, we have made an ARPES study of $Na_{0.96}V_2O_5$ by changing the temperature and found that a strong spectral weight redistribution occurs in the lower Hubbard band. Also we have compared the ARPES spectra with the one-particle spectral function of the 1D t-J model at finite temperatures calculated by the exact diagonalization method. The overall agreement between theory and experiment implies that the spin-charge separation picture is valid in the excitation spectra of this system. Although they are more drastic than the theoretical prediction, the experimental finite temperature effects have been partly explained by the theory, which may be expressed as the Fermi surface effect of the spinon band.

References

[3.1] M. Isobe and Y. Ueda. J. Phys. Soc. Jpn. **65,** 1178 (1996).

[3.2] M. Hase, I. Terasaki and K. Uchinokura, Phys. Rev. Lett. **70,** 3651 (1993).

[3.3] A. Carpy and J. Galy, Acta Cryst. B **31,** 1481 (1975).

[3.4] J. G. Bonner and M. E. Fisher, Phys. Rev. **135A,** 640 (1964).

[3.5] For example, neutron scattering: Y. Fujii, H. Nakao, T. Yosihama, M. Nishi, K. Nakajima, K. Kakurai, M. Isobe, Y. Ueda, and H. Sawa, J. Phys. Soc. Jpn. **66,** 326 (1997); Yoshihama, M. Nishi, K. Kakajima, K. Kakurai, Y. Fujii, M. Isobe, C. Kagami, and Y. Ueda, J. Phys. Soc. Jpn. **67,** 744 (1998). NMR: T. Ohama, M. Isobe, H. Yasuoka, and Y. Ueda, J. Phys. Soc. Jpn. **66**, 545 (1997); Ref. [3.27]. Raman scattering: M. Weiden, R. Hauptmann, C. Geibel, F. Steglich, M. Fischer, P. Lemmens, and G. Güntherodt, Z. Phys. B **103,** 1 (1997).

[3.6] H. Smolinski, C. Gros, W. Weber, U. Peuchert, G. Roth, M. Weiden, and C. Geibel, Phys. Rev. Lett. **80**, 5164 (1998).

[3.7] H. G. von Schnering, Yu. Grin, M. Kaupp, M. Somer, R. K. Kremer, O. Jepsen, T. Chatterji, and M. Weiden, Z. Kristallogr. 213, 246 (1998).

[3.8] A. Meetsma, J. L. de Boer, A. Damascelli, T. T. M. Palstra, J. Jegoudez, and A. Revcolevshi, Acta Crystallogr. Sec. C **54,** 1558 (1998).

[3.9] D. Khomskii, W. Geertsma and M. Mostovoy, Czech. J. Phys., **46,** Suppl. S6-3239 (1996).

[3.10] T. Ohama, H. Yasuoka, M. Isobe, and Y. Ueda, Phys. Rev. B **59**, 3299 (1999).

[3.11] P. Horsch and F. Mack, Eur. Phys. J. B **5**, 367-370 (1998).

[3.12] M. V. Mostovoy and D. I. Khomskii, cond-mat/9806215.

[3.13] H. Seo and H. Fukuyama, J. Phys. Soc. Jpn. **67**, 2602 (1998).

[3.14] J. Riera and D. Poilblanc, Phys. Rev. B **59**, 2667 (1999).

[3.15] H. Nakao, Doctor Thesis (Tokyo University, 1999).

[3.16] E. Lieb and F. Y. Wu, Phys. Rev. Lett., **20**, 1445 (1968).

[3.17] S. Sorella and A. Parola, J. Phys. Cond. Matter **4**, 3589 (1992).

[3.18] Z. Zou and P. W. Anderson, Phys. Rev. B **37**, 627 (1988).

[3.19] C. Kim, A. Y. Matsuura, Z.-X. Shen, N. Motoyama, H. Eisaki, S. Uchida, T. Tohyama, and S. Maekawa, Phys. Rev. Lett. **77**, 4054 (1996); Phys. Rev. B **56**, 15589 (1998).

[3.20] J. Zaanen, G. A. Sawatzky and J. W. Allen, Phys. Rev. Lett. **55**, 418 (1985).

[3.21] M. Isobe and Y. Ueda, J. Alloys and Compounds, **262-263**, 180 (1997).

[3.22] H. Tsunetsugu, J. Phys. Soc. Jpn. **60**, 1460 (1991).

[3.23] M.Isobe, C. Kagami and Y.Ueda, J. Crystal Growth, **181**, 314 (1997).

[3.24] J.-J. Yeh and I. Lindau, At. Data Nucl. Data Tables **32**, 1 (1985).

[3.25] Z. S. Popović and F. R. Vukajlović, Phys. Rev. B **59**, 5333 (1999).

[3.26] N. Katoh, T. Miyazaki, and T. Ohno, Phys. Rev. B **59**, 12723 (1999).

[3.27] T. Ohama, H. Yasuoka, M. Isobe, and Y. Ueda, J. Phys. Soc. Jpn. **66**, 3008 (1997).

[3.28] S. Hüfner, *Photoelectron Spectroscopy* (Springer-Verlag, Berlin, 1994).

[3.29] J. J. Sakurai, *Modern Quantum Mechanics* (The Benjamin/Cummings Publishing Company, California, 1985).

[3.30] P. A. Cox, *The Electronic Structure and Chemistry of Solids* (Oxford University Press, New York, 1987).

[3.31] I. H. Inoue, I. Hase, Y. Aiura, A. Fujimori, Y. Haruyama, T. Maruyama, and Y. Nishihara, Phys. Rev. Lett. **74**, 2539 (1995).

[3.32] K. Morikawa, T. Mizokawa, K. Kobayashi, A. Fujimori, H. Eisaki, S. Uchida, F. Iga, and Y. Nishihara, Phys. Rev. B **52**, 13711 (1995).

[3.33] M. Ogata and H. Shiba, Phys. Rev. B **41**, 2326 (1990).

[3.34] D. Augier, D. Poilblanc, S. Haas, A. Delia, and E. Dagotto, Phys. Rev. B **56**, 5732 (1997).

[3.35] T. Tohyama and S. Maekawa, unpublished.

[3.36] K. Penc, K. Hallberg, F. Mila, and H. Shiba , Phys. Rev. Lett. **77**, 1390 (1996)

[3.37] J. Favand, S. Haas, K.Penc, F. Mila, and E. Dagotto Phys. Rev. B **55**, 4859 (1997).

[3.38] T. Tohyama, H. Okuda, and S. Maekawa, Physica C **215**, 382 (1993).

[3.39] H. Suzuura and N. Nagaosa, Phys. Rev. B **56**, 3548 (1997).

[3.40] K. Penc and M. Serhan, Phys. Rev. B **56**, 6555 (1997).

[3.41] S. Shin, S. Suga, M. Taniguchi, M. Fujisawa, H. Kanzaki, A. Fujimori, H. Daimon Y. Ueda, K. Kosuge, and S. Kachi, Phys. Rev. B **41**, 4993 (1990); A. E. Bocquet, T. Mizokawa, K. Morikawa, A. Fujimori, S. R. Barman, K. Maiti, D. D. Sarma, Y. Tokura and M. Onoda, Phys. Rev. B **53**, 1161 (1996).

[3.42] A. N. Vasil'ev, V. V. Pryadun, D. I. Khomskii, G. Dhalenne, A. Revcolevschi, M. Isobe, and Y. Ueda, Phys. Rev. Lett. **81**, 1949 (1998).

[3.43] K. Maiti, Priya Mahadevan, and D. D. Sarma, Phys. Rev. Lett. **80**, 2885 (1998).

Chapter 4

Successive Phase Transitions in Bipolaron System Ti_4O_7

We have performed a photoemission study of Ti_4O_7 around its transition temperatures so as to cover the metallic ($T > 154$ K), high-temperature insulating (154 K $> T \gtrsim 140$ K), and low-temperature insulating (140 K $\gtrsim T$) phases. While the O $2p$ band is almost unchanged with temperature, the spectra of the Ti $3d$ band exhibit three characteristic spectral lineshapes corresponding to the three phases. Particularly, the spectra of the high-temperature semiconducting phase are gapless at the Fermi level, which is interpreted as a soft Coulomb gap due to dynamical disorder. In addition, we performed a quantitative comparison with Fe_3O_4, which exhibits a charge order-disorder transition (Verwey transition) as in the case of Ti_4O_7, and found that the spectra of Fe_3O_4 in the high temperature phase are also well interpreted by assuming a Coulomb gap. These observations indicate that dynamical disorder possibly makes a significant influence on the physical properties of both Fe_3O_4 in the high temperature phase and Ti_4O_7 in the high-temperature insulating phase.

4.1 Introduction

The titanium oxide Ti_4O_7 is a member of Magnéli phases, which form a homologous series of triclinic compounds of the form T_nO_{2n-1} (T = Ti or V, $4 \leq n \leq 10$) [4.1]. In 1970's to early 1980's, this compound was intensively studied as a typical system where a pair of two polarons in real space, i. e. bipolaron, exits [4.2–5]. Ti_4O_7 is a system with nominal $3d^{0.5}$ electron per Ti, allowing two possible valence states, Ti^{3+} ($3d^1$) and Ti^{4+} ($3d^0$). The electrical resistivity ρ and the magnetic susceptibility χ show peculiar temperature dependences as shown in Fig. 4.1 (a) [4.6–8]. It shows metallic conductivity at high temperature (metallic phase: M). With decreasing temperature, it undergoes a metal-to-semiconductor transition at $T_{MS} = 154$ K with a

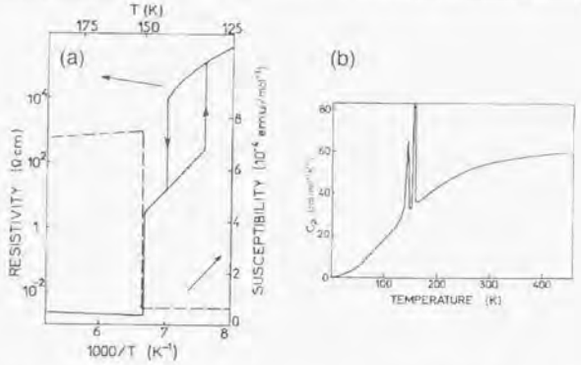

Figure 4.1: (a) Electrical resistivity and magnetic susceptibility of Ti_4O_7 plotted against reciprocal temperature [4.6]. (b) Heat capacity of Ti_4O_7 as a function of temperature [4.3, 6].

steep increase in ρ by three orders of magnitude although ρ, which seems to be of activation type, is relatively small $\sim$ 10 Ωcm compared to ordinary semiconductors (high-temperature insulating phase: HI). Subsequently, a semiconductor-to-semiconductor phase transition occurs at $T_{SS} \sim 140$ K[1] with a further rise in ρ by three orders of magnitude (low-temperature insulating phase: LI). The transition at $T = T_{SS}$ exhibits a thermal hysteresis of $\sim$ 5 K. On the other hand, χ, which is attributed to Pauli paramagnetism in the M phase, drops at $T = T_{MS}$, implying the formation of non-magnetic singlet pairs. The residual χ below $T = T_{MS}$, which is small and temperature-independent, is attributed to Van Vleck paramagnetism related to the matrix elements between the singlet and triplet states of the pairs [4.5]. As shown in Fig. 4.1 (b), the temperature dependence of the specific heat has two peaks centered at $T = T_{MS}$ and T_{SS}, whose shapes are characteristic of first-order transitions [4.3, 6].

The crystal structure of Ti_4O_7 is based on the rutile TiO_2 structure as shown in Fig. 4.2. In rutile TiO_2, where TiO_6 octahedra are running along the rutile c-axis with their edge shared, the chains contact each other at the corners of the TiO_6 octahedra. As shown in Fig. 4.3, Ti_4O_7 consists of rutile-like blocks composed of chains of four TiO_6 octahedra lining infinitely in parallel. The rutile-like blocks are separated by crystallographic shear planes along which the TiO_6 octahedra share faces while they share edges inside the blocks. The crystal symmetry is triclinic with four formulas per unit cell (space group $P\bar{1}$ at both 298 K and 115K with the lattice parameters of $a = 5.597$ Å, $b = 7.125$ Å, $c = 20.429$ Å, $\alpha = 67.70°$, $\beta = 57.16°$, and $\gamma = 108.76°$ at 298 K) [4.10]. It has four different crystallographic Ti sites labelled as 1, 2, 3, and 4 in Fig. 4.3. Hence, they form two types of octahedral chains along the pseudo-rutile c-axis, such as Ti(3)-Ti(1)-Ti(1)-Ti(3) and Ti(4)-Ti(2)-Ti(2)-Ti(4), which will be referred to as the 3113 chain and the 4224 chain, respectively, below. The Ti-Ti distances and the Ti valences estimated from the average Ti-O interatomic distance in each TiO_6 octahedron using the bond strength/bond length method are listed in Table. 4.1 [4.6]. The schematic crystal structures of the LI, HI, and M phases are shown in Figs. 4.4 (a), (b), and (c), respectively. In the M phase, the four crystallographically different Ti sites are similar with an uniform valence of 3.5 as determined above. In the LI phase, the charges are localized on the

[1] T_{SS} shows a deviation of $\sim$ 5 K depending on samples [4.7].

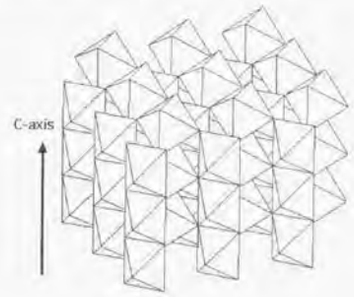

Figure 4.2: Rutile structure of TiO_2, where TiO_6 octahedra are running along the c-axis with their edge shared, forming an infinite one-dimensional chain. The chains contact each other at the corners of the octahedra.

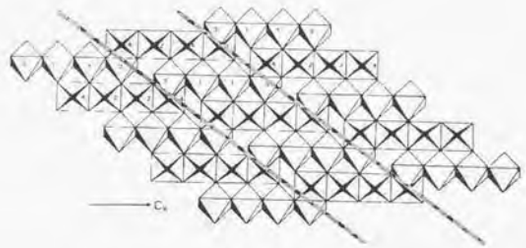

Figure 4.3: Stacking of the TiO_6 octahedra in Ti_4O_7. Successive sections of three rutile-like blocks are separated by the two thick lines indicating the crystallographic shear planes. The arrow indicates the pseudo-rutile c-axis. The numbers 1, 2, 3, and 4 refer to the crystallographically different Ti sites.

		298 K	140 K	120 K
Ti-Ti distance (Å)	1–3	3.02	2.99	2.80
	1–1	2.90	2.93	3.13
	2–4	3.02	3.00	3.08
	2–2	2.94	2.94	3.02
Ti valence	Ti (1)	3.48	3.43	3.02
	Ti (2)	3.45	3.55	4.00
	Ti (3)	3.60	3.48	3.09
	Ti (4)	3.47	3.54	3.90

Table 4.1: Top: Distances between crystallographically different Ti sites (in Å) at 298 K (M phase), 140 K (HI phase), and 120 K (LI phase) [see Fig. 4.3]. Bottom: Ti valences estimated from the average Ti-O interatomic distance in each TiO_6 octahedron [4.6].

3113 chains occupied by Ti^{3+} with the empty 4224 chains occupied by Ti^{4+} sites. The chains in the HI phase are likely to be in a dynamically disordered state according to the electron paramagnetic resonance (EPR) study [4.4, 9] although a fivefold superstructure for the HI phase was once reported [4.10]. The phase diagram of $(Ti_{1-x}V_x)_4O_7$ as described below also supports the existence of the disordered state in the HI phase at $x \to 0$ [see Fig. 4.5 (c)].

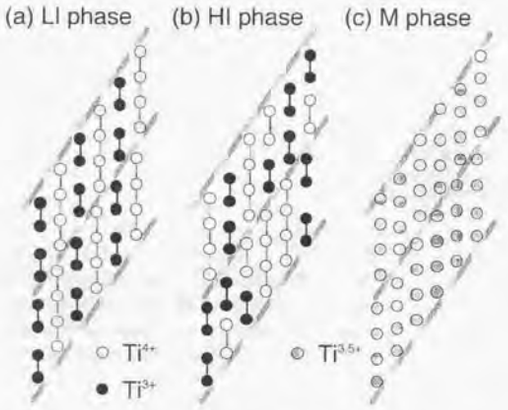

Figure 4.4: Schematic crystal structure of Ti_4O_7, where only the chains parallel to the pseudo-rutile c-axis truncated by shear planes are shown [4.2]. The thick lines indicate the shear planes. (a) Crystal structure of Ti_4O_7 in the LI phase, where the chains are ordered. (b) Disordered model for the HI phase [4.2, 4, 10]. (c) Crystal structure of Ti_4O_7 in the M phase where all the Ti sites have a uniform valence of 3.5.

Based on these observations, the physical properties of Ti_4O_7 have been explained as follows. In the LI phase, a d electron is localized in each Ti^{3+}-Ti^{3+} pair inside the 3113 chain, which accounts for the semiconducting behavior and the low temperature-independent magnetic susceptibility. In the M phase, the delocalization of the d electrons gives rise to a metallic behavior. For the HI phase, the existence of disordered Ti^{3+}-Ti^{3+} pairs with no long-range order results in the low semiconducting resistivity and the diamagnetic susceptibility [4.2]. From this viewpoint, the transition at $T = T_{SS}$ is interpreted as an order-disorder transition of the Ti^{3+}-Ti^{3+} pairs, namely, bipolarons. The LI and HI phases correspond to a solid and a liquid of bipolarons, respectively. Above $T = T_{MS}$, the bipolaron is dissociated into two polarons, yielding metallic conductivity and Pauli paramagnetism.

The order-disorder transition of bipolarons discussed above has been referred to as a Verwey transition [4.6, 11]. The Verwey transition [4.12] was originally pointed out for Fe_3O_4 at $T_V \simeq 120$ K. Fe_3O_4 has two possible valence states of Fe^{2+} and Fe^{3+}, analogous to Ti_4O_7. The charge-ordered states in Fe_3O_4 and Ti_4O_7 are, however, different in that the cations in the former have magnetic moments resulting in the ferrimagnetic long-range order while in the latter the diamagnetic cation pairs are formed. It is noted that the conductivities in Ti_4O_7 above $T = T_{MS}$ and Fe_3O_4 above $T = T_V$ are $\sim 10^3$ and $\sim 10^2\ \Omega^{-1}\mathrm{cm}^{-1}$, respectively, both of which are small compared to an ordinary metal.

Since the HI phase in Ti_4O_7, which is of particular interest as a disordered system, is stable only within the small temperature interval, the physical properties of $(Ti_{1-x}V_x)_4O_7$ have been studied instead, where the stable temperature range of the intermediate disordered phase is much wider than in pure Ti_4O_7. Figures 4.5 (a)–(d) show the physical properties of $(Ti_{1-x}V_x)_4O_7$ [4.5]. The electrical resistivity for the V-substituted compounds with various x (%) is plotted against the reciprocal temperature in Fig. 4.5 (a). The steep metal-to-semiconductor transition remains for all the compounds while the semiconductor-to-semiconductor transition is smeared out with increasing x and vanishes between $x = 0.33$ and 0.38 %. The magnetic susceptibility shown in Fig. 4.5 (b) also indicates that the metal-to-semiconductor transition still exists in all the V-substituted samples as in pure Ti_4O_7, signaling the formation of the Ti^{3+}-Ti^{3+} pairs below $T = T_{MS}$. In this phase, the susceptibility is not diamagnetic but of Curie-type with the Curie temperature of < 4 K and the effective magnetic moment of $2 \pm 0.1 \mu_B$ per vanadium, which can be explained by the existence of Ti^{3+}-V^{3+} pairs on which an excess electron is trapped in addition to a pair of two electrons [4.5]. The phase diagram of $(Ti_{1-x}V_x)_4O_7$ in Fig. 4.5 (c) was obtained from the electrical resistivity, magnetic susceptibility, EPR and calorimetric measurements. The conductivity in the intermediate (HI) phase (the semiconducting disordered phase) just below $T = T_{MS}$ can be fitted to an

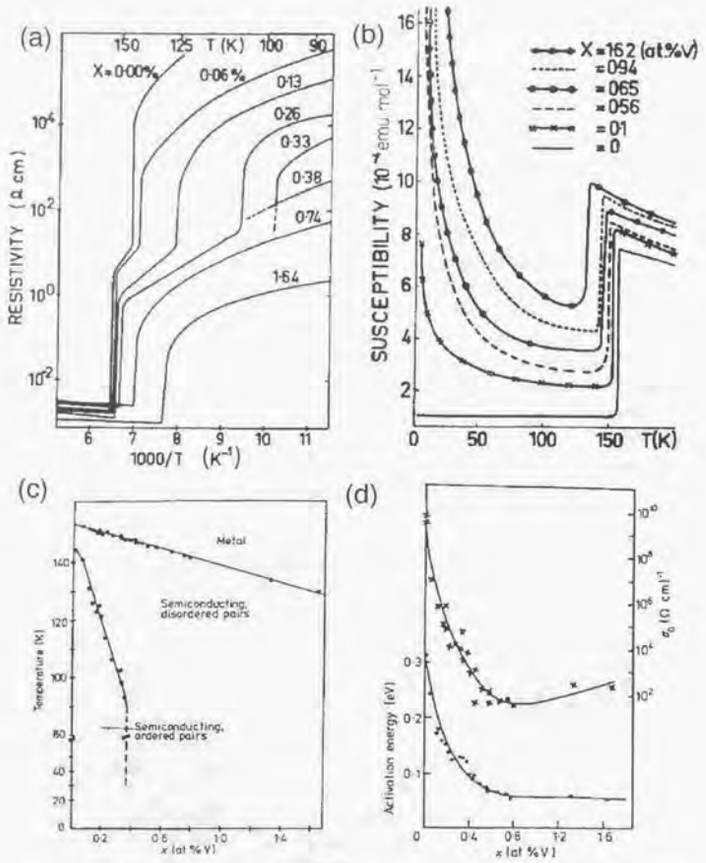

Figure 4.5: Physical properties of $(Ti_{1-x}V_x)_4O_7$ [4.5]. (a) Electrical resistivity plotted against reciprocal temperature showing the vanishing of the LI phase above x (%)$\simeq$ 0.38. (b) Magnetic susceptibility plotted against temperature for x (%)= 0, 0.1, 0.56, 0.65, 0.94, and 1.62. (c) Phase diagram. (d) Activation energy E_a (left-hand scale, lower curve) and pre-exponential factor σ_0 (right-hand scale, upper curve) in the intermediate (HI) phase (the semiconducting disordered phase) just below $T = T_{MS}$.

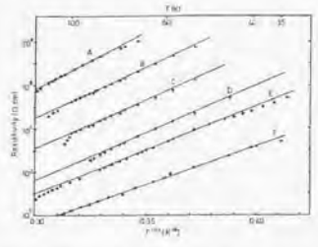

Figure 4.6: Electrical resistivity of $(Ti_{1-x}V_x)_4O_7$ in the semiconducting phase at low temperatures plotted against $T^{-1/4}$ for x(%)= 0, 0.1, 0.56, 0.65, 0.94, and 1.62 labelled as A, B, C, D, E, and F, respectively [4.5].

activation-type conductivity $\sigma = \sigma_0 \exp(-E_a/k_BT)$, whose activation energy E_a and coefficient σ_0 are plotted as a function of x in Fig. 4.5 (d). Additionally, it is worth mentioning that the resistivity of the semiconducting phase at lower temperatures is not of the activation-type but is well fitted to the variable-range-hopping (VRH) form $\rho \propto \exp\left(-(T_0/T)^n\right)$ [4.5]. Figure 4.6 shows the electrical resistivity plotted against $T^{-1/4}$ as expected for VRH in a three-dimensional system.

As for the electronic structure, photoemission spectroscopy (PES) and x-ray absorption spectroscopy (XAS) studies of this system were reported by Abbate *et al.* [4.13, 14] as shown in Figs. 4.7 (a) and (b), respectively. With the energy resolution of 0.2 eV for PES and 0.25 eV for XAS, they could obtain different spectra for the M phase and LI phase. In this chapter, we report on the PES spectra of this compound obtained with a much higher energy resolution of $\sim$ 50 meV. Our aim of the present work is two-fold. One is to focus on the variation of the PES spectra and hence the electronic structure of Ti_4O_7 as a function of temperature. The other is the single-particle excitation spectra of disordered systems which should be observed in the HI phase. As for the latter subject, a comparative discussion with the PES result of Fe_3O_4 [4.15] will be performed.

4.2 Experiment

Single crystals of Ti_4O_7 were supplied by Dr. T. Tonogai and Prof. H. Takagi of ISSP, University of Tokyo. The crystals were grown by the vapor transport method [4.7, 8, 16, 17]. Ti_3O_5 powder was first prepared by heating a mixture of a prescribed amount of Ti and TiO_2 powder at 1100 °C for 24 hours in an evacuated, sealed quartz tube. A mixture of 2 g of the resultant Ti_3O_5 powder and 60 mg of $TeCl_4$, acting as a transport agent, were then sealed in

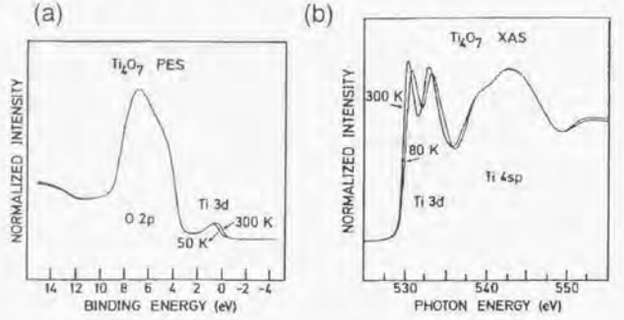

Figure 4.7: (a) Valence-band PES spectra of Ti_4O_7 at $T = 50$ K (the LI phase) and 300 K (the M phase) measured at $h\nu = 45$ eV, where the contribution from Ti $3d$ electrons is resonantly enhanced. The result shows that the Ti $3d$ band is shifted by ~ 0.25 eV towards higher binding energies in the LI-phase spectrum. (b) O $1s$ XAS spectra at at $T = 80$ K (the LI phase) and 300 K. Two peaks around $h\nu \sim 530$–535 eV are attributed to the t_{2g} and e_g subbands, which show a crystal field splitting of ~ 2.4 eV [4.13]. These peaks are shifted by ~ 0.6–0.7 eV towards higher energies in the LI phase.

an evacuated quartz tube with a diameter of 10 mm and a length of about 200 mm. The tube was kept for 7 days in a gradient furnace of a source temperature of 1150 °C. The obtained single crystals had $T_{MS} = 154$ K and $T_{SS} \sim 140$ K.

Ultraviolet photoemission spectroscopy (UPS) measurements were performed using an OMICRON hemi-spherical analyzer and the He I resonance line ($h\nu$ =21.2 eV) from a Vacuum Generator discharge lamp as a light source. Calibration and estimation of the instrumental resolution were done using Au evaporated on the sample surfaces by measuring the Fermi edge. The energy resolution was set ~50 meV in the present experiments in order to collect a number of spectra after a single cleave. Samples with a typical size of $4 \times 1 \times 0.5$ mm^3 were cleaved *in situ*. Every cleavage gave a rough surface, an assembly of randomly-orientated small facets. Since the analyzer has an acceptance angle of ±8°, the obtained spectra were supposed to be angle-integrated photoemission (AIPES) spectra. Indeed, the spectra were almost independent of the angle of the orientation of the cleaved surfaces. We checked that the measurements on the sample surfaces scraped *in situ* with a diamond file yielded almost the same results as those obtained for the cleaved surfaces. The measurement temperature ranged from $T = 120$ K to 170 K, covering the three phases of Ti_4O_7. The temperature was controlled within the accuracy of ±0.2 K using a digital temperature controller made by Scientific Instruments, Inc. While the calibrated silicon-diode thermometer was used, there existed a difference of ~ 2 K between the temperature of the

thermometer and that at the sample surfaces[2]. We calibrated the thermometer taking this into account. For the measurements in the III phase, we took special care in changing the temperature to avoid its overshooting to within 0.5 K. The base pressure in the spectrometer was less than 1×10^{-10} Torr. Below, we show reproducible results for several sample surfaces which were obtained within a few hours after cleavage.

4.3 Results and Discussion

4.3.1 Electronic Structure in the Entire Valence-Band Region

Figure 4.8 shows PES spectra of the entire valence band of Ti_4O_7 measured using $h\nu = 21.2$ eV photons at various temperatures covering the M, III, and LI phases. The spectra have been normalized to the area between binding energies (E_B) of 0 and 10 eV. The prominent features at $E_B = 3$–9 eV are the O $2p$ band while the weaker structures between 0 and 2 eV are the Ti $3d$ band. Judging from the lineshape of the spectra of the Ti $3d$ band in the expanded scale, T_{SS} was found to lie between 132 and 136 K for this cleavage. There are two distinct structures in the O $2p$ band at $E_B \sim 5$ and ~ 7 eV. In the previous result shown in Fig. 4.7 (a) [4.13], the 5 eV structure is weakly visible as a shoulder, while the 7 eV one appears as the dominant feature. The difference of the intensities between the previous [4.13] and present results reflects the strength of hybridization between the O $2p$ and Ti $3d$ electrons. Since the spectra taken at $h\nu = 45$ eV met the resonance condition of Ti $3p \rightarrow 3d$ transition, the resonantly enhanced structure around $E_B \sim 7$ eV is of O $2p$-Ti $3d$ bonding character. The 5 eV structure is hence attributed to states of O $2p$ non-bonding character. As shown in Fig. 4.8, there appears almost no temperature dependence in the positions and widths of the O $2p$ band even across the two phase transitions, indicating that the crystallographic distortion with the phase transitions makes no, or little if any, influence on the O $2p$ band, consistent with the previous result [4.13].

4.3.2 Electronic Structure in the Ti $3d$-Band Region across the Phase Transitions

Figure 4.9 shows the PES spectra in the Ti $3d$ band region. As indicated by the arrows in Fig. 4.9, the sample was first cooled and then heated so as to cross twice each of the two phase-transition temperatures of Ti_4O_7. The first spectrum in the bottom of Fig. 4.9, which was measured at 157 K ($> T_{MS}$)

[2]The metal-to-semiconductor transition thus occurred at the same measured temperature of $T_{MS} = 154$ K throughout the experiments.

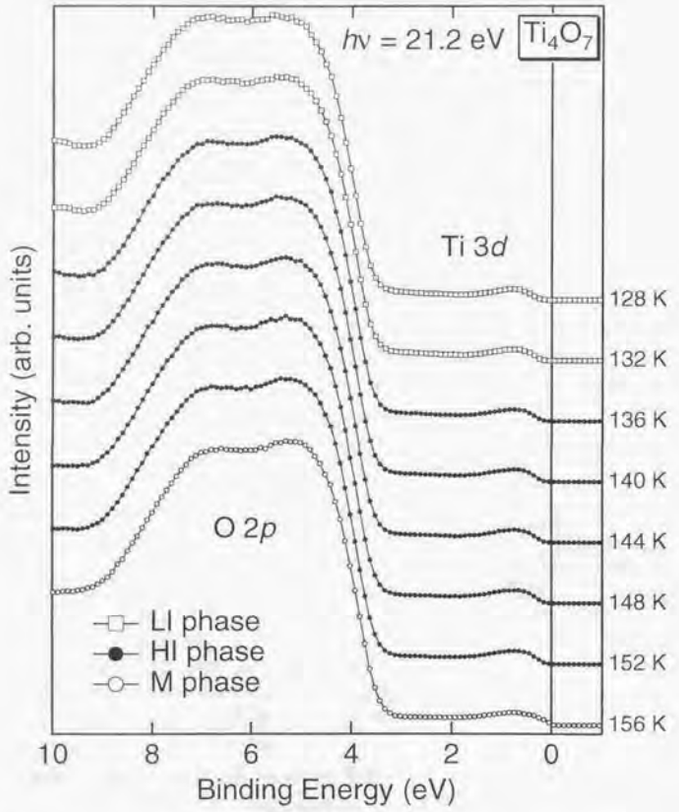

Figure 4.8: PES Spectra of Ti_4O_7 measured using He I ($h\nu$ = 21.2 eV) at various temperatures covering the M, HI, and LI phases, which are plotted by dotted-dashed, solid, and dashed lines, respectively. T_{SS} was situated between 132 K and 136 K for this cleavage.

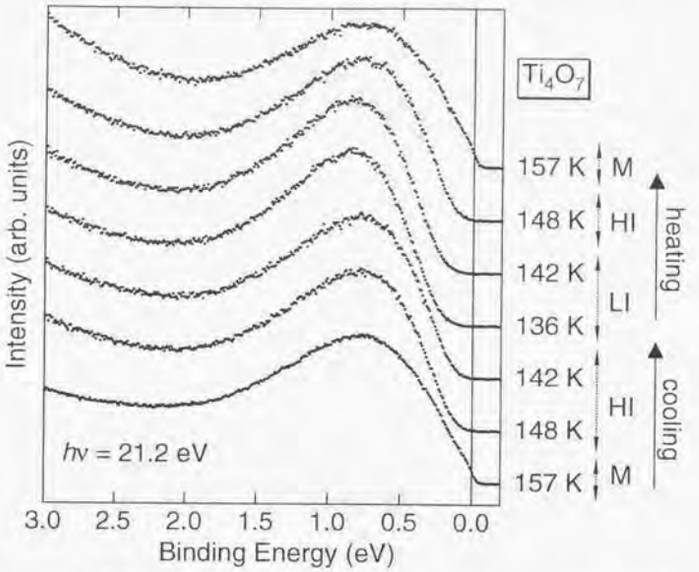

Figure 4.9: PES spectra of Ti_4O_7 measured by He I ($h\nu$ = 21.2 eV) in changing the temperature as 157 K → 148 K → 142 K → 136 K → 142 K → 148 K → 157 K from the bottom to the top of the figure. The attributed phases are labeled in the right of the figure.

shows a broad maximum around E_B = 0.75 eV with a weak but finite Fermi edge, reflecting its metallic nature. On cooling from T = 157 K to 148 K, the spectrum loses the Fermi edge, indicating that the HI phase is no longer metallic. Whereas the 142 K spectrum in the cooling was identical to the 148 K one, the spectrum changed in going to 136 K and showed the sharpest peak at $E_B \sim 0.85$ eV. Since these changes occur with the energy scale much larger than the instrumental energy resolution ~50 meV, we concluded that the 157 K and 136 K spectra reflect the intrinsic electronic structure of the M and LI phases of Ti_4O_7, respectively, between which the HI phase was situated. T_{SS} for the cooling existed between 136 and 142 K. These three spectra were also shown in the top panel of Fig. 4.10. The difference spectrum between the M and LI phase (the M-LI difference spectrum) and that between the HI and LI phase (the HI-LI difference spectrum) are shown in the bottom panel of Fig. 4.10.

Next, we heated the sample from 136 K to 157 K as shown in the top

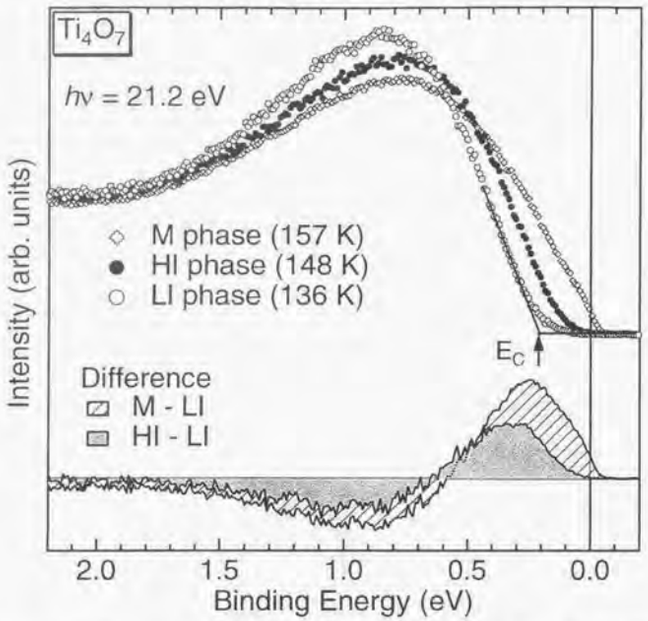

Figure 4.10: Top panel: PES spectra corresponding to the three phases of Ti_4O_7. They have been normalized to their area between $E_B = -0.2$ eV and 2.0 eV. The arrow for the LI spectrum indicates a gap (E_C). Bottom panel: The M-LI and HI-LI difference spectra.

half of Fig. 4.9. Interestingly, the 142 K spectrum was found to be identical to the 136 K spectrum, not to the 142 K spectrum in the cooling as more clearly seen in Fig. 4.11. That is, T_{SS} for the heating was located between 142 and 148 K for this sample, compared to between 136 and 142 K in the cooling. This difference in T_{SS} between heating and cooling is due to thermal hysteresis between the LI and HI phases, as has been observed in the electrical resistivity (see Fig. 4.1), thermopower [4.9], optical transmission [4.18], and EPR measurements [4.4, 9]. To extract the hysteretic behavior, we have defined the integrated PES intensity $S(T)$ as a function of temperature as

$$S(T) = \int_{E_F}^{E_1} I(E_B, T) dE_B / \int_{E_1}^{E_2} I(E_B, T) dE_B, \qquad (4.1)$$

where $I(E, T)$ is the PES intensity. $S(T)$ obtained for $E_1 = 0.5$ eV and $E_2 =$

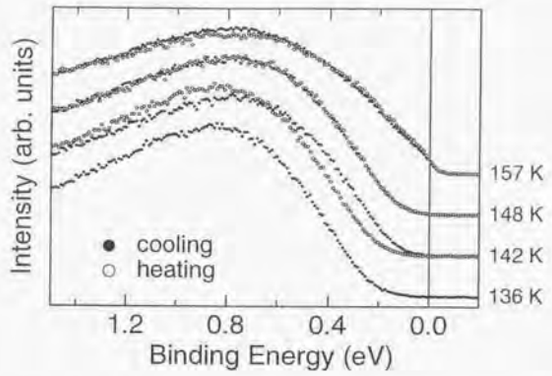

Figure 4.11: Spectra of Ti_4O_7. Two 142 K spectra are different between in the cooling and in the heating due to the hysteresis effect.

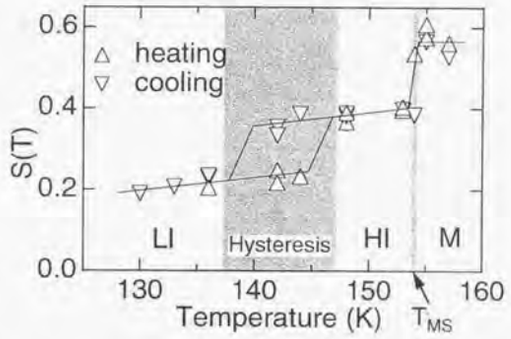

Figure 4.12: Integrated PES intensity $S(T)$ defined by Eq. (4.1) calculated for $E_1 = 0.5$ eV and $E_2 = 1$ eV. The upward- and downward-triangles denote values in the heating and cooling processes, respectively. The solid line is guide to the eye.

1 eV is plotted in Fig. 4.12[3], indicating that this behavior was reproducible for several thermal cyclings crossing T_{MS} and T_{SS}. Since the speed of cooling and heating was kept almost constant during this iteration, the width of the

[3]A slight change of E_1 and E_2 does not seriously affect the qualitative trend shown in Fig. 4.12.

hysteresis was 6–12 K in the present case, while, actually, the width was found to depend both on samples and on thermal cycling around the SS transition, being consistent with the previous reports. The reason for this uncertainty in the hysteresis width was attributed to the nucleation of domains of the LI phase coexisting with the rest of the crystal which is still in the HI phases [4.4, 9, 18]. This could be explained in terms of the spinodal decomposition. At this moment, there is no information about the size of such domains, on which diffuse scattering experiments using x-ray or neutron would shed some light. Nevertheless, the discrete and reproducible behavior of the spectral change shown in Fig. 4.12 strongly supports that the intermediate phase consists of almost single HI phase with negligible amount of the LI phase. While the PES spectra of 1T-TaS_2 show hysteretic behavior with width of $\sim$ 100 K [4.19], the present result is interesting in that hysteresis in such a narrow temperature range is observed by PES measurements.

PES Spectra of the M Phase

Let us discuss the M-, HI-, and LI-phase spectra in detail below. First, we focus on the M-phase spectra. The Ti $3d$ orbital occupied by electrons is thought to be approximately the $3d_{x^2-y^2}$ orbital [4.4], where x is the direction of the pseudo-rutile c-axis. In the M phase, the transfer integral t between the neighboring $d_{x^2-y^2}$ orbitals is estimated $\sim$ 0.40–0.47 eV [4.20] for the Ti-Ti distance of 2.9–3.0 Å (Table. 4.1). Then, as a first approximation, Ti_4O_7 has a single band of the width $W \sim 4t$, quarter of which is occupied and should be observed as occupied states in PES. Apparently, most of the spectral weight of the occupied states exists at higher binding energies around the broad maximum centered at E_B = 0.75 eV. A similar broad feature has been observed at $E_B \sim$ 1–1.5 eV in the spectra of three-dimensional vanadium and titanium oxides with $3d^1$ configuration such as $LaTiO_3$ and $YTiO_3$ [4.21–23]. The feature has been interpreted as the incoherent part of the spectral function accompanying the quasi-particle excitations around E_F[4]. The relative intensity of the incoherent part to that of the coherent part located around the Fermi level is known to be significantly dependent on the strength of electron correlation [4.21]. Indeed, this effect can be presented by the parameter U/W, where U and W are the magnitudes of the on-site Coulomb energy and the one-electron band width, respectively [4.21]. It is added here that we have also discussed the structure corresponding to the incoherent part in the spectra of the one-dimensional NaV_2O_5 in Sec. 3 although the momentum dispersions have been observed in this region for NaV_2O_5. No coherent spectral weight appears at E_F for NaV_2O_5 since it is an insulator.

What is characteristic in Ti_4O_7 is that the coherent part, which overlaps

[4]Details have been discussed in Chapter 2. See Fig. 2.2.

the tail of the incoherent peak, is so weak in intensity that it is hardly distinguishable from the incoherent part. This implies that the M phase of Ti_4O_7 is a strongly correlated metal, where the motion of the conduction electrons in this system is highly incoherent. Tonogai *et al.* [4.7, 8] observed a T^2 dependence in the resistivity in the low-temperature metallic phase of Ti_4O_7 under high pressure. Assuming the Kadowaki-Woods relation, they obtained the electronic specific heat coefficient γ = 70–80 mJ/K^{2}mol, which is quite enhanced comparable to γ = 80 mJ/K^{2}mol for V_2O_3 [4.24]. The enhanced Pauli susceptibility [4.3, 4] and the reduced Drude weight in the optical conductivity [4.7] of the M-phase Ti_4O_7 are also analogous to the metallic phase of V_2O_3 and support the strongly correlated picture.

PES Spectra of the LI Phase

Next, let us focus on the LI-phase spectra which correspond to single-particle excitations in the charge ordered state. In going from the M phase to the LI phase, the peak at E_B = 0.85 eV becomes sharper and a clear gap is open $E_C \sim$ 0.21 eV as shown in Fig. 4.10[5]. E_C is consistent with the previous PES study, which show a shift of the leading edge near E_F by $\sim$ 0.25 eV in going from the M phase to the LI phase [4.13] as shown in Fig. 4.7. The opening of the gap in the semiconducting phase of Ti_4O_7 has been attributed to the formation of bipolarons. The concept of bipolaron was firstly proposed by Anderson [4.25] for amorphous semiconductors, where two electrons form a singlet pair on a single site in order to compensate the Coulomb repulsion U by the energy gain due to lattice deformation. Later, this concept was applied to Ti_4O_7 [4.26]. It was pointed out that the nearest neighbor Coulomb repulsion V is weaker than the on-site Coulomb repulsion U and the total energy can be further lowered, leading to the formation of a singlet-pair between the nearest neighbor sites. The bipolaron binding energy E_b is thus given by

$$E_b = \frac{2g^2}{C} - V, \tag{4.2}$$

where g is the electron-phonon coupling parameter and C is the elastic constant. E_b was estimated to be $\sim$ 0.16 eV from the analysis of the EPR line width [4.26]. E_b is of the same order as E_C, which is the energy for a localized bipolaron to be decomposed into the photoelectron and the polaron with lattice distortion retained.

Simultaneously with the opening of the gap, considerable spectral weight transfer occurs over a much larger energy range than E_C as can be seen in the M-LI difference spectrum in Fig. 4.10. It is interesting to compare the

[5]Here, we only roughly estimated $E_C \sim$ 0.21 eV without paying any attention to the instrumental resolution. More quantitative treatment of the hard gap will be performed below (see Fig. 4.16 (a)).

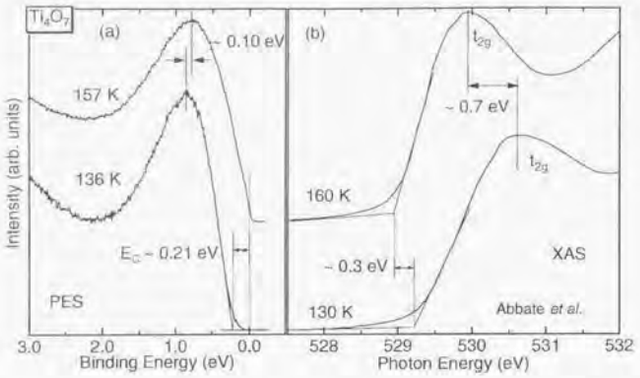

Figure 4.13: PES (a) and XAS [4.13] (b) spectra of Ti_4O_7 in the M and LI phases.

PES as well as XAS [4.13] spectra between the LI and M phases, as shown in Fig. 4.13. In the XAS spectra, the t_{2g} and e_g levels of Ti $3d$ were observed separately with the splitting of ~ 2.5 eV as shown in Fig. 4.7 (b). While this splitting was independent of temperature, the position of the unoccupied t_{2g} level was shifted to higher photon energies by ~ 0.7 eV in going from the M phase to the LI phase. If we estimate the optical gap E_{gap} by combining the threshold shifts of the XAS and PES spectra, $E_{gap} \sim 0.5$ eV is obtained as shown in Fig. 4.13, which is much larger than the measured optical gap of ~ 0.25 eV [4.18]. If the Fermi level may be pinned at the bottom of the conduction band as suggested by Abbate *et al.* [4.13], a band gap of ~ 0.2 eV would be obtained, in agreement with the value of the optical gap. The negative thermopower value, indicating that Ti_4O_7 is of n-type, supports their suggestion [4.9].

For further quantitative discussion on the lineshape of the LI-phase spectra, it is necessary to compare it with theoretical spectra calculated using the Fröhlich or Holstein model. In general, if the phonon energy is negligible in comparison with W or if the electron-phonon coupling constant is small, such interaction in metal does not cause significant influence on the PES spectra except for around E_F [4.27]. However, if these conditions do not hold, PES spectra are significantly influenced or a metal-to-insulator transition, in most cases a transition into a charge-density-wave (CDW) state, may occur and a gap is opened at E_F. At the same time, the PES spectra are greatly affected, where large spectral weight tends to transfer from the region around E_F to higher binding energies. Although the LI phase of Ti_4O_7 is not in the CDW state but in the ordered state of bipolarons, it would be

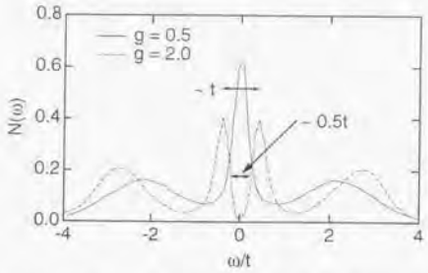

Figure 4.14: The electron density of states $N(\omega)$ of the Holstein model calculated at half-filling for the Einstein phonon $\omega_0 = 4.0t$ for an 8×8 lattice at temperature $0.1t$ [4.28], where t is the transfer matrix element between the nearest neighbor sites. g is the electron-phonon coupling constant.

worth comparing it with such theoretical calculations. For example, Vekić and White [4.28] calculated the single-particle excitation spectra based on the Holstein model using quantum Monte Carlo method. Figure 4.14 shows the calculated electron density of states $N(\omega)$, indicating that there emerges a CDW gap around $\omega = 0$ in going from the weak coupling case $g = 0.5$ to the strong coupling case $g = 2.0$. For $g = 2.0$ the CDW gap is of order $\sim 0.5t$ ($t \sim 0.5$ eV for Ti_4O_7) and the weight of the incoherent part shows a peak at $\omega \sim \pm 3t$. In spite of the unphysically large Einstein phonon frequency ω_0 in their calculation, the calculated lineshape [4.28] seems consistent with our observation for Ti_4O_7. Experimentally, however, there is no such a sharp feature corresponding to the coherent peak as shown in Fig. 4.14 [4.28] not only in the LI phase but also in the M phase. This discrepancy is probably due to Fröhlich interaction [4.29] or due to electron correlation including long-range Coulomb interaction [4.22]. If those interactions are taken into account, the self-energy $\Sigma(\vec{k}, \omega)$, where $\vec{k}$ is the electron momentum in the system, becomes strongly $\vec{k}$-dependent and the DOS near E_F is suppressed. Those competing effects, electron-electron and electron-phonon interactions, should be treated in a model including both [4.30], which has not yet been well understood.

PES Spectra of the HI Phase

The HI-phase spectra take an intermediate lineshape between the LI and M spectra: They show no Fermi edge and have a somewhat broader peak at $E_B = 0.75$ eV than that of the LI-phase spectra. If we estimate the gap of the HI phase as in the LI spectra (Fig. 4.10), 0.12 eV is obtained. The situation is, however, more delicate since there appears no real gap in the HI phase as substantiated in the HI-LI difference spectra in the bottom

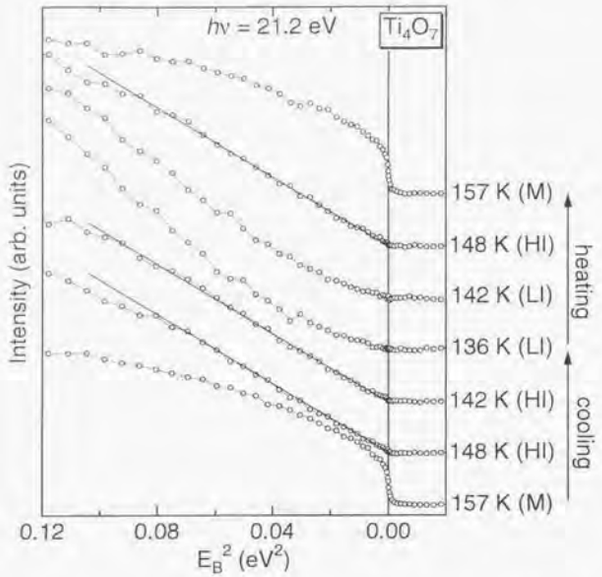

Figure 4.15: PES spectra of Ti_4O_7 plotted against E_B^2 for $E_B > 0$ and $-E_B^2$ for $E_B < 0$. The straight lines are guide to the eye.

of Fig. 4.10. Indeed, the spectral intensity vanishes only at $E_B = 0.0$ eV. Figure 4.15 shows the spectra plotted against E_B^2 for $E_B > 0$ and $-E_B^2$ for $E_B < 0$. As shown in Fig. 4.15, the M-phase spectra are convex near E_F with an enhanced Fermi edge, while the LI spectra, which have a "hard gap", are concave. In contrast, the HI-phase spectra form an almost straight line from $E_B^2 = 0.00$ to ~ 0.08 eV^2 ($0.0 \leq E_B \lesssim 0.3$ eV) as indicated in Fig. 4.15. This clearly means that the spectra are tangent to E_F with the power law exponent of ~ 2. For more quantitative analysis taking the experimental resolution into account, we have performed a lineshape analysis for the LI- and HI-phase spectra. The following lineshape $I(E = E_B, T)$ was assumed with free parameters a_2, b_0, and E_0:

$$I(E,T) = I_0(E,T) + I_{bg}(E), \tag{4.3}$$

where $I_0(E,T)$ is the intrinsic part expressed as:

$$I_0(E,T) = \begin{cases} a_2(E-E_0)^2 F_{FD}(E,T), & \text{for } E \geq E_0 \\ 0, & \text{for } E < E_0, \end{cases} \tag{4.4}$$

where $F_{FD}(E,T)$ is the Fermi-Dirac function at T although the effect of $F_{FD}(E,T)$ is negligibly weak because $I_0(E_F,T) = 0$ and $T \sim 150$ K. $I_{bg}(E)$ represents the constant background of the PES spectra given by

$$I_{bg}(E) = b_0. \tag{4.5}$$

E_0 was fixed 0 for the HI phase while it was allowed to take a finite value for the LI phase. Instrumental resolution was included through the convolution of $I(E,T)$ with the Gaussian of FWHM 50 meV. As shown in Fig. 4.16 (a), the result of the fitting is satisfactory, especially for the HI spectra, between $-0.2 \leq E_B \leq 0.3$ eV. We also show part of the results in Fig. 4.16 (b) on the log-log scale to emphasize the $(E - E_F)^2$ dependence of the HI phase, which makes a clear contrast to the LI phase in Fig. 4.16 (c). The resolution of 50 meV is influential only for $E_B \lesssim 0.05$ eV. Thus, $I \propto E^2$ is quite convincing around the Fermi level of the HI-phase spectra.

We propose that the above phenomenon peculiar to the HI-phase spectra can be explained as a consequence of the dynamical disorder inherent in this phase, whose existence has been established through EPR results [4.4]. Theoretical studies of disordered systems have a long history since 1958 when Anderson raised a concept of electron localization due to disorder [4.31]. Here, we briefly summerize the single-particle excitation spectra predicted for these systems: According to Altshuler and Aronov [4.32], the effect of disorder in a metal appears as a cusp $\propto |E - E_F|^{\frac{1}{2}}$ in the DOS $N(E)$ in the vicinity of E_F. Experimentally, an indication of this cusp-like depletion of $N(E)$ has been reported for $Ge_{1-x}Au_x$ [4.33], granular Al wire [4.34], and $LaNi_{1-x}T_xO_3$ (T = Mn, Fe, and Ni) [4.35] by tunneling and photoemission spectroscopy. On the other hand, Efros and Shklovskii (ES) [4.36, 37] have predicted that $N(E)$ of a disorder-driven insulator shows a "soft gap" called Coulomb gap at E_F:

$$N(E) = \frac{3}{\pi}\left(\frac{\kappa}{e^2}\right)^3 (E - E_F)^2, \tag{4.6}$$

where κ is the dielectric constant. The essence of their argument is quite simple as follows [4.36]: Consider a three-dimensional disordered system composed of localized electronic states close to E_F where electron-electron interaction $U_{ij} = e^2/4\pi\kappa r_{ij}$ exists between any two states i and j. Here, $r_{ij} = |r_i - r_j|$ is the distance between the two localized states. If we denote the energies of single-particle excitations of the occupied state i and the vacant state j by E_i and E_j, respectively, the following inequality should hold for the transfer of an electron from state i to state j.

$$E_j - E_i - U_{ij} > 0. \tag{4.7}$$

in order for the system to be stable. Here, last term represents the exitonic effect of the created electron-hole pair between the states i and j. Now, let

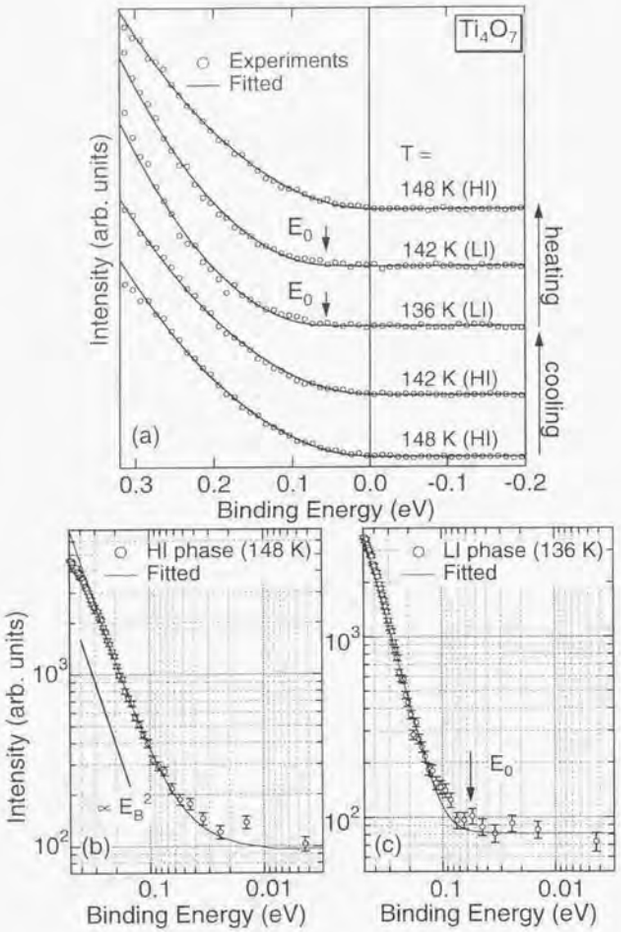

Figure 4.16: (a) Result of the fitting of the LI- and HI-phase spectra to Eq. (4.4). The arrows indicate E_0 for the LI phase. As mentioned in the text, the fitting has been performed with the instrumental resolution of 50 meV included. (b) The HI-phase spectrum and the fitted curve plotted on the log-log scale. (c) The LI-phase spectrum and the fitted curve plotted on the log-log scale.

us assume that $N(E_F) = g_0 \neq 0$ and consider a small energy interval E centered at E_F. The mean distance R between the states within this interval is $R \simeq (g_0 E)^{-\frac{1}{3}}$ since $N(E)R^3E \simeq 1$. If $E \ll \Delta \equiv e^3 g_0^{\frac{1}{2}}/(4\pi\kappa)^{\frac{3}{2}}$, the mean interaction energy between the states $e^2/4\pi\kappa R = (e^2/4\pi\kappa)(g_0 E)^{\frac{1}{3}}$ exceeds E and Eq. (4.7) breaks down. Therefore, $N(E_F) = 0$ must hold. Next, if we assume $N(E) \propto E^\nu$, it is easily deduced in a similar manner that $\nu \geq 2$ should hold in order to satisfy Eq. (4.7) for any $E < \Delta$. Indeed, under long-range Coulomb interaction, numerical calculations [4.38] have shown that the density of single-particle states has the form of Eq. (4.6) around E_F. The width Δ_C of the soft Coulomb gap is given by:

$$\Delta_C = e^3 \sqrt{\frac{N_0}{\kappa^3}}. \tag{4.8}$$

where N_0 is the noninteracting density of states at E_F. The opening of the Coulomb gap reflects the fact that electrons in Ti_4O_7 are localized around E_F. As far as the lineshape is concerned, the HI-phase spectra agree well with the ES theory.

The magnitude of the Coulomb gap Δ_C has been estimated as follows: If we assume a free-electron-like parabolic dispersion for Ti_4O_7, N_0 is of order of $\sim 1 \times 10^{-2}$ eV^{-1}Å^{-3}, a typical value for simple metals. Although there is no reported κ value for Ti_4O_7, if κ is taken to be ~ 10 as in an ordinary semiconductor, Δ_C is estimated to be ~ 0.2 eV. If we take $\gamma = 70$–80 mJ/K^{2}mol [4.7, 8], N_0 equals $\sim 7 \times 10^{-2}$ eV^{-1}Å^{-3}, yielding $\Delta_C \sim 0.5$ eV. As the estimated Δ_C falls in the same range as our observation, we may conclude that the peculiar HI-phase spectra are consistent with the opening of the Coulomb gap.

Experimentally, the Coulomb gap was observed in tunneling spectroscopy measurements for the doped semiconductor Si:B [4.39, 40], whose gap was very small 0.75 meV due to low N_0. As for PES measurements, Davies and Franz [4.38] first pointed out the possibility of a Coulomb gap opening in the spectra of $Na_xTa_yW_{1-y}O_3$ [4.41]. At the same time, they predicted the possible existence of a Coulomb gap for Ti_4O_7 and Fe_3O_4, too, while no quantitative analysis on the experimental spectra has been performed yet. In this sense, the result of $I \propto (E - E_F)^2$ with a plausible Δ_C in the HI-phase spectra of Ti_4O_7 is the first indication of a Coulomb gap using PES. Since our measurements were performed on cleaved surfaces, extrinsic effects such as disorder induced by scraping can be safely excluded. There might exist defects in the cleaved surfaces of Ti_4O_7, but the influence of them is not supposed to be significant since the spectra of Ti_4O_7 show the distinct hard gap in the LI phase below T_{SS} signaling the charge ordering. Such an ordering gap would not be observed if the defects affected as a random potential at the surface which is also implied by the dramatic impurity effect as seen in Fig. 4.5 (c). It should also be emphasized that substitutional

compounds such as $LaNi_{1-x}T_xO_3$ (T = Mn, Fe, and Ni) [4.35] has static disorder, while Ti_4O_7 is a dynamically disordered system. As we shall see below, Fe_3O_4 shows a similar Coulomb gap behavior.

However, there remain some problems to be solved for the above interpretation of the photoemission spectra. The first is about how the bipolaron-liquid nature influences the HI-phase spectra. If the bipolarons are stable objects, a finite energy will be needed to extract a photoelectron from a bipolaron as was observed in the LI-phase spectra, but the HI-phase spectra show only a soft gap. Here, the result of the EPR study may be relevant. According to Lakkis *et al.* [4.4], EPR measurements detected signals from Ti^{3+} centers of impurity origin for the LI phase and detected no signals for the HI phase. This indicates that Ti^{3+} centers with lifetime shorter than 10^{-10} sec may exist in the HI phase [4.4]. Such a short life time is, however, much longer than the time scale of photoemission process and therefore the dynamical disorder is expected to play a dominant role in the PES spectra, resulting in the Coulomb gap. The second problem is the consistency with the electrical resistivity ρ. The $\log \rho$-$T^{-\frac{1}{4}}$ plot of $(Ti_{1-x}V_x)_4O_7$ in Fig. 4.6 shows VRH behavior at low temperatures, which supports the existence of localized states around E_F. However, $\log \rho$ should behave as $\propto T^{-\frac{1}{2}}$ rather than $\propto T^{-\frac{1}{4}}$ if the Coulomb gap exists [4.42]. Unambiguous determination of the exponent seems difficult in this case from the data shown in Fig. 4.6 since the temperature range is not wide enough. In addition, the LI-phase Ti_4O_7 also shows power-law behavior of $\log \rho$ presumably due to dilute impurity, while this fact does not necessarily contradict with the observed hard gap in the LI phase in the PES spectra since the density of states giving rise to such VRH process with large resistivity is supposed to be too small to be detected in PES measurements.

Schematic Diagram of the Spectra

So far, we have discussed the PES spectra of the M, HI, and LI phases in detail. In Fig. 4.17, schematic diagrams for the DOS of the three phases are shown. In the M phase, the single-particle excitation spectrum has a reduced coherent part with large spectral weight in the incoherent part, reflecting strong electron correlation as well as electron-lattice coupling. This results in the pseudogap behavior at E_F as shown in the figure. On decreasing temperature down to the HI phase, the lattice becomes softened to allow a temporal formation of polaron pairs, while electrons or bipolarons can hop between sites. This leads to the bipolaron liquid state with relatively low resistivity for a semiconductor. Reflecting the dynamics of bipolarons, the DOS shows an opening of the soft Coulomb gap. This state may be called a bipolaronic Wigner glass as was pointed out repeatedly [4.6, 9, 11]. On further decreasing temperature into the LI phase, the lattice becomes softened enough to capture electrons. To lower the total energy of localized

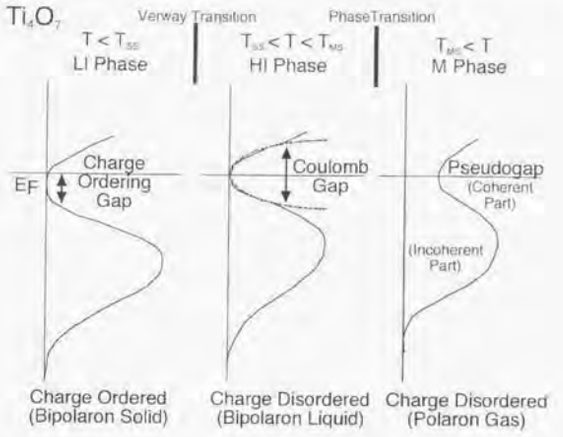

Figure 4.17: Schematic diagrams of DOS for the M, HI, and LI phases of Ti_4O_7.

bipolarons, a charge ordered state is realized with a hard gap, which may be called "Verwey" gap. While only the most dominant aspect is emphasized for each phase in Fig. 4.17 for simplicity, the electron-electron interaction and the electron-lattice interaction are competing in all the phases. To add to both, the effect of disorder is found to influence significantly on the HI-phase spectra.

4.3.3 Comparison with Fe_3O_4

It is worth comparing Ti_4O_7 in the HI phase with Fe_3O_4 above the Verwey transition temperature $T_V \simeq 120$ K. It has been believed that charges are ordered below T_V while they are disordered above T_V, leading to the characteristic transport properties of this materials. Chainani *et al.* [4.15] reported a high-resolution PES study of this compound at various temperatures. Here, we present an analysis of their result in the context of a Coulomb gap driven by disorder. Figure 4.18 (a) shows the spectra of Fe_3O_4 measured using $h\nu = 21.2$ eV with the instrumental resolution of 70 meV. As shown in Fig. 4.18 (a), they observed that the intensity at E_F in the metallic phase evolves as the temperature increases. They concluded that it reflects the existence of short-range order (SRO) above T_V while SRO is gradually lost with increasing temperature. As was performed for Ti_4O_7 in Fig. 4.15, we have plotted the spectra against E_B^2 for $E_B > 0$ and $-E_B^2$ for $E_B < 0$ in Fig. 4.18 (b). It becomes clearer that the intensity at E_F increases as the temperature rises as Chainani *et al.* [4.15] pointed out, and more interest-

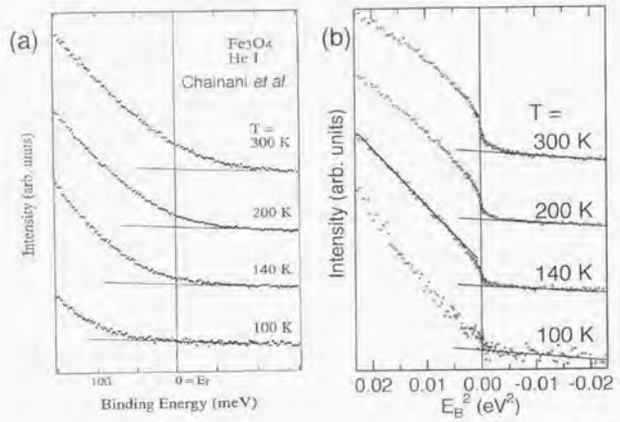

Figure 4.18: (a) Spectra of Fe_3O_4 at 100 K ($\leq T_V$), 140 K ($> T_V$), 200 K, and 300 K measured using $h\nu = 21.2$ eV [4.15]. (b) Plotted against E_B^2 for $E_B > 0$ and $-E_B^2$ for $E_B < 0$. The solid line in the 140 K spectrum is guide to the eye.

ingly, it is found that the 140 K spectrum almost falls on a straight line at $E_B \gtrsim 0.07$ eV ($\sim$ instrumental resolution). In contrast, the 100 K spectrum is slightly concave, signaling a hard gap, while the 200 K and 300 K spectra are convex. This observation is analogous to the LI-, HI-, and M-phase spectra of Ti_4O_7. It is therefore implied that disorder inherent in Fe_3O_4 plays a significant role in the PES spectra around T_V. Fe_3O_4 is, however, different from Ti_4O_7 in that the 140 K spectrum, which would correspond to the HI-phase spectra of Ti_4O_7, does not vanish at E_F but shows a clear Fermi edge as is the high-temperature metallic state at $T > 200$ K. The difference between Ti_4O_7 in the HI phase and Fe_3O_4 just above T_V is probably related to the difference magnitudes of the conductivity (~ 0.1 versus $\sim 10\ \Omega^{-1}\mathrm{cm}^{-1}$, respectively) between these compounds, although both show characteristic sign of disorder.

We have performed a quantitative lineshape analysis on Fe_3O_4. Similar to Eq. (4.4), we have modeled the spectra $I(E = E_B, T)$ at 140 K, 200 K, and 300 K with four parameters as follows:

$$I(E,T) = I_0(E,T) + I_{bg}(E), \tag{4.9}$$

where $I_0(E,T)$ for 140 K, 200 K, and 300 K is the intrinsic part expressed as:

$$I_0(E,T) = (a_2E^2 + a_0)F_{FD}(E,T). \tag{4.10}$$

where a_0 represents a finite intensity at E_F. Only for the 100 K spectrum, $I_0(E,T)$ is assumed to be,

$$I_0(E,T) = \begin{cases} a_2(E - E_0)^2, & \text{for } E \gtrsim E_0 \\ 0, & \text{for } E < E_0, \end{cases} \tag{4.11}$$

where E_0 represents a hard gap. Finally, $I_{bg}(E)$ represents the linear background of the PES spectra given by

$$I_{bg}(E) = b_1E + b_0. \tag{4.12}$$

Since the intensity of the spectra of Fe_3O_4 is very low around E_F, it was necessary to assume the linear background due to the satellites of the photon source[6]. Instrumental resolution was included through the convolution of $I(E,T)$ with a Gaussian of FWHM ~ 70 meV [4.15].

The fitting was satisfactorily performed as shown in Fig. 4.19 (a) between $E_B = -0.15$ eV and 0.15 eV. The 100 K spectrum shows a hard gap of $E_0 \sim 50$ meV as indicated by an arrow. In Fig. 4.19 (b), the results of the fitting $I_0(E,T)$ are shown without the background $I_{bg}(E)$ and the instrumental broadening. The dashed curves represent the original density of states without the finite-temperature Fermi-Dirac function (namely, $I_0(E, T = 0)$, the cut off at E_F in order to clarify the finite DOS at E_F). The most interesting point of this fitting is that the finite intensity at E_F evolves systematically with increasing temperature. In Fig. 4.20, the ratio a_0/a_2 between the intensity at E_F, which contributes to the "metallic" conductivity, and the magnitude of the E^2 term, which represents the disorder, is shown. The electrical conductivity data of Fe_3O_4 [4.45] is superimposed in the figure. The a_0/a_2 values at 140 K, 200 K, and 300 K form a straight line which extrapolates to 0 at 119 ± 5 K $\sim T_V$. This observation, namely, $a_0/a_2 \propto T - T_V$ strongly indicates that the $I_0 \propto (E - E_F)^2$ holds just above T_V. As temperature goes up above T_V, the finite intensity at E_F grows up in proportion to $T - T_V$. J.-H. Park *et al.* [4.44] reported that the spectra of Fe_3O_4 at 130 K show no Fermi edge, which is naturally understood as due to the small a_0/a_2. Their result seems to obey $I \propto (E - E_F)^2$, supporting our analysis.

Schematic diagrams for the DOS of Fe_3O_4 are shown in Fig. 4.21. Since the electronic structure of Fe_3O_4 just above T_V shows a strong analogy with Ti_4O_7 in the HI phase, we propose that the Coulomb gap exists in Fe_3O_4 just above T_V and continuously evolves into a pseudogap well above T_V. While charges are ordered in Fe_3O_4 below T_V, the order-disorder transition occurs at

[6]Unlike the case of Fe_3O_4, the satellite of the photon source, which is composed of $h\nu = 23.09$, 23.75, and 24.05 eV for $h\nu = 21.22$ eV [4.43], gives only negligibly small influence on the spectra of Ti_4O_7 around E_F because the structure around $E_B = 2$ eV in them is almost flat as shown in Fig. 4.8, while there exists a large feature in the spectra of Fe_3O_4 around $E_B = 2$ eV [4.15].

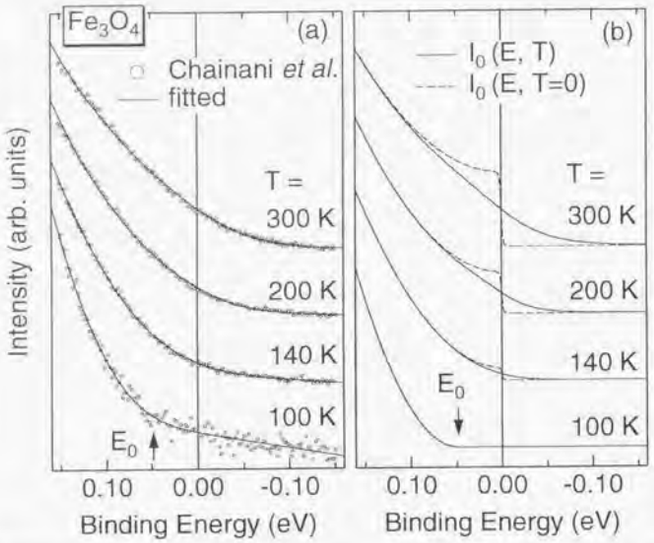

Figure 4.19: (a) Results of the fitting of the PES spectra of Fe_3O_4. Open circles and solid lines show the experimental spectra and the fitted curve $I(E,T)$, respectively. (b) Results of the fitting without the background $I_{bg}(E)$. The solid curve and dashed curve represent $I_0(E,T)$ and $I_0(E,T=0)$ (cut off at E_F), respectively. The arrows in (a) and (b) represent E_0.

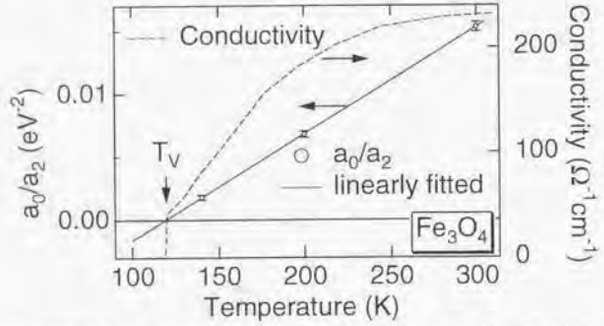

Figure 4.20: Ratio a_0/a_2 [see Eq. (4.10)] indicating $a_0/a_2 \propto T - T_V$. Electrical conductivity of Fe_3O_4 is also shown by a dashed line [4.45].

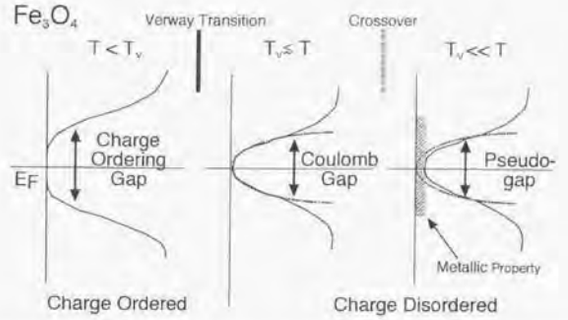

Figure 4.21: Schematic diagrams of DOS of Fe_3O_4 for the charge-ordered phase ($T < T_V$), the charge-disordered phase with strong SRO ($T \gtrsim T_V$), and the charge-disordered phase with weak SRO ($T \gg T_V$).

T_V, above which charges are disordered with finite SRO, namely, the system is in the Wigner glass state [4.42]. This results in the Coulomb gap at T_V and the pseudogap above T_V in the PES spectrum. The SRO is gradually lost and the system becomes more uniform and more metallic as the temperature goes up, which yields the temperature-dependent intensity at E_F. This picture is consistent with recent optical study of Fe_3O_4 [4.45] in that the effective number of electrons monotonously increases above T_V up to 300 K. In Ti_4O_7, the temperature range of the HI phase is only a few K and the first-order phase transition into the M phase occurs and, therefore, such a crossover-like behavior as in the case of Fe_3O_4 is not observed. We therefore conclude that disorder possibly plays an important role in the physical properties in Fe_3O_4 above T_V as well as in the HI-phase Ti_4O_7.

Finally, two points are remarked. First, one cannot totally exclude the presence of a tiny Fermi-edge in the HI-phase spectra of Ti_4O_7 from the experimental data. In fact, by fitting the HI-phase spectra of Ti_4O_7 with Eq. (4.10) instead of Eq. (4.4), we have obtained a finite value of $a_0/a_2 \lesssim 2 \times 10^{-3}$ eV^{-2} which seems to decrease to zero toward T_{SS}. In the case of the spectrum shown in Fig. 4.16 (b), for example, the obtained $a_0/a_2 \sim 0.5 \times 10^{-3}$ eV^{-2} give a finite Fermi edge, but is not larger than the error bar. Thus, the finite a_0/a_2 seems too small and temperature range of the HI phase too narrow for the purpose of accurate discussion as performed for Fe_3O_4. A precise PES study of the V-substituted compounds $(Ti_{1-x}V_x)_4O_7$ around their phase-transition temperatures may serve for more quantitative discussion on the temperature-dependent finite DOS at E_F coexisting with the Coulomb gap. As a second remark, the real Wigner glass state seems unstable toward charge

ordering in both Ti_4O_7 and Fe_3O_4. Indeed, approaching from the metallic side, Fe_3O_4 undergoes the Verwey transition into a charge-ordered state as soon as a_0/a_2 reaches 0. Presumably, similar Coulomb-gap behavior could be observed in other systems such as β-$Na_xV_2O_5$ ($0.3 \leq x \leq 0.4$), a bipolaronic compound [4.9, 46] where an order-disorder transition of bipolarons occurs at ~ 200 K [4.47, 48].

4.4 Conclusion

In conclusion, we have performed a PES study of Ti_4O_7 covering its LI, HI, and M phases. While the O $2p$ band is almost insensitive to the temperature variation, the spectra of the Ti $3d$ band show characteristic temperature-dependent spectra corresponding to the three phases. Effects of thermal hysteresis were also observed in the PES spectra. The spectra of the M phase are similar to the spectra of three-dimensional vanadium and titanium oxides with $3d^1$ configuration, reflecting the strong electron-correlation inherent in this system. In the spectra of the LI phase, a finite gap was observed. We discussed its lineshape in terms of electron-phonon interaction. The spectra of the HI phase are gapless and can be fitted to $(E - E_F)^2$ near E_F. We interpreted this as a soft Coulomb gap resulting from a bipolaron liquid state or a bipolaronic Wigner glass. By re-analyzing the PES spectra of Fe_3O_4, the Coulomb gap was also found just above T_V, indicating the significant role of disorder and long-range Coulomb interaction in the metallic phase of Fe_3O_4. With increasing temperature, the Coulomb gap in Fe_3O_4 is found to continuously evolve into a pseudogap in the metallic state, whereas the first-order HI-to-M transition in Ti_4O_7 precludes the observation of the corresponding continuous change. We have pointed out that disorder possibly plays an important role in the physical properties of Fe_3O_4 above T_V as well as in the HI-phase Ti_4O_7.

References

[4.1] S. Andersson, B. Collen, U. Kuylenstierna, and A. Magnéli, Acta Chem. Scand. **11**, 1641 (1957).

[4.2] M. Marezio, D. B. McWhan, P. D. Dernier, and J. P. Remeika, Phys. Rev. Lett. **28**, 1390 (1972).

[4.3] C. Schlenker, S. Lakkis, J. M. D. Coey, and M. Marezio, Phys. Rev. Lett. **32**, 1318 (1974).

[4.4] S. Lakkis, C. Schlenker, B. K. Chakraverty, R. Buder, and M. Marezio, Phys. Rev. B **14**, 1429 (1976).

[4.5] C. Schlenker, S. Ahmed, R. Buder, and M. Gourmala, J. Phys. C: Solid State Phys. **12**, 3503 (1979).

[4.6] C. Schelenker and M. Marezio, Philos. Mag. B **42**, 453 (1980).

[4.7] T. Tonogai, Doctor Thesis, (Tokyo University, 1998).

[4.8] T. Tonogai, H. Takagi, C. Murayama, and N. Mori, Rev. High Pressure Sci. Technol. **7**, 453 (1998).

[4.9] C. Schlenker, *Physics of Disordered Materials*, eds. by D. Alder, H. Fritzsche, and S. Ovshinsky (Plenum, New York, 1985) p. 369.

[4.10] Y. Le Page and M. Marezio, J. Solid State Chem. **53**, 13 (1984).

[4.11] B. K. Chakraverty, Philos. Mag. B **42**, 473 (1980).

[4.12] E. J. W. Verwey and P. W. Haaymann, Physica **8**, 979 (1941).

[4.13] M. Abbate, R. Potze, G. A. Sawatzky, C. Schlenker, H. J. Lin, L. H. Tjeng, C. T. Chen, D. Teehan and T. S. Turner, Phys. Rev. B **51**, 10150 (1995).

[4.14] M. Abbate, R. Potze, G. A. Sawatzky, C. Schlenker, D. Teehan and T. S. Turner, Solid State Commun. **94**, 465 (1995).

[4.15] A. Chainani, T. Yokoya, T. Morimoto, T. Takahashi, and S. Todo, Phys. Rev. B **51**, 17976 (1995).

[4.16] J. Mercier and S. Lakkis, J. Crystal Growth **20**, 195 (1973).

[4.17] J. J. Since, S. Ahmed, and J. Mercier, J. Crystal Growth **40**, 301 (1977).

[4.18] D. Kaplan, C. Schelenker, and J. J. Since, Philos. Mag. **36**, 1275 (1977).

[4.19] F. Zwick, H. Berger, I. Vobornik, G. Margaritondo, L. Forró, C. Beeli, M. Onellion, G. Panaccione, A. Taleb-Ibrahimi, and M. Grioni, Phys. Rev. Lett. **81**, 1058 (1998).

[4.20] W. A. Harrison, *Electronic Structure and the Properties of Solids* (Dover, New York, 1989).

[4.21] A. Fujimori, I. Hase, H. Namatame, Y. Fujishima, Y. Tokura H. Eisaki, S. Uchida K. Takegahara, and F. M. F. de Groot, Phys. Rev. Lett. **69**, 1796 (1992).

[4.22] I. H. Inone, I. Hase, Y. Aiura, A. Fujimori, Y. Haruyama, T. Maruyama, and Y. Nishihara, Phys. Rev. Lett. **74**, 2539 (1995).

[4.23] K. Morikawa, T. Mizokawa, K. Kobayashi, A. Fujimori, H. Eisaki, S. Uchida, F. Iga, and Y. Nishihara, Phys. Rev. B **52**, 13711 (1995).

[4.24] D. B. McWhan, J. P. Remeika, T. M. Rice, W. F. Brinkman, J. P. Maita, and A. Menth, Phys. Rev. Lett. **27**, 941 (1971).

[4.25] P. W. Anderson, Phys. Rev. Lett. **34**, 953 (1975).

[4.26] B. K. Chakraverty and C. Schlenker, J. Physique **37**, C4-353 (1976).

[4.27] A. L. Fetter and J. D. Walecka, *Quantum Theory of Many-Particle Systems* (McGraw-Hill, San Francisco, 1971).

[4.28] M. Vekić and S. R. White, Phys. Rev. B **48**, 7643 (1993).

[4.29] A. S. Alexandrov and P. E. Kornilovitch, Phys. Rev. Lett. **82**, 807 (1999).

[4.30] E. Berger, P. Valášek, and W. von der Linden, Phys. Rev. B **52**, 4806 (1995) and references there in.

[4.31] P. W. Anderson, Phys. Rev. **109**, 1492 (1958).

[4.32] B. L. Althsuler and A. G. Aronov, Solid State Commun. **30**, 115 (1979).

[4.33] W. L. McMillan and J. Mochel, Phys. Rev. Lett. **46**, 556 (1981).

[4.34] A. E. White, R. C. Dynes, and J. P. Garno, Phys. Rev. Lett. **56**, 532 (1986).

[4.35] D. D. Sarma, A. Chainani, S. R. Krishnakumar, E. Vescovo, C. Carbone, W. Eberhardt, O. Rader, Ch. Jung, Ch. Hellwig, W. Gudat, H. Srikanth, and A. K. Raychaudhuri, Phys. Rev. Lett. **80**, 4004 (1998).

[4.36] A. L. Efros and B. I. Shklovskii, J. Phys. C **8**, L49 (1975).

[4.37] B. I. Shklovskii and A. L. Efros, Fiz. Tekh. Poluprovodn. **14**, 825 (1980) [Sov. Phys. Semicond. **14**, 487 (1980)].

[4.38] J. H. Davies and J. R. Franz, Phys. Rev. Lett. **57**, 475 (1986).

[4.39] J. G. Massey and M. Lee, Phys. Rev. Lett. **75**, 4266 (1995).

[4.40] J. G. Massey and M. Lee, Phys. Rev. Lett. **77**, 3399 (1996).

[4.41] G. Hollinger, P. Pertosa, J. P. Doumerc, F. J. Himpsel, and B. Reihl, Phys. Rev. B **32**, 1987 (1985).

[4.42] N. F. Mott, *Metal-Insulator Transitions* (Taylor and Francis, London, 1990).

[4.43] M. Cardona and L. Ley, in *Photoemission in Solids*, edited by M. Cardona and L. Ley (Springer-Verlag, Berlin, 1978), Vol. I.

[4.44] J.-H. Park, L. H. Tjeng, J. W. Allen, P. Metcalf, and C. T. Chen, Phys. Rev. B **55**, 12813 (1997).

[4.45] S. K. Park, T. Ishikawa, and Y. Tokura, Phys. Rev. B **58**, 3717 (1998).

[4.46] B. K. Chakraverty, M. J. Sienko, and J. Bonnerot, Phys. Rev. B **17**, 3781 (1978).

[4.47] Y. Kanai, S. Kagoshima and H. Nagasawa, J. Phys. Soc. Jpn. **51**, 697 (1982).

[4.48] Y. Kanai, S. Kagoshima and H. Nagasawa, Synth. Met. **9**, 369 (1984).

Chapter 5

Insulator-Superconductor Transition in $Ba_{1-x}K_xBiO_3$

We have performed x-ray absorption spectroscopy (XAS) and x-ray photoemission spectroscopy (XPS) studies of single crystal $Ba_{1-x}K_xBiO_3$ (BKBO) covering the whole composition range $0 \leq x \leq 0.60$. Several features in the oxygen 1*s* core XAS spectra show systematic changes with x. Spectral weight around the absorption threshold increases with hole doping and shows a finite jump between $x = 0.30$ and 0.40, which signals the metal-insulator transition. We have compared the obtained results with band-structure calculations. Comparison with the XAS results of $BaPb_{1-x}Bi_xO_3$ (BPBO) has revealed quite different doping dependences between BKBO and BPBO. We have also observed systematic core-level shifts in the XPS spectra as well as in the XAS threshold as functions of x, which can be attributed to a chemical potential shift accompanying the hole doping. The observed chemical potential shift is found to be slower than that predicted by the rigid band model based on the band-structure calculations. We analyze the dependence of the chemical potential shift on the hole doping in terms of a simple Fermi-liquid theory and discuss a possible relevance of the pseudogap in the metallic phase.

5.1 Introduction

The hole-doped bismuthate $Ba_{1-x}K_xBiO_3$ (BKBO) has been fascinating researchers since its discovery [5.1, 2] for its diverse physical properties such as superconductivity, metal-insulator transition and charge-density wave

The content of this chapter was reported in: K. Kobayashi, T. Mizokawa, A. Ino, J. Matsuno, A. Fujimori, H. Samata, A. Mishiro, Y. Nagata, and F. M. F. de Groot: Doping Dependence of the Electronic Structure of $Ba_{1-x}K_xBiO_3$ Studied by X-Ray Absorption Spectroscopy, Phys. Rev. B **59**, 15100 (1999).

Figure 5.1: Basic crystal structure of BKBO is, i. e., the three-dimensional perovskite structure. The BiO_6 octahedra are tilted and shows breathing for $x < x_c$.

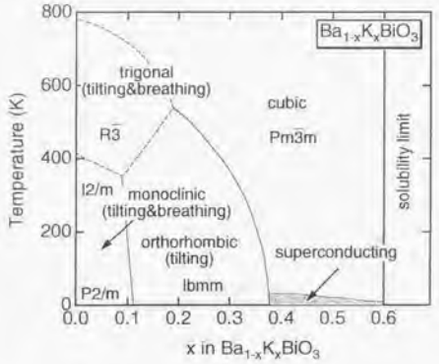

Figure 5.2: Phase diagram of the BKBO system with the corresponding space groups. "tilting" and "breathing" indicates those of the BiO_6 octahedra [5.3, 11] as drawn in Fig 5.3.

(CDW) formation. Although it is basically a simple three-dimensional perovskite as shown in Fig. 5.1, the crystal structure is actually distorted ($0 \leq x < x_c$) or cubic ($x_c < x$) depending on x, where $x_c \sim 0.38$. Figure 5.2 shows the complicated phase diagram of BKBO showing the tilting or breathing of the constituent BiO_6 octahedra for $x < x_c$ [5.3]. In Fig. 5.3, some examples of the tilting or breathing of BKBO are shown.

The parent compound $BaBiO_3$ is an insulator in contrast to the prediction of many band-structure calculations that it is a metal with the half-filled non-degenerate Bi 6*s*-O 2*p* antibonding band crossing the Fermi level (E_F) [5.4–7] as shown in Figs. 5.4 and 5.5. This discrepancy between band theory and experiment has been attributed to a charge disproportionation of Bi into Bi^{3+} and Bi^{5+} sites or a CDW formation accompanied by the breathing of

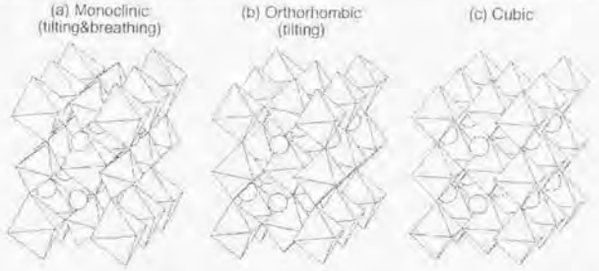

Figure 5.3: Tilting and breathing of the BiO_6 octahedra in BKBO [5.3]. Circles denote Ba or K ions. (a) Monoclinic structure with tilting and breathing. (b) Orthorhombic structure with tilting. (c) Cubic structure.

the BiO_6 octahedra [5.4, 8]. However, calculations on hypothetical charge-ordered states failed to open the band gap and the importance of electron correlation effect was suspected [5.5, 9]. More recently, a band-structure calculation which takes into account both the breathing and tilting distortion indeed predicted the opening of an indirect gap [5.10].

By increasing x from 0, i. e., by hole doping into $BaBiO_3$, BKBO undergoes a semiconductor-to-superconductor transition at $x = x_c$. The transition temperature (T_C) is highest ~ 30 K at $x = x_c$ [5.2], which is the highest among the copper-free oxides. It remains superconducting up to $x \sim 0.6$, above which there is a solubility limit of K atoms [5.11]. Those striking properties have often been compared with those of the typical cuprate system $La_{2-x}Sr_xCuO_4$ (LSCO), which also shows a transition from the insulating La_2CuO_4 into the superconducting phase with hole doping. Unlike BKBO, however, the crystal structure of LSCO is of the layered perovskite type and the parent material La_2CuO_4 is an antiferromagnetic insulator rather than a CDW insulator. It is noted that BKBO bears a close relationship with the $BaPb_{1-x}Bi_xO_3$ (BPBO) system, which shows superconductivity between $x = 0$ and ~ 0.35 with the maximum T_C of ~ 12 K around $x \sim 0.25$ [5.12]. The origin of the superconductivity in BKBO as well as in BPBO has not been settled yet: Both systems are *sp* electron systems without magnetic ions, excluding the possibility of magnetic pairing mechanisms.

To explain the characteristic properties of BKBO and BPBO, many theoretical studies including the band-structure calculations were reported. While the band-structure calculations could explain the CDW formation in $BaBiO_3$ as described above, Takegahara [5.9] pointed out that the observed breathing-mode distortion theoretically induces only a direct gap ~ 0.9 eV which is quite a small value compared to the optical gap of ~ 2 eV [5.13] and, therefore, that the finite gap formation in BPBO ($0.3 < x < 1$) is due to a correlation effect of the Bi 6*s* electrons. In this sense, electron correlation

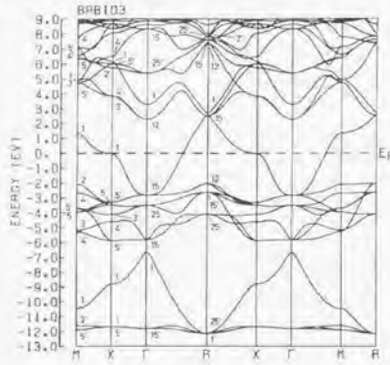

Figure 5.4: Calculated energy band structure of $BaBiO_3$. The Bi 6*s*-O 2*p* antibonding band is crossing E_F [5.5].

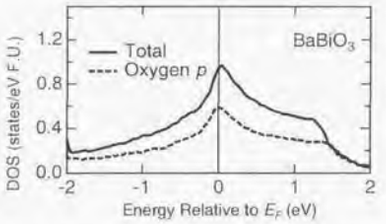

Figure 5.5: Calculated total and oxygen *p* partial density of states (DOS) of $BaBiO_3$ around E_F. DOS around E_F comes from Bi 6*s*-O 2*p* antibonding band [5.5].

within the Bi 6*s* band should not be neglected compared to the electron-lattice interaction in spite of the general recognition that the 6*s* electrons form a weakly correlated system. Actually, the latter overcomes the former in $BaBiO_3$, yielding the stable Bi^{3+} sites which are doubly occupied by 6*s* electrons. In the most simplest case, such a system was treated using the negative-U Hubbard model starting from the charge-disproportionated state $Ba_2(Bi^{3+}Bi^{5+})O_6$ [5.14, 15], which could explain the gap formation and the doping dependence of the superconductivity qualitatively. As another approach, using the Holstein model, Noack *et al.* [5.16] successfully discussed the competition between CDW and superconductivity as a function of doping in $BaBiO_3$.

Understanding the electronic structure of BKBO is a necessary step to elucidate the mechanism of its superconductivity. So far many experimen-

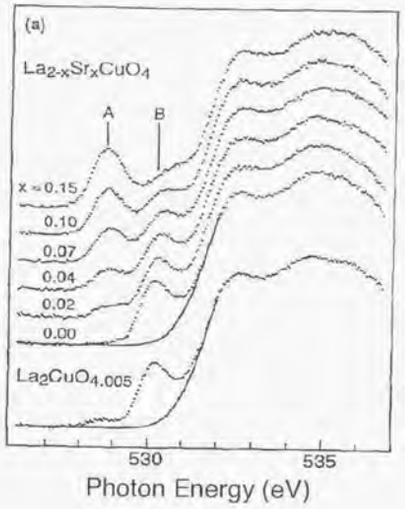

Figure 5.6: O 1*s* XAS spectra of a series of LSCO. It clearly proves that a new state labeled "A" develops in the charge-transfer gap just above the Fermi level by hole doping [5.25].

tal studies have been performed on BKBO including transport, optical and tunneling experiments. Quite a few photoemission studies have also been reported (for example, Refs. [5.17-21]) while there have been relatively few x-ray absorption spectroscopy (XAS) studies [5.22-24]. XAS gives us information about the unoccupied electronic states and, therefore, is suitable for studying the effect of hole doping on the electronic structure, as has been successfully applied to LSCO by Chen *et al* [5.25]. They observed that a new state develops just above the Fermi level by hole doping to the parent compound La_2CuO_4 as shown in Fig. 5.6, clearly proving that the electronic structure of LSCO is described as a doped charge-transfer insulator. As far as BKBO concerns, Salem-sugui *et al.* [5.22] observed a prepeak in the O 1*s* XAS spectra for BKBO with $x = 0.0$, 0.2 and 0.4 and a continuous change across the transition $x \sim x_c$ was observed. Qvarford *et al.* [5.23] also reported result for $x = 0.1$ and 0.4 and obtained similar results. A systematic study covering a wider concentration range, however, has been lacking.

In this chapter, we report on a detailed XAS study of $Ba_{1-x}K_xBiO_3$ using single crystals covering the entire available K concentration range ($0 \leq x \leq 0.60$) for the first time. Gradual and systematic x-dependent changes were observed for several features in the XAS spectra. We compare these results

with the band-structure calculations and with the XAS results of BPBO. A quantitative analysis has been made on the spectral weight of the prepeak. Contrasting doping behaviors have been revealed between BKBO and BPBO. We also performed XPS measurements on the core levels of BKBO. The observed core-level shifts will be discussed in terms of the chemical potential shift due to the hole doping.

5.2 Experiment

$Ba_{1-x}K_xBiO_3$ single crystals ($x = 0.10$, 0.20, 0.30, 0.40, 0.50 and 0.60), which were offered by Prof. Y. Nagata, Dr. H. Samata, and Mr. A. Mishiro of Aoyama-Gakuin University, were grown by an electrochemical method from a KOH solution with $Ba(OH)_2 \cdot 8H_2O$ and Bi_2O_3. The composition of each sample was determined by EPMA [5.26]. A $BaBiO_3$ single crystal supplied by Prof. H. Takagi of ISSP, University of Tokyo was prepared by the flux method.

XAS measurements were performed at beamline BL-2B of Photon Factory, High Energy Accelerator Research Organization, where the highest instrumental resolution was expected around the O 1*s* absorption edge among beamlines in Japan. Photon energies were calibrated using the Cu $2p_{3/2}$ edge of Cu metal at 932.5 eV [5.27] and the O 1*s* edge of $LaCoO_3$ at 529.3 eV [5.28]. O 1*s* XAS spectra were taken by the total electron-yield method with photoelectrons. The energy resolution including the lifetime of the O 1*s* core hole was ~ 0.7 eV at 530 eV. The samples were cooled down to ~ 50 K using a closed-cycle He refrigerator. The pressure in the spectrometer was $\sim 4 \times 10^{-10}$ Torr.

XPS measurements were performed using the Mg Kα line ($h\nu = 1253.6$ eV) and photoelectrons were collected using a PHI DCMA. Calibration and estimation of the instrumental resolution were done using gold evaporated on the sample surface defining Au $4f_{7/2} = 84.0$ eV. The total resolution was ~ 1 eV, including both the light source and the instrumental resolution. The base pressure in the spectrometer was $\sim 6 \times 10^{-10}$ Torr. All the XPS measurements were performed at room temperature in order to avoid charging effect in the insulating phase.

The samples were scraped *in situ* with a diamond file for both measurements. For the XAS measurements, which are less surface-sensitive than XPS, samples were scraped until the spectra showed no further change. The obtained XAS spectra seem consistent with the previous reports for $x = 0$ [5.29] and $x = 0.40$ [5.24]. For the XPS measurements, scraping was performed until the O 1*s* core-level spectra became a single peak. We confirmed that the measured peak intensity of the Ba 3*d* XPS core level was proportional to x, while those of the O 1*s* and Bi 4*f* core levels were almost independent of x.

5.3 Results and Discussion

5.3.1 Overall Electronic Structure of the Unoccupied States

Figure 5.7 shows the XAS spectra of $Ba_{1-x}K_xBiO_3$ for various x's. We superimpose the spectrum of $BaBiO_3$ ($x = 0.00$) on each spectrum ($x \geq 0.10$) as a solid curve. Normalization of all the spectra was performed by peak height at the photon energy $h\nu = 533$–535 eV. In the bottom, difference spectra from the $BaBiO_3$ spectrum are shown. Notable structures found in the spectra are labeled as *a*–*f* in Fig. 5.7, and the positions of structures *a*–*e* are plotted in Fig. 5.8.

The O 1*s* XAS spectra represent the unoccupied partial density of states (PDOS) of *p* character at the oxygen site. Structure *a* near the absorption edge $h\nu \sim 528.0$–528.5 eV grows almost monotonously as x increases, which is also substantiated in the bottom panel of Fig. 5.7. At $x = 0.00$, the shape of the prepeak *a* is rounded, while it becomes a sharper peak at $x \geq 0.10$. For the spectra $0.10 \leq x \leq 0.30$, where BKBO is insulating, the peak grows slowly as x increases. At $x = 0.40 > x_c$, where BKBO enters the metallic region, the prepeak suddenly becomes intense and keeps its height until $x = 0.60$. The increase of the prepeak is due to the doped holes and the rapid growth from $x = 0.30$ to 0.40 would be attributed to a transfer of spectral weight to the region near the chemical potential, signaling the metal-insulator transition. This behavior is essentially different from that in LSCO (see Fig. 5.6), where new spectral weight appears well below the first peak of the insulator La_2CuO_4. A quantitative discussion about the spectral weight of the prepeak will be made in Sec. 5.3.3.

Next, we investigate the behaviors of structures *b*–*f*. Structure *b*, which appears as a shoulder-like structure for $x = 0.00$ at $h\nu \sim 532$ eV, becomes obscure in going from $x = 0.00$ to 0.30 and disappears at $x \geq 0.40$. Hence, *b* may be attributed to Ba character, which point will be discussed below. The behavior of structure *c* at $h\nu \sim 533$–534 eV and structure *d* at $h\nu \sim 535$ eV is also systematically dependent on x. At $x = 0.00$, feature *c* with a slightly smaller feature *d* is observed. This two-component peak centered around $h\nu \sim 534$ eV is monotonously shifted to higher photon energies with x, until the center of the peak reaches $h\nu \sim 535$ eV. At the same time, *d* becomes stronger than *c* at $x \sim 0.30$ and, finally, structures *c* and *d* merge at $x \geq 0.40$ into a peak as labelled "$c + d$" in Figs. 5.7 and 5.8. This observation can be explained as follows: Structures *c* and *d* are mainly of Ba character at $x = 0.00$, while the substituted states of K character appear at the position of *d* for $x \geq 0.10$ and, therefore, the gradual change results from the change of the electronic structure due to the substitution of K for Ba. As will be discussed in Sec. 5.3.2, this is also supported by the result of the XAS spectra

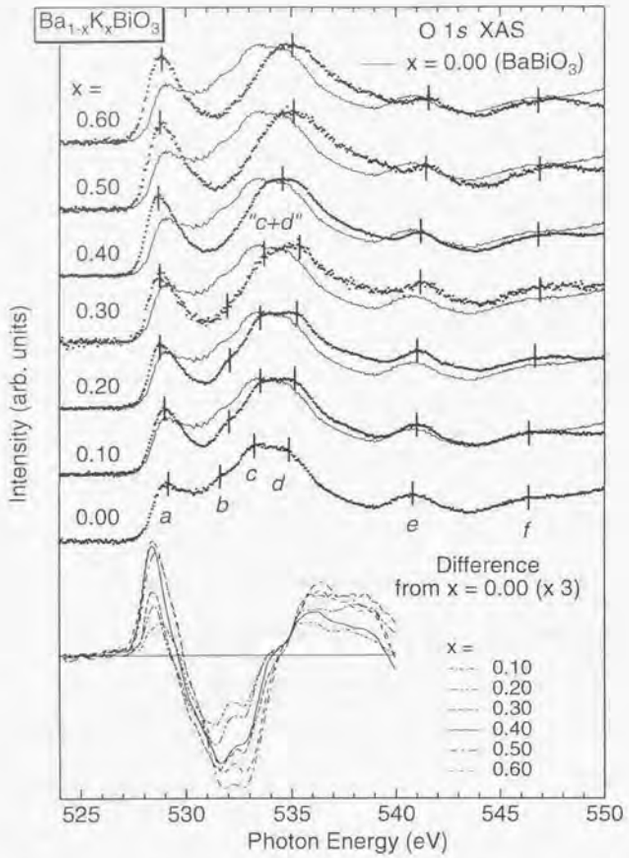

Figure 5.7: Oxygen 1s x-ray-absorption spectra (XAS) of a series of $Ba_{1-x}K_xBiO_3$ ($0 \leq x \leq 0.60$). The spectrum of $BaBiO_3$ is superimposed on each spectrum as a solid curve. They have been normalized to their peak height around $h\nu = 533$–535 eV. The positions of a–e are plotted in Fig. 5.8. In the bottom panel are shown the difference spectra from the XAS spectrum of $BaBiO_3$.

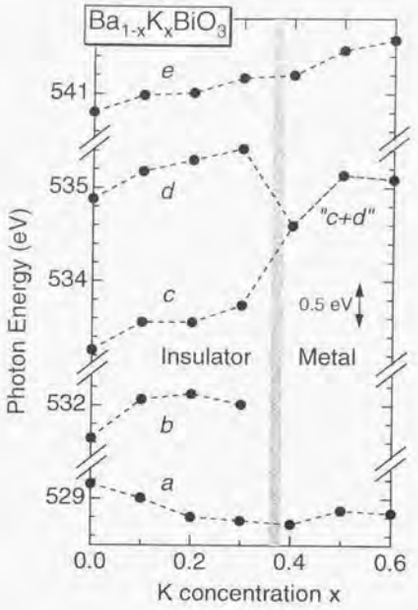

Figure 5.8: Positions of structures a–e indicated in Fig. 5.7.

of BPBO [5.29], where the corresponding e structure does not move to higher photon energies so much as that in BKBO.

Besides a–d, the behaviors of the structures in the higher photon energy region are worth mentioning although they behave less drastically than those near the absorption edge. On one hand, structure e around $h\nu \sim 541$ eV simply becomes weak with x, indicating that this structure is of Ba character. On the other hand, the broader structure f around $h\nu \sim 547$ eV does not change in the entire x range, indicating this to be of Bi or purely of O character.

It is interesting to compare these observations with the previous report on the unoccupied states of BKBO studied by inverse photoemission spectroscopy (IPES) (see Fig. 5.9). Wagener *et al.* [5.21] assigned structures at about 4, 7, 9 and 14 eV above E_F (corresponding structures b–e) to Bi $6p$, Ba $5d$, K $3d$ and Ba $4f$ states, respectively. As for structures c, d and e, their assignment agrees with ours. If b is assigned to the Bi $6p$ band as they identified, our observation that b disappears at $x \geq 0.40$ may indicate a change

of the electronic structure caused by the change of the crystal structure.

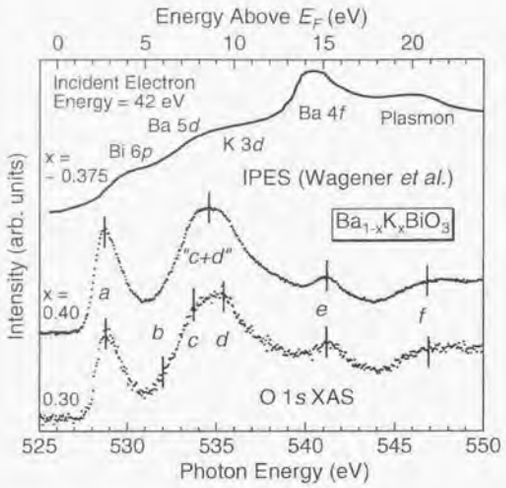

Figure 5.9: In the top panel is shown the IPES spectrum of BKBO [5.21]. The assignments indicated in the figure correspond well to our result of XAS of BKBO shown in the bottom panel. See the text for details.

In Fig. 5.10, we show comparison between the XAS spectra of $BaBiO_3$ and $Ba_{0.9}K_{0.1}BiO_3$ and the theoretical spectrum of $BaBiO_3$ derived from the unoccupied oxygen p PDOS [5.5]. The oxygen PDOS has been broadened with a Gaussian and a Lorentzian which represent the instrumental resolution ~ 0.5 eV and the lifetime broadening of O $1s$ core hole ~ 0.3 eV, respectively [5.29]. The energy scale of the theoretical spectrum has been shifted so as to compare well with the experimental spectra. Structures in the theoretical spectrum are labelled as α–γ. Although the lineshapes of the XAS spectra tend to be distorted by the core-hole potential, the theoretical spectrum reproduces experiment to some extent: Structures α, β and γ seem to correspond to a, b and c (or d), respectively. In addition, it is interesting to note that, as for the prepeak a, the theoretical spectrum resembles the experimental spectrum of $Ba_{0.9}K_{0.1}BiO_3$ rather than that of $BaBiO_3$. Because both samples are insulating, this cannot be explained only by the effect of the core-hole potential. This may be related to the difference of the crystal structure between $x = 0.00$ and $x = 0.10$ since the strong breathing-type distortion and the tilting of the BiO_6 octahedra exist for $x \lesssim 0.1$ with a large electron-phonon coupling constant [5.3, 10].

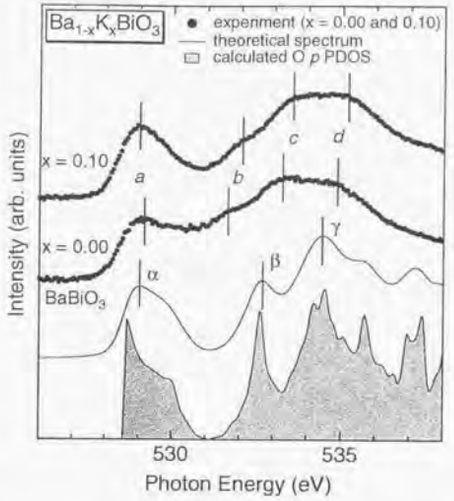

Figure 5.10: Comparison of the XAS spectra of $BaBiO_3$ and $Ba_{0.9}K_{0.1}BiO_3$(dots) with the theoretical spectrum (solid curves) derived from the unoccupied O p PDOS [5.5]. The labels a–d are the same as in Fig. 5.7.

5.3.2 Comparison with the XAS Spectra of BPBO

Next we compare our results with the previous report on the XAS spectra of the BPBO system [5.29]. In the upper panel of Fig. 5.11, the XAS spectra of a series of $BaPb_{1-x}Bi_xO_3$ ($0.0 \leq x \leq 1.0$) are shown by dots, with the $BaBiO_3$ XAS spectrum superimposed for comparison[1]. All the spectra have been normalized to their peak height around $h\nu \sim 534$ eV. We have labelled structures as a–e. In the bottom, the difference spectra from the $BaBiO_3$ spectrum are shown. The positions of structures a–e are plotted in Fig. 5.12.

Although structure b is only weakly visible, structures c, d and e correspond well to those of BKBO in Fig. 5.7. Unlike BKBO, c and d do not greatly change their positions and lineshapes with x. e also does not change its position with x. This supports the above assignment for BKBO that c, d and e are mainly of Ba character. On the other hand, the position and lineshape of the prepeak labelled a change dramatically with x, while their

[1]Here, we have linearly rescaled the photon energies of the spectra measured by de Groot *et al.* [5.29] so that their $BaBiO_3$ result agrees well with ours except for the slightly better energy resolution in the present data. This discrepancy may be due to a technical reason, namely, the method of the photon energy calibration.

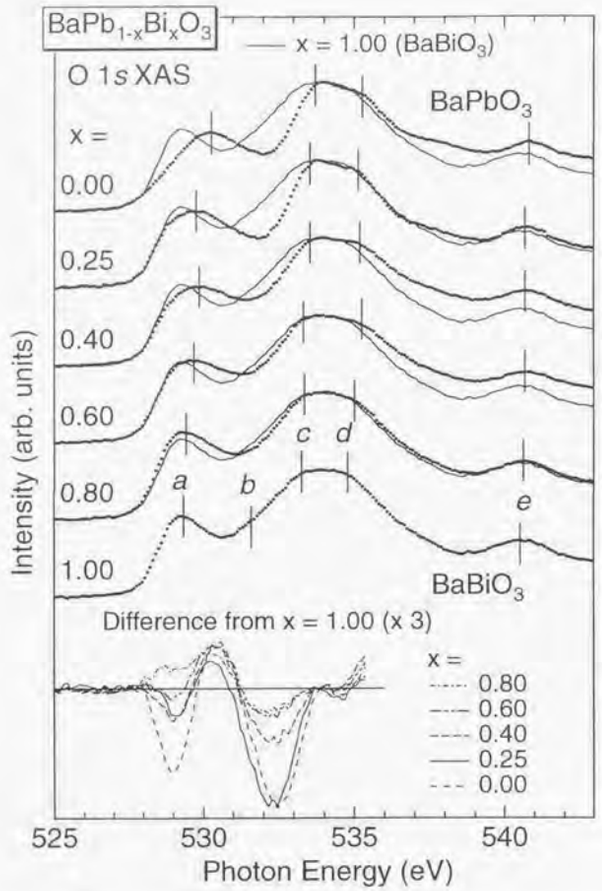

Figure 5.11: O 1*s* XAS spectra of a series of $BaPb_{1-x}Bi_xO_3$ ($0.0 \leq x \leq 1.0$) [5.29]. The spectrum of $BaBiO_3$ is superimposed on each spectrum. They have been normalized to their peak height around $h\nu = 534$ eV. The positions of a–e are plotted in Fig. 5.12. In the bottom panel are shown the difference spectra from that of $BaBiO_3$.

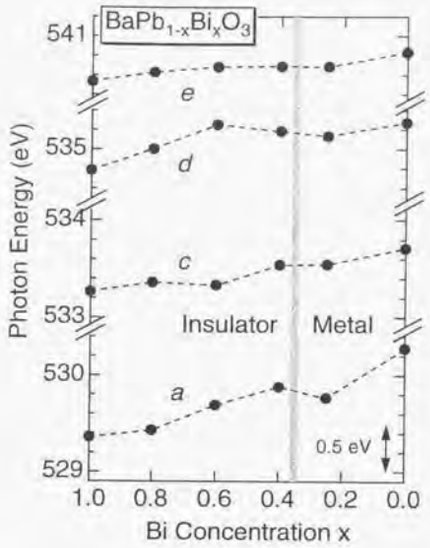

Figure 5.12: Positions of structures a and c–e indicated in Fig. 5.11.

intensity relative to the main peak at $h\nu = 533$–535 eV is conserved. This observation is clearly contrasted with the case of BKBO, where the intensity of the prepeak increases with x. The difference spectra in the bottom panel also clarify this point. As for BPBO, the intensity of the prepeak a a little increases in going from $x = 1.00$ to 0.80, and then decreases almost monotonously as x decreases. Unlike BKBO, there is another structure in the difference spectra at $h\nu \sim 530$ eV, which does not behave systematically, while the broad dip at $\sim$ 532–533 eV increases with decreasing x. Such complicated behaviors significantly differ from those of BKBO, reflecting the different doping processes between BPBO and BKBO. In the former system, the Bi 6*s*-O 2*p* antibonding band is replaced by the Pb 6*s*-O 2*p* antibonding band near E_F. In the latter system, the doped holes are rather simply accommodated in the Bi 6*s*-O 2*p* antibonding band. The different doping processes are also reflected on the opposite shifts of peak a in BKBO and BPBO (Figs. 5.8 and 5.12). Other structures are shifted more slowly in BPBO than in BKBO.

5.3.3 Electronic Structure near the Fermi Level

In this section, we discuss how doped holes are accommodated in the Bi 6*s*-O 2*p* antibonding band in BKBO based on the doping dependence of the intensity of the prepeak. In order to characterize how the prepeak grows with K substitution, the peak around $h\nu$ = 534–535 eV has been subtracted by assuming it to be a Gaussian, as shown in Fig. 5.13. Here, the shaded area represents the extracted prepeak. In Fig. 5.14, the area $N(x)$ of the prepeak relative to that of the Gaussian is plotted as a function of x. We have scaled $N(x)$ so that $N(x = 0.40) = 1.40$ because $N(x)$ would be proportional to the number of empty states in the Bi 6*s*-O 2*p* antibonding band if the strength of the Bi 6*s*-O 2*p* hybridization does not change with x.

In accordance with the observation in Fig. 5.7 that the prepeak grows systematically with x, the extracted $N(x)$ is a monotonously increasing function of x in the whole x range. The dashed line in Fig. 5.14 represents the "ideal hole doping" $N(x) = 1 + x$. One can see a deviation from this "ideal" behavior below $x = 0.30$ with a jump between $x = 0.30$ and 0.40, i. e., below and above $x = x_c$. The present result suggests that below $x = x_c$, doped holes may not be accommodated in the Bi 6*s*-O 2*p* antibonding band in the same way as in the metallic phase, resulting in the reduced $N(x)$ and the insulating behavior. In other words, spectral weight due to the empty Bi 6*s*-O 2*p* states, which should be proportional to $1 + x$, is not concentrated near E_F, but is also distributed away from E_F, presumably overlaid by the Gaussian.

Next, we focus on the shift of the threshold of the XAS spectra. Figure 5.15 (a) shows the XAS spectra of BKBO near the absorption threshold. We define the threshold by the midpoint of the leading edge as marked by the vertical bars in the figure. The result of the threshold shift is shown in the bottom panel of Fig. 5.16. The positions of the prepeak a around $h\nu \sim 529$ eV are also indicated by vertical bars in Fig. 5.15 (a). In going from $x = 0.00$ to 0.20, the prepeak position rapidly moves toward lower photon energies as shown in Fig. 5.8. On the other hand, the threshold is shifted more slowly than that of the prepeak in going from $x = 0.00$ to $x = 0.20$, meaning that the prepeak becomes broader with decreasing x. This may have an origin common with the depression of the spectral weight $N(x)$ in the insulating phase and may be attributed to the structural distortion and the CDW gap formation in the insulating phase. It has been reported in the optical study that the CDW gap of ~ 2 eV opens at $x = 0.00$, while it almost collapses already at $x = 0.24$ [5.13]. On the other hand, in the metallic region at $x \geq 0.40$, the shift of the XAS threshold seems almost saturated. This saturation may arise from the difficulty in the definition of the threshold in the metallic region because of the pile-up of spectral weight near E_F, since the O 1*s* XPS peak shift behaves systematically for $x \leq 0.50$ as reported below.

The depression of $N(x)$ in the insulating phase implies a possible failure

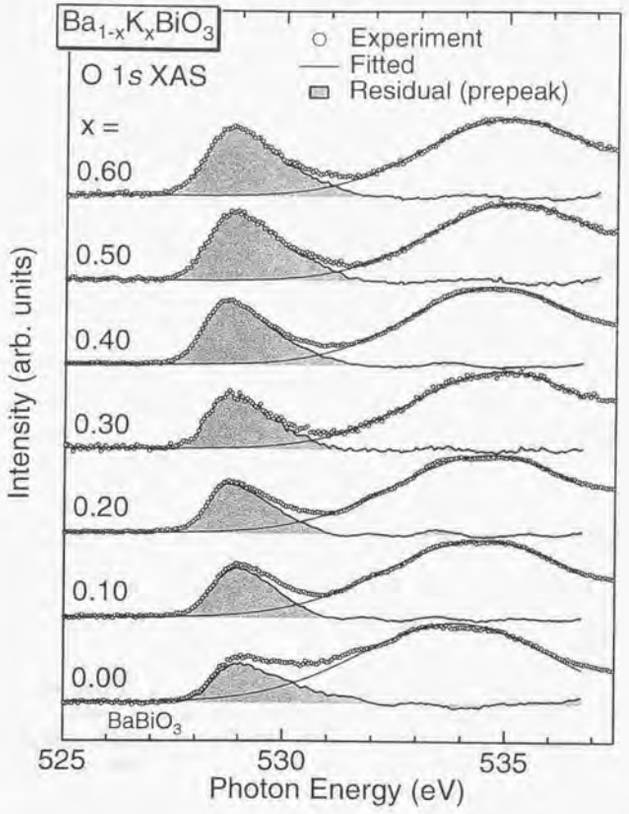

Figure 5.13: Prepeak of the XAS spectra extracted on the assumption that the peak at $h\nu$ = 534–535 eV is a Gaussian.

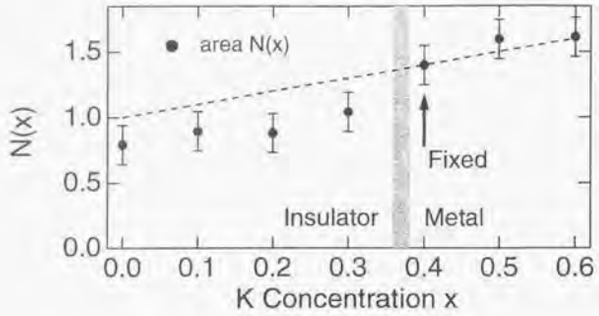

Figure 5.14: Area $N(x)$ of the prepeak relative to that of the main peak. $N(x)$ has been normalized assuming that $N(x = 0.40) = 1.40$. The dashed line represents the "ideal hole doping" as explained in the text.

of the simple rigid-band model. In this region, doped holes would be localized due to strong electron-phonon coupling, which decreases the spectral weight near E_F. This is consistent with the report by Puchkov *et al.* [5.30] that spectral weight observed in the mid-infrared absorption of the insulating BKBO is suppressed and that the lost spectral weight is transferred to a higher energy region. In contrast, above $x = x_c$, spectral weight of the holes introduced by the substitution of K for Ba is distributed near E_F, leading to the regular behavior of $N(x)$.

5.3.4 Core-Level XPS Spectra and Chemical Potential Shift

In Figs. 5.15 (b), (c), and (d), we also show the results of the Bi $4f_{7/2}$, O $1s$, and Ba $3d$ core-level XPS spectra, respectively. According to the high resolution XPS study [5.23], the lineshapes of the core levels of the metallic BKBO are not single peaks but of multi-components with an energy-loss structure on the high binding energy (E_B) side. In fact, the core-level spectra in the metallic phase (particularly, $x = 0.50$ and 0.60) show somewhat broader peak widths than those in the insulating phase. In order not to be disturbed by such energy-loss structures, we use the midpoint of the lower binding energy edge of each peak. The core-level positions thus obtained are shown by vertical bars in Figs. 5.15 (b), (c), and (d). The results of the Bi $4f_{7/2}$, O $1s$, and Ba $3d$ core-level binding energies relative to $x = 0.00$

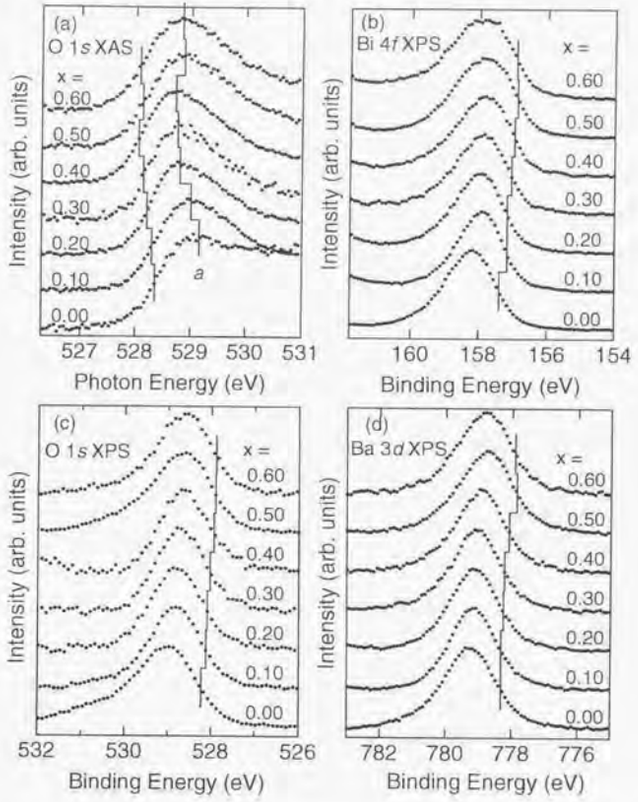

Figure 5.15: (a) O $1s$ XAS spectra of BKBO near the absorption threshold. The threshold defined as the midpoint of the peak are marked with vertical bars. The position of the prepeak a is also shown. (b), (c), and (d) are the XPS spectra of the Bi $4f$, O $1s$ and Ba $3d$ core levels. The midpoint of the peak is marked with the vertical bars. In each panel, the spectra have been normalized to the peak height.

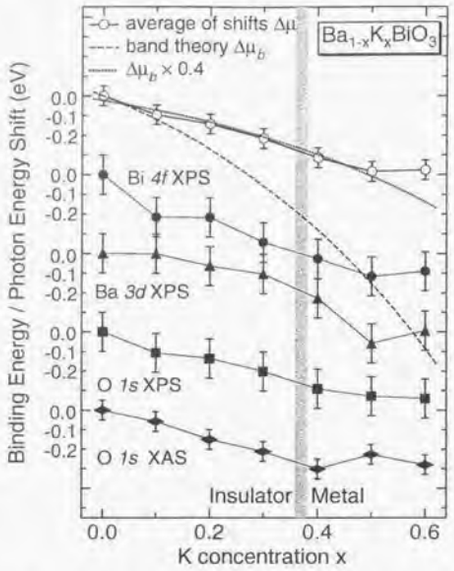

Figure 5.16: Shifts of the O 1*s* XAS threshold and the O 1*s*, Ba 3*d*, and Bi $4f_{7/2}$ XPS core levels. In the top, the average shift of the XAS threshold and the XPS core levels and the theoretical chemical potential shift calculated by band theory [5.5] assuming the rigid-band model are shown.

are compiled in Fig. 5.16. In going from $x = 0.00$ to 0.50 [2], each core level gradually moves to lower E_B by $\sim$ 0.3–0.5 eV. The direction and amount of the core-level shifts are common to all the core levels in agreement with the previous result [5.19]. Between $x = 0.00$ and 0.40, the shift of the O 1*s* core-level XPS spectrum and the shift of the threshold of the O 1*s* XAS spectrum agree with each other quite well, indicating that the XAS threshold corresponds to a transition from the O 1*s* core level to states at E_F.

Here, it is important to note that the core levels of both anion (O) and cations (Ba, Bi) move in the same direction, indicating that the observed shift is a measure of the chemical potential shift caused by the hole doping. We have obtained the average of the shifts of the O 1*s* XAS threshold and the XPS core levels of Ba 3*d*, O 1*s*, and Bi 4*f* as plotted by open circles in Fig. 5.16 and regard it as the experimentally deduced chemical potential shift

[2] The singular behavior at $x = 0.60$ might be due to the fact that the sample is near the solubility limit of K in the BKBO system.

$\Delta\mu(x)$. Except for $x = 0.60$, $\Delta\mu(x)$ decreases monotonously. In Fig. 5.16, we have also plotted the chemical potential shift $\Delta\mu_b(x)$ predicted by the band-structure calculations based on the rigid-band model [5.5] by a dashed curve. The qualitative behavior of $\Delta\mu(x)$ implies that the doping dependence of the BKBO system obeys the rigid-band model, as pointed out before by Namatame *et al.* [5.19]. Quantitatively, however, the amount of $\Delta\mu(x)$ is reduced compared to $\Delta\mu_b(x)$, indicating that the rigid-band model based on the band-structure calculations does not succeed in the quantitative explanation of $\Delta\mu(x)$. In fact, we found that $0.4 \times \Delta\mu_b(x)$ well reproduces the $\Delta\mu(x)$ as shown by a dotted line in the figure. Zakharov *et al.* [5.20] observed a 0.35 eV shift of the O 2*p* band between $x = 0.1$ and 0.4 by photoemission spectroscopy, corresponding to the factor of $\sim$ 0.6. Namatame *et al.* [5.19] also reported that the measured chemical potential shift is reduced almost to half of the theoretical prediction. Theoretical analysis on this factor will be discussed below.

5.3.5 Analysis Based on Fermi-Liquid Theory

In this section, we interpret the observed chemical potential shift $\Delta\mu(x)$ in the metallic phase ($x \geq x_c$) in terms of a simple Landau Fermi-liquid theory, where a rigid-band description is supposed to be valid [5.31]. When the distribution function $n(k\sigma)$ of quasiparticles (QP's) with wave vector k and spin σ is changed by an infinitesimal quantity $\delta n(k\sigma)$, the total energy E of the system changes by

$$\delta E = \sum_{k\sigma} \epsilon^0_{k\sigma} \delta n(k\sigma) + \frac{1}{2} \sum_{k\sigma} \sum_{k'\sigma'} f(k\sigma, k'\sigma') \delta n(k\sigma) \delta n(k'\sigma'), \tag{5.1}$$

where $\epsilon^0_{k\sigma}$ is the energy of a non-interacting QP and $f(k\sigma, k'\sigma)$, which is called a Landau parameter, is the second functional derivative of E. $f(k\sigma, k'\sigma)$ can be divided into the spin-symmetric part $f^S(k, k')$ and the spin-asymmetric one $f^A(k, k')$:

$$f^S(k, k') = \frac{1}{2}(f(k\sigma, k'\sigma) + f(k\sigma, k' - \sigma)) \tag{5.2}$$

$$f^A(k, k') = \frac{1}{2}(f(k\sigma, k'\sigma) - f(k\sigma, k' - \sigma)). \tag{5.3}$$

$f^{S,A}(k, k')$ can be expanded by using Legendre functions $P_l(\cos\theta)$ in the form

$$f^{S,A}(k, k') = \sum_l f^{S,A}_l P_l(\cos\theta). \tag{5.4}$$

Further, $f^{S,A}_l$ is reduced to a dimensionless parameter $F^{S,A}_l$ by multiplying $Vk_F m^*/\pi^2\hbar^2$, where V is the system volume, k_F is the Fermi wave number,

and m^* is the effective mass of the QP. We shall refer to $F_l^{S,A}$ as the Landau parameter hereafter.

We utilize the following equation which holds for an isotropic Fermi liquid [5.32],

$$\frac{\partial\mu}{\partial n} = \frac{1+F_0^S}{N^*(\mu)} \equiv \left(\frac{m_b}{m^*}\right)\frac{1+F_0^S}{N_b(\mu)}, \tag{5.5}$$

where $N^*(\mu)$ is the density of renormalized QP's at the chemical potential μ, m_b and $N_b(\mu)$ are the bare (unrenormalized) band mass and the band density of states (DOS) at μ, respectively, and F_0^S is the Landau parameter introduced above, which represents the isotropic ($l = 0$) spin-symmetric part of the QP-QP repulsion. Since the electronic specific heat coefficient is expressed as

$$\gamma = \frac{\pi^2}{3}k_B^2 N^*(\mu), \tag{5.6}$$

$\Delta\mu$ can be predicted from measured γ if F_0^S is known [5.33]. Many groups [5.34] have reported $\gamma \simeq 1.5$–3.4 mJ/mol K^2, which leads to 0.65–1.4 states/eV-Bi for $N^*(\mu)$. According to a recent report [5.35], γ was estimated to be 2.16, 1.8, and 1.95 for $x = 0.34, 0.37$, and 0.41 which yield $N^*(\mu) = 0.92$, 0.80, and 0.88 state/eV-Bi, respectively. On the other hand, our result of the chemical potential shift around $x \sim 0.4$ indicates that $\partial\mu/\partial n \sim 1.0$ (see Fig. 5.16), which yields $F_0^S = -0.12 < 0$ if we use $N^*(\mu) = 0.88$ for Eq. (5.5). Alternatively, if we use $N^*(\mu)$ slightly larger than ~ 1 according as reported by some groups, we obtain a small, positive value for F_0^S. Hence, we may consider two different scenarios below, namely, $0 \leq F_0^S \ll 1$ and $F_0^S < 0$.

If $0 < F_0^S \ll 1$, the QP-QP repulsion is very weak, which is in a clear contrast to the result of LSCO in the overdoped regime ($x > 0.2$) with $F_0^S \sim 8$ [5.33]. It may be reasonable that BKBO in the metallic region is well described as a Fermi liquid with weak electron-electron correlation since the hybridized Bi 6s-O 2p band has a large band width. Recently, Bansil and Kaprzyk [5.36] treated BKBO using the first-principles Korringa-Kohn-Rostoker coherent-potential-approximation (KKR-CPA) approach and concluded that the total density of state at E_F is reasonably well described by the $BaBiO_3$-based rigid-band model in the whole x range. If this is the case, the aforementioned adjustable parameter 0.4 in $\Delta\mu = 0.4 \times \Delta\mu_b(x)$ yields $m^*/m_b \sim 2$, meaning that the electron-phonon coupling constant $\lambda \sim 1$ since electron-electron correlation is weak and the mass enhancement will be dominated by electron-phonon interaction. $\lambda \sim 1$ is plausible theoretically [5.10], while various experiments have given different λ ranging from 0.1 to 2.1 as compiled in Ref. [5.35].

If F_0^S is negative, it means that the interaction between QP's is attractive. It should be noted here that the Fermi liquid still remains stable for a negative F_0^S if $F_0^S > -1$ [5.31]. The possibility of an attractive interaction between QP's is plausible in that it favors a superconducting pairing or a charge disproportionation. Indeed, a negative F_0^S has been deduced for LSCO in the underdoped superconducting region [5.33]. In fact, it has been intensively argued that the charge disproportionation into Bi^{3+} and Bi^{5+} may have an important role in the metal-insulator transition and the superconductivity in BKBO. Sofo *et al.* [5.37] treated the BPBO system in a simple model where the local disproportionation on Bi atoms is included in a coherent-potential approximation. According to their result (Fig. 1 in Ref. [5.37]), the chemical potential moves more slowly than the expectation based on the rigid-band model, as a result of the disproportionation at the Bi sites. Experimentally, Hellman and Hartford [5.38] found that the conductivity of metallic BKBO has two different contributions such as a semiconducting part and a metallic part. This was also reproduced in the single crystals [5.11]. Presumably, the disproportionation at the Bi sites which dominates the insulating phase of BKBO still remains even in the metallic phase according to this scenario. Although such disproportionation at the Bi sites has been observed as a static order only in the insulating phase [5.22], it is theoretically predicted that a kind of ordered state remains as a mixture of local CDW domains even in the metallic region [5.39]. Such a spatial fluctuation of charge disproportionation or local CDW leads to the opening of a pseudogap in the metallic phase [5.19], which may develop a "hard" CDW gap in the insulating phase, where the charge disproportionation becomes static.

Finally, it is noted that the charge disproportionation at the Bi sites, whether dynamical or static, might lead to the continuous behavior of $\Delta\mu(x)$ across $x = x_c$, while the observed finite jump in the prepeak intensity $N(x)$ between $x = 0.30$ and 0.40 indicates that there exists a definite boundary between the insulating and metallic phases of BKBO. These contrasting facts are left to be consistently clarified experimentally and theoretically in future.

5.4 Conclusion

We have performed XAS and XPS measurements of BKBO in the whole x range ($0 \leq x \leq 0.60$). The XAS results show that the overall electronic structure of the unoccupied states changes systematically with substitution of K for Ba. That is, the intensity of the prepeak increases monotonously with a finite jump between $x = 0.30$ and 0.40, and the absorption threshold moves toward lower energies, at least in the insulating phase. Good overall agreement with the band-structure calculations has been obtained. Comparison with the XAS result of the BPBO system has revealed very different doping-dependent changes in the electronic structure between BKBO and BPBO. In the latter system, Pb substitution replaces the prepeak in $BaBiO_3$ of Bi 6s-O 2p anti-bonding character by another peak of Pb 6s character at a higher energy. The XPS measurements reveal that the chemical potential shift $\Delta\mu(x)$ derived from the core-level shifts moves in the direction predicted

by the rigid-band model. The amount of the shift, however, is almost half of that predicted by the band-structure calculations. We analyzed the behavior of $\Delta\mu(x)$ in terms of a simple Fermi-liquid theory. The interaction between QP's is found to be either weakly repulsive or attractive. While the former case is consistent with a general recognition that BKBO is a weakly correlated system, we also discussed, for the latter case, the possibility of the local charge disproportionation or local CDW remaining in the metallic region of BKBO.

References

[5.1] L. F. Mattheiss, E. M. Gyorgy, and D. W. Johnson, Jr., Phys. Rev. B **37**, 3745 (1988).

[5.2] R. J. Cava, B. Batlogg, J. J. Krajewski, R. Farrow, L. W. Rupp, Jr., A. E. White, K. Short, W. F. Peck, and T. Kometani, Nature (London) **332**, 814 (1988).

[5.3] Shiyou Pei, J. D. Jorgensen, B. Dabrowski, D. G. Hinks, D. R. Richards, A. W. Mitchell, J. M. Newsam, S. K. Sinha, D. Vaknin, and A. J. Jacobson, Phys. Rev. B **41**, 4126 (1990).

[5.4] L. F. Mattheiss and D. R. Hamann, Phys. Rev. B **28**, 4227 (1983).

[5.5] K. Takegahara and T. Kasuya, J. Phys. Soc. Jpn. **56**, 1478 (1987).

[5.6] L. F. Mattheiss and D. R. Hamann, Phys. Rev. Lett. **60**, 2681 (1988).

[5.7] N. Hamada, S. Massidda, A. J. Freeman, and J. Redinger, Phys. Rev. B **40**, 4442 (1989).

[5.8] D. E. Cox and A. W. Sleight, Solid State Commun. **19**, 969 (1976).

[5.9] K. Takegahara, J. Electron Spectrosc. Relat. Phenom. **66**, 303 (1994).

[5.10] A. I. Liechtenstein, I. I. Mazin, C. O. Rodriguez, O. Jepsen, O. K. Andersen, and M. Methfessel, Phys. Rev. B **44**, 5388 (1991).

[5.11] T. Uchida, Doctor Thesis, (Aoyama-Gakuin University, 1995).

[5.12] S. Tajima, S. Uchida, A. Masaki, H. Takagi, K. Kitazawa, S. Tanaka, and A. Katsui, Phys. Rev. B **32**, 6302 (1985); S. Tajima, S. Uchida, A. Masaki, H. Tagaki, K. Kitazawa, S. Tanaka, and S. Sugai, *ibid.* **35**, 696 (1987); C. Chaillout, A. Santoro, J. P. Remeika, A. S. Cooper, G. P. Espinosa, and M. Marezio, Solid State Commun. **65**, 1363 (1988).

[5.13] M. A. Karlow, S. L. Cooper, A. K. Kots, M. V. Klein, P. D. Han and D. A. Payne, Phys. Rev. B **48**, 6499 (1993).

[5.14] T. M. Rice and L. Sneddon, Phys. Rev. Lett. **47**, 689 (1981).

[5.15] D. Yoshioka and H. Fukuyama, J. Phys. Soc. Jpn. **54**, 2996 (1985).

[5.16] R. M. Noack, D. J. Scalapino, and R. T. Scalettar, Phys. Rev. Lett. **66**, 778 (1991).

[5.17] M. W. Ruckman, D. Di Marzio, Y. Jeon, G. Liang, J. Chen, M. Croft, and M. S. Hegde, Phys. Rev. B **39**, 7359 (1989).

[5.18] M. Nagoshi, T. Suzuki, Y. Fukuda, K. Ueki, A. Tokiwa, M. Kikuchi, Y. Syono, and M. Tachiki, J. Phys.: Condens. Matter **4**, 5769 (1992).

[5.19] H. Namatame, A. Fujimori, H. Torii, T. Uchida, Y. Nagata, and J. Akimitsu, Phys. Rev. B **50**, 13674 (1994).

[5.20] A. A. Zakharov, U. Johansson, M. Leandersson, H. Nylén, M. Qvarford, I. Lindau, and R. Nyholm, Phys. Rev. B **56**, R5755 (1997)

[5.21] T. J. Wagener, H. M. Meyer III, D. M. Hill, Y. -J. Hu, M. B. Jost, J. H. Weaver, D. G. Hinks, B. Dabrowski, and D. R. Richards, Phys. Rev. B **40**, 4532 (1989).

[5.22] S. Salem-Sugui, Jr., E. E. Alp, S. M. Mini, M. Ramanathan, J. C. Campuzano, G. Jennings, M. Faiz, S. Pei, B. Dabrowski, Y. Zheng, D. R. Richards, and D. G. Hinks, Phys. Rev. B **43**, 5511 (1991)

[5.23] M. Qvarford, V. G. Nazin, A. A. Zakharov, M. N. Mikheeva, J. N. Andersen, M. K.-J. Johansson, G. Chiaia, T. Rogelet, S. Söderholm, O. Tjernberg, H. Nylén, I. Lindau, R. Nyholm, U. O. Karlsson, S. N. Barilo, and S. V. Shiryaev, Phys. Rev. B **54**, 6700 (1996).

[5.24] H. Nylén, A. Beutler, A. A. Zakharov, M. Leandersson, M. Qvarford, I. Lindau, M. B. Tsetlin, L. L. Lev, M. N. Mikheeva, S. N. Barilo, and S. V. Shiryaev, Phys. Rev. B **58**, 12836 (1998).

[5.25] C. T. Chen, F. Sette, Y. Ma, M. S. Hybertsen, E. B. Stechel, W. M. C. Foulkes, M. Schluter, S.-W. Cheong, A. S. Cooper, L. W. Rupp, Jr., B. Batlogg, Y. L. Soo, Z. H. Ming, A. Krol, and Y. H. Kao, Phys. Rev. Lett. **66**, 104 (1991).

[5.26] Y. Nagata, N. Suzuki, T. Uchida, W. D. Mosley, P. Klavins, and R. N. Shelton, Physica C **195**, 195 (1992); T. Uchida, S. Nakamura, N. Suzuki, Y. Nagata, W. D. Mosley, M. D. Lan, P. Klavins, and R. N. Shelton, *ibid.* **215**, 350 (1993).

[5.27] M. Grioni, J. B. Goedkoop, R. Schoorl, F. M. F. de Groot, J. C. Fuggle, F. Schäfers, E. E. Koch, G. Rossi, J.-M. Esteva, and R. C. Karnatak, Phys. Rev. B **39**, 1541 (1989).

[5.28] T. Saitoh, T. Mizokawa, A. Fujimori, M. Abbate, Y. Takeda, and M. Takano, Phys. Rev. B **56**, 1290 (1997).

[5.29] F. M. F. de Groot, J. C. Fuggle, and J. M. van Ruitenbeek, Phys. Rev. B **44**, 5280 (1991).

[5.30] A. V. Puchkov, T. Timusk, M. A. Karlow, S. L. Cooper, P. D. Han, and D. A. Payne, Phys. Rev. B **54**, 6686 (1996).

[5.31] P. Nozières, *Theory of Interacting Fermi Systems* (Benjamin, 1964).

[5.32] N. Furukawa and M. Imada, J. Phys. Soc. Jpn. **61**, 3331 (1992).

[5.33] A. Ino, T. Mizokawa, A. Fujimori, K. Tamasaku, H. Eisaki, S. Uchida, T. Kimura, T. Sasagawa, and K. Kishio, Phys. Rev. Lett. **79**, 2101 (1997).

[5.34] For example, B. Batlogg, R. J. Cava, L. W. Rupp, Jr., A. M. Mujsce, J. J. Krajewski, J. P. Remeika, W. F. Peck, A. S. Cooper, and G. P. Espinosa, Phys. Rev. Lett. **61**, 1670 (1988); Z. I. Huang, H. H. Fang, Y. Y. Hue, P. H. Hor, C. W. Chu, M. L. Norton, and H. Y. Tang, Physica C **180**, 331 (1991); J. E. Graebner, L. F. Schneemeyer, and J. K. Thomas, Phys. Rev. B **39**, 9682 (1989); references in Ref. [5.35].

[5.35] S. N. Barilo, S. V. Shiryaev, V. I. Gatalskaya, J. W. Lynn, M. Baran, H. Szymczak, R. Szymczak, and D. Dew-Hughes, Phys. Rev. B **58**, 12355 (1998).

[5.36] A. Bansil and S. Kaprzyk, Phys. Rev. B **43**, 10335 (1991).

[5.37] J. O. Sofo, A. A. Aligia, and M. D. N. Requeiro, Phys. Rev. B **40**, 6955 (1989).

[5.38] E. S. Hellman and E. H. Hartford, Jr., Phys. Rev. B **47**, 11346 (1993)

[5.39] K. Iwano and K. Nasu, Phys. Rev. B **57**, 6957 (1998).

Chapter 6

Summary

We have performed photoemission spectroscopy (PES) studies on three different kinds of oxide system, NaV_2O_5, Ti_4O_7, and $Ba_{1-x}K_xBiO_3$ (BKBO) where both electron-electron and electron-lattice interactions are thought to play a significant role. Our main findings are summarized for each system as follows.

NaV_2O_5 The angle-resolved photoemission (ARPES) study of NaV_2O_5 has made it clear that the electronic structure of the valence band is highly anisotropic. The ARPES study by changing the temperature has revealed that the lower Hubbard band shows massive redistribution of spectral weight over the energy-momentum space. The overall agreement between the one-dimensional (1D) t-J model and our observations implies that the spin-charge separation picture is valid in the excitation spectra of this system. Although they are more drastic than the theoretical prediction, the experimental finite temperature effects have been partly explained by the theory, which may be expressed as the Fermi surface effect of the spinon band.

Ti_4O_7 The Ti $3d$ band shows characteristic temperature-dependent PES spectra corresponding to the three phases of Ti_4O_7. The spectra of the metallic phase at $T > 154$ K show weak coherent part with stronger incoherent part, signaling that the d electrons in this compound are strongly correlated. In the spectra of the low-temperature insulating phase at $T \lesssim 140$ K, a finite gap is observed reflecting the charge ordering in this phase. The spectra of the high-temperature insulating (HI) phase at $140 < T \lesssim 154$ K are gapless at the Fermi level (E_F) and the spectral intensity around E_F can be well expressed as $(E - E_F)^2$. This fact implies the existence of a soft Coulomb gap due to dynamical disorder under the influence of long-range Coulomb interaction. Quantitative discussion on the PES spectra of Fe_3O_4 has lead to a physical description consistent with the case of Ti_4O_7.

$Ba_{1-x}K_xBiO_3$ The x-ray absorption spectroscopy (XAS) study on BKBO has revealed that the overall electronic structure of the unoccupied states changes systematically with substitution of K for Ba. In contrast to the case of $La_{2-x}Sr_xCuO_4$, the intensity of the prepeak increases monotonously with x with a finite jump between $x = 0.30$ and 0.40, and the absorption threshold moves toward lower energies, at least in the insulating phase. Good overall agreement with the band-structure calculations has been obtained. The XPS measurements reveal that the chemical potential shift derived from the core-level shifts moves in the direction predicted by the rigid-band model. The amount of the shift, however, is almost half of that predicted by the band-structure calculations. According to the analysis of the shift based on a simple Fermi-liquid theory, the interaction between quasi-particles is found to be either weakly repulsive or attractive.

As introduced in Chapter 1, the electron correlation and the electron-lattice interaction are roughly characterized by the on-site Coulomb repulsion U and the lattice deformation energy $S \sim g^2/C$, where g is the electron-phonon coupling parameter and C is the elastic constant. In the present work, we have found that the PES spectra of those systems show considerable spectral-weight transfer with temperature or hole-concentration. The origin of these phenomena has been attributed to electron-electron and/or electron-lattice interactions, while the degree of their contributions differs from compound to compound. In fact, BKBO has been found to have only weak electron correlation through the core-level shift measurements and large electron-lattice coupling is, therefore, suggested in order to explain the spectral-weight transfer at the semiconductor-to-metal transition observed in the XAS spectra. In this sense, the electron-lattice interaction seems to be dominant in BKBO, that is "$U < S$". In contrast, strong electron correlation in one dimension explains most of the finite-temperature effects observed in NaV_2O_5 within the 1D t-J model, while there still remains some room to be explained in order to obtain more quantitative agreement between theory and experiment, presumably indicating the necessity of including electron-lattice interaction. We may conclude that NaV_2O_5 in this temperature range is expressed as "$U > S$". If PES measurements could be performed for the charge ordered state in the low temperature, the information on the state under the competition would be obtained, which is left for future study. In Ti_4O_7, we have found a clear indication of both the long-range Coulomb interaction and the disorder due to formation of mobile bipolarons. In the metallic state, Ti_4O_7 has large electron correlation with the substantial effect of the electron-lattice interaction. In the low-temperature insulating phase, "$U \sim S$" holds resulting in the ordered state of bipolarons. In the intermediate disordered phase, significant influence of long-range Coulomb interaction yields a soft Coulomb gap. Although the resultant soft gap may be most

striking, we would like to emphasize that the competition between the two interactions in this phase brings such an exotic state like "bipolaron liquid" into existence. A similar description is well applicable to Fe_3O_4, supporting our interpretation of Ti_4O_7. By comparing different roles of U and S in the three kinds of compounds, we may conclude that the difference in the importance of the two interactions yields a variety of observed ground states of the spin-Peierls phase in NaV_2O_5, the Verwey state in Ti_4O_7, and the superconductivity or charge-density-wave state in BKBO. The difference of dimensionality may be also significant: three dimension for BKBO, one dimension for NaV_2O_5, and strong anisotropy in Ti_4O_7.

Finally, our results give a typical example as to how the competition between electron-electron and electron-lattice interactions affects the physical properties. While theoretical treatments of PES spectra described by parameters of order eV such as the on-site Coulomb energy have been well established, quantitative treatment relevant to low-energy excitations is far from comprehensive understanding and still in progress. Such problems are certainly one of the most important problems in solid state physics left to be solved in future.

Appendix A

Alternative Analysis of the APRES Spectra of NaV_2O_5

In Chapter 3, we report the ARPES spectra of $Na_{0.96}V_2O_5$ at 120 K and 300 K and discussed the physical meaning of the results in detail. Actually, in our process of study on the $Na_xV_2O_5$ ($x = 0.96$ and 1) system, we first performed ARPES measurements of stoichiometric NaV_2O_5 at 300 K, for which we could not measure at low temperatures due to severe charging effect. Subsequently, the measurements of Na-deficient $Na_{0.96}V_2O_5$ were successfully performed until down to 120 K. As pointed out in Chapter 3, the results of NaV_2O_5 are consistent with the results of $Na_{0.96}V_2O_5$. Here, we append our original analysis on the ARPES spectra of NaV_2O_5.

In Fig. A.1, we show the He I spectra of the V $3d$ band normalized to the peak height at the binding energy (E_B) $\sim$ 1.5 eV rather than to the area. For the momentum (k) $\parallel b$ spectra shown in Fig. A.1 (a), the take-off angle θ was varied from $-19°$ to $53°$, corresponding to $k = -0.7\pi$ to 1.8π along the b-axis. The lineshape of the lower binding energy side of the peak (E_B = 0.5–1.2 eV) shows a weak but clear k-dependence. The inflection points obtained from the second derivative of the spectra are marked with vertical bars in the same figure while this dispersion seems to overlap the stronger feature centered at E_B = 1.5 eV. The intensity plot in the E-k plane on the grey scale shown in Fig. A.1 (b) indicates that the lower binding energy side of the lower Hubbard band disperses with the periodicity of π, half of the reciprocal lattice vector $k = 2\pi$. In fact, the spectra at $k = -\pi/2$, $\pi/2$ and $3/2\pi$ have shoulders around E_B = 0.5–1.2 eV. It thus appears that the spatial periodicity is effectively doubled for the electronic structure of the V $3d$ states. On the contrary, the higher binding energy side (E_B = 1.8–2.5 eV) shows no signals of periodicity π and the result seems consistent with

The content of this appendix was reported in: K. Kobayashi, T. Mizokawa, A. Fujimori, M. Isobe, and Y. Ueda: Single-Particle Excitations in One-Dimensional Mott-Hubbard Insulator NaV_2O_5, Phys. Rev. Lett. **80**, 3121 (1998).

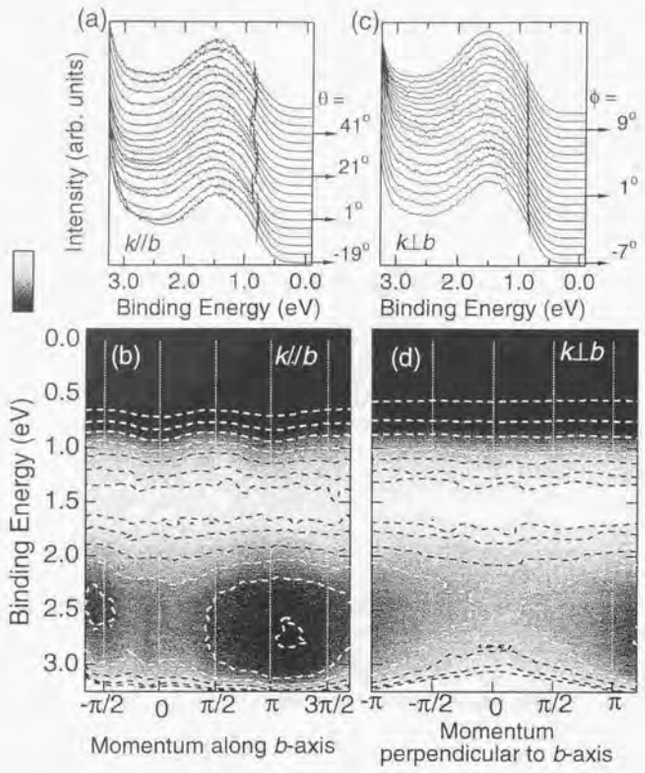

Figure A.1: (a) $k \parallel b$ spectra in the V $3d$ band region. They are normalized to the peak height around $E_B = 1.5$ eV. The vertical lines indicate the inflection points. (b) The intensity plot. The dashed lines are contours. (c) $k \perp b$ spectra in the V $3d$ band region and (d) the intensity plot.

the periodicity of 2π as in the O $2p$ band, reflecting the periodicity of the crystal structure (although we could not check the 2π periodicity within our k-range $\sim 2\pi$). The structure centered at $E_B \sim 1.5$ eV itself does not seem to disperse. We show the $k \perp b$ spectra in Fig. A.1 (c) with their inflection points marked by vertical lines, which signals no dispersive feature. The intensity plot in Fig. A.1 (d) also does not show any detectable k-dependent modulation on the lower binding energy side of the lower Hubbard band.

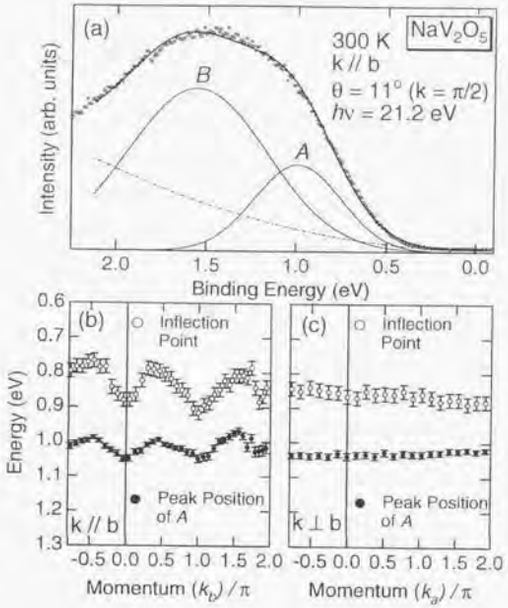

Figure A.2: (a) Line-shape analysis of an ARPES spectrum. The measured spectrum is plotted with dots. I, I_A and I_B with solid curves, and I_{bg} with a dot-dashed curve. (b) Peak positions for the $k \parallel b$ spectra obtained from the lineshape analysis (closed circles and the inflection points) and the inflection points (open circles). (c) Peak positions for the $k \perp b$ spectra.

To perform more quantitative analysis, we have made a line-shape analysis between $E_B = -0.1$ and 2.1 eV on the assumption that each spectrum I can be decomposed into two components and an appropriate background as $I = I_A + I_B + I_{bg}$ as shown in Fig. A.2 (a). Here, I_A and I_B are assumed to be Gaussian and represents the dispersive feature on the lower binding energy side of the ~ 1.5 eV peak and that of the non-dispersive feature at ~ 1.5 eV, respectively, although actual lineshapes may be more complicated [A.1–4]. I_{bg} is assumed to be $\propto E_B^2$. The peak position and the width of Gaussian A were treated as fitting parameters while those of B were assumed to be k-independent[1] In Fig. A.2 (b), we have plotted the peak position of A as

[1]The position of peak B may be weakly dependent on k_b but when it was allowed to vary with k_b, we could not obtain reasonable convergence in the least-squares fitting.

well as the inflection points. The figure shows that the momentum dependence of the peak position of A, which is consistent with that of the inflection point, seems to have the periodicity of π, fully supporting our observation discussed above. In Fig. A.2 (*c*), we show the result of the analysis of the $k \perp b$ spectra, indicating no detectable k-dependence.

Since the theoretical interpretations for these observations have been discussed already in Sec. 3, it is not repeated here. Finally, the following two points are mentioned based on the results of the ARPES spectra of this system at 120 K and 300 K.

- The spectra of the more insulating NaV_2O_5 than $Na_{0.96}V_2O_5$ were slightly distorted toward higher E_B due to weak charging effect even at 300 K.
- Peak B includes the spinon and holon bands located at higher binding energies, in which we were not confident when we first analyzed NaV_2O_5 data, partly because drastic finite-temperature effects broaden the ARPES spectra at 300 K and partly because the slight charging effect smears the spectra of NaV_2O_5.

References

[A.1] S. Sorella and A. Parola, J. Phys. Cond. Matter **4**, 3589 (1992).

[A.2] T. Tohyama and S. Maekawa, unpublished.

[A.3] D. Augier, D. Poilblanc, S. Haas, A. Delia, and E. Dagotto, Phys. Rev. B **56**, 5732 (1997).

[A.4] J. Favand, S. Haas, K.Penc, F. Mila, and E. Dagotto Phys. Rev. B **55**, 4859 (1997).

Acknowledgments

I greatly owe the present thesis to many people.

First of all, I would like to thank Prof. Atsushi Fujimori for having suggested this work and always giving me instruction full of encouragement for more than six years. I also acknowledge Prof. Takashi Mizokawa who has been advising me both on experiment and theory since I was a master course student.

Single-crystal NaV_2O_5 samples were kindly provided by Prof. Yutaka Ueda and Dr. Masahiko Isobe. Prof. Takami Tohyama and Prof. Sadamichi Maekawa graciously offered us their results of the exact diagonalization studies prior to publication and taught me the theoretical details on the correlated one-dimensional systems. I could also learn much through discussion with Dr. Hidekatsu Suzuura. I would also like to thank Prof. Norio Kawakami and Dr. Tetsuya Mutou for informative discussions. I also appreciate many enlightening discussions with Prof. Hiroyuki Shiba, Dr. Karlo Penc, Dr. Changyoung Kim, and Prof. Dick van der Marel.

Single-crystal Ti_4O_7 samples were graciously provided by Prof. Hidenori Takagi and Dr. Toru Tonogai. Their advises were of great help in the experiments. Mr. Katsuhiro Tobe supported the initial experiments on Ti_4O_7. Dr. Miguel Abbate kindly sent me their XAS data of Ti_4O_7. A productive discussion with Dr. Daniel Khomskii has greatly promoted my understanding on Ti_4O_7 and Fe_3O_4.

Single-crystal BKBO samples were kindly provided by Prof. Yujiro Nagata, Dr. Hiroaki Samata, and Mr. Amane Mishiro. Prof. Yujiro Nagata warmly answered my requests and inquiries on samples. I would like to thank Dr. Frank M. F. de Groot for discussion and collaboration with us. We would like to thank Prof. Hidenori Takagi for providing us with the $BaBiO_3$ sample. We would like to thank Dr. Takuya Hashimoto for informative discussions. The experiment at Photon Factory, which was technically supported by the staff of Photon Factory, was performed under the approval of the Photon Factory Program Advisory Committee (Proposal No. 94-G361).

I would like to thank Dr. Motohiko Nakamura and Dr. Ashish Chainani for their detailed advice on the ARPES measurements, and Dr. Yoshihiro Aiura for teaching me his expertise on a general UPS system including on a He refrigerator. Mr. Shigemi Otsuka often advised and helped me with many

technical problems.

I enjoyed the time which I spent for the band-structure calculations of NaV_2O_5 under the guidance of Dr. Leonard F. Mattheiss who graciously and patiently taught me the method of the calculations. Though I could not complete the trial to NaV_2O_5 because of the peculiarity of NaV_2O_5, I am convinced that this experience will serve someday.

Our work was supported by a Grant-in-Aid for Scientific Research from the Ministry of Education, Science and Culture and by a Special Coordination Fund from the Science and Technology Agency of Japan. I was financially supported by a Research Fellowship of the Japan Society for the Promotion of Science for Young Scientists.

It is of great pleasure to express my most sincere thanks to Mr. Jin-Young Son and Dr. Akihiro Ino for their encouragement and help through more than five years that I spent in Fujimori laboratory. Mr. Tomofumi Susaki has readily cooperated with me on the new UPS system. I also greatly owe the following people: Prof. Dipanker D. Sarma, Prof. Hirofumi Namatame, Dr. Antoine E. Bocquet, Dr. Oliver Radar, Dr. Keiji Morikawa, Dr. Kenya Shimada, Dr. Tomohiko Saitoh, Dr. Kazutoshi Mamiya, Dr. Akira Sekiyama, Dr. Takehisa Konishi, Mr. Jun Okamoto, Mr. Toshiyuki Tsujioka, Mr. Jobu Matsuno, Mr. Jun Okabayashi, Mr. Masahiko Satake, Mr. Teppei Yoshida, Mr. Kouzou Okazaki, Mr. Yoshisuke Ishikawa, Mr. Hiroyuki Ishii, Mr. Takashi Nambu, Mr. Naoyuki Harima, Ms. Hazuki Wakazono and Mrs. Naoko Misawa.

Last but not least, I thank my parents, my brother, my sister, and my wife for their support and their love.

Tokyo
June 1999

Kensuke Kobayashi